

UNIVERSITY OF WARSAW

DOCTORAL THESIS

**Observations of anomalous transverse
local momenta in spatial wave-functions**

Author:

Bohnishikha GHOSH

Supervisor:

Dr. Radosław ŁAPKIEWICZ
Dr. hab. Piotr WASYLCHYK

*A thesis submitted in fulfillment of the requirements
for the degree of Doctor of Philosophy*

in the

Quantum Imaging Laboratory
Division of Optics, Institute of Experimental Physics
Faculty of Physics, University of Warsaw

February 6, 2025

Declaration of Authorship

I, Bohnishikha GHOSH, declare that this thesis titled, "Observations of anomalous transverse local momenta in spatial wave-functions" and the work presented in it are my own. I confirm that:

- This work was done wholly or mainly while in candidature for a research degree at this University.
- Where any part of this thesis has previously been submitted for a degree or any other qualification at this University or any other institution, this has been clearly stated.
- Where I have consulted the published work of others, this is always clearly attributed.
- Where I have quoted from the work of others, the source is always given. With the exception of such quotations, this thesis is entirely my own work.
- I have acknowledged all main sources of help.
- Where the thesis is based on work done by myself jointly with others, I have made clear exactly what was done by others and what I have contributed myself.

Signed:

Date:

“God runs electromagnetics by wave theory on Monday, Wednesday, and Friday, and the Devil runs them by quantum theory on Tuesday, Thursday, and Saturday.”

Sir William Bragg

UNIVERSITY OF WARSAW

Abstract

Faculty of Physics

Doctoral Dissertation

Observations of anomalous transverse local momenta in spatial wave-functions

by Bohnishikha GHOSH

The wavefunction of a quantum particle leads to distinctly non-classical mechanical effects. An important example is quantum tunneling, which enables scanning tunneling microscopy, Josephson junctions, and flash memory. An equally puzzling effect is quantum backflow — an interference effect where a free quantum particle with positive momentum exhibits negative probability current at some space-time point, seemingly moving backwards. This is explained by the distinction between local properties such as probability density and probability current and global properties such as momentum, which require knowledge of the entire wavefunction.

The term ‘quantum’ in quantum backflow underscores the stark contrast between classical and quantum particle dynamics. The broader concept of ‘backflow’—a wave phenomenon where the flow of some quantity (such as energy or probability) in certain regions of space-time is opposite to the flow direction of its constituent elementary waves—is explored experimentally and theoretically with classical and quantum light in this thesis. Our experimental observations of anomalous transverse ‘local’ linear and orbital angular momentum in simple optical two-beam interference using a Shack-Hartmann wavefront sensor, provide new insights and highlight that ‘backflow’ in such scenarios is quite common, owing to the practical impossibility of creating the constituent beams with perfectly equal amplitudes. These observations are extended to the single photon regime.

It ought to be noted that the flow of energy, quantified by the Poynting momentum, is co-directional with the measured local momentum only in the case of linearly polarized paraxial fields in free space. As discussed in a dedicated chapter of the thesis, this assumption no longer holds true for vector fields.

Despite the observations of backflow in optical systems, the prospect of experimentally observing the counter-propagation of a massive quantum particle, such as an electron, remains a compelling challenge. A proposal, to observe the phenomenon with electrons in a transmission electron microscope, is discussed in this thesis.

UNIwersytet Warszawski

Streszczenie

Wydział Fizyki

Rozprawa Doktorska

Obserwacje anomalnych poprzecznych lokalnych pędów w przestrzennych funkcjach falowych

Bohnishikha GHOSH

Funkcja falowa cząstki kwantowej prowadzi do wyraźnie nieklasycznych efektów mechanicznych. Ważnym przykładem jest tunelowanie kwantowe, które umożliwia skaningową mikroskopię tunelową, łączy Josephsona oraz pamięci flash. Równie zagadkowym zjawiskiem jest kwantowy przepływ wsteczny — efekt interferencyjny, w którym swobodna cząstka kwantowa o dodatnim pędzie wykazuje ujemny prąd prawdopodobieństwa w pewnym punkcie czasoprzestrzeni, pozornie poruszając się wstecz. Zjawisko to można wyjaśnić różnicą między lokalnymi właściwościami, takimi jak gęstość prawdopodobieństwa i prąd prawdopodobieństwa, a globalnymi właściwościami, takimi jak pęd, które wymagają znajomości całej funkcji falowej.

Termin „kwantowy” w przepływie wstecznym podkreśla wyraźny kontrast między klasyczną a kwantową dynamiką cząstek. Szersza koncepcja „przepływu wstecznego” — zjawiska falowego, w którym przepływ pewnej wielkości (takiej jak energia lub prawdopodobieństwo) w określonych obszarach czasoprzestrzeni jest przeciwny do kierunku przepływu jego składowych fal elementarnych — jest badana doświadczalnie i teoretycznie w świetle klasycznym i kwantowym w tej rozprawie. Nasze obserwacje anomalnego poprzecznego „lokalnego” pędu liniowego i orbitalnego momentu pędu w prostych superpozycjach dwóch wiązek światła przy użyciu sensora frontu falowego Shacka-Hartmanna demonstrują, że „przepływ wsteczny” w takich scenariuszach jest dość powszechny, z uwagi na praktyczną niemożność stworzenia wiązek składowych o idealnie równych amplitudach. Obserwacje te zostały rozszerzone do reżimu pojedynczych fotonów.

Należy zauważyć, że przepływ energii, kwantyfikowany poprzez wektor Poyntinga, jest współkierunkowy z mierzonym lokalnym pędem jedynie w przypadku liniowo spolaryzowanych przyosiowych pól w wolnej przestrzeni. Jak omówiono w dedykowanym rozdziale rozprawy, założenie to przestaje być prawdziwe dla pól wektorowych.

Pomimo obserwacji przepływu wstecznego w układach optycznych, perspektywa eksperymentalnego zaobserwowania tego zjawiska dla masywnej cząstki kwantowej, takiej jak elektron, pozostaje interesującym wyzwaniem. W pracy omówiono propozycję zaobserwowania tego zjawiska przy użyciu elektronów w transmisyjnym mikroskopie elektronowym.

Acknowledgements

At the outset, I would like to express my deepest gratitude to my supervisor, Dr. Radek Łapkiewicz. This dissertation would not have taken shape without his unwavering guidance, support, and encouragement. His insightful advice, patience, and belief in my abilities have been instrumental in both my academic and personal growth. Thanks to his mentorship, I have not only expanded my knowledge but have also learned how to navigate academic and administrative challenges with confidence.

I am also sincerely grateful to Prof. Piotr Wasylczyk for his support and guidance throughout this process. Furthermore, I would like to thank Mrs. Halina Przychoźeń and the Division of Optics, Faculty of Physics (FUW), University of Warsaw at large, as well as the Doctoral School of Exact and Natural Sciences, for their invaluable administrative assistance during my doctoral journey, which provided me with a solid foundation to pursue my research.

A heartfelt thanks goes to the past and present members of the Quantum Imaging Lab group at FUW, for creating a special, supportive, and stimulating environment—one filled with academic rigor and a sense of fun. In particular, I express my sincere gratitude to Dr. Anat Daniel and Bernard Gorzkowski, who have been incredible collaborators and teammates. Working with them has been an enriching experience.

Additionally, I express my earnest thanks to Dr. Monika Pawłowska, Adrian Makowski, Paweł Szczypkowski, Alexander Krupiński-Ptaszek, Dr. Sanjukta Kundu, and Jerzy Szuniewicz for several fruitful academic discussions over the years of my studies. A special word of thanks goes to Jakub Lewandowski, whose enthusiasm and insights taught me quite a lot.

I must also thank all the wonderful collaborators I have had the privilege of learning from: Prof. Tomasz Paterek for introducing us to the concept of backflow, Dr. Arseni Goussev for his deep insights and mathematical expertise on the subject, Prof. Konstantin Bliokh for generously sharing his vast and incredible knowledge of structured light with us, and Prof. Thomas Juffmann for his quick, astute observations and for sharing his knowledge of the transmission electron microscope. Additionally, I thank Prof. Iwo Białynicki-Birula, Prof. Robert Fickler, Dr. Filippo Cardano, and Prof. Miguel Navascués for very insightful discussions and exchange of ideas.

Several others outside of the lab and collaborations have also impacted my PhD journey. I would like to express my gratitude to Prof. Nirmalya Ghosh, a mentor since my formative years at the Indian Institute of Science Education and Research, Kolkata (IISER-K), and to my friends from IISER-K who, while enduring and enjoying their own PhD journeys in various parts of the world, have kept in touch and provided constant support. Additionally, I am thankful to a set of great friends I have spent time with in Warsaw—Kaustav, Sudeep, Sanjukta, Deeksha, Chandan, Rubina and Suchetana—whose companionship has made this journey all the more memorable.

Finally, I would like to express my deepest gratitude to my family for their continuous support and inexhaustible patience: to my father, my first mentor, for introducing me to research in quantum physics, and to my mother, for teaching me perseverance. Last but not least, I thank Shubhayan for the discussions on physics at odd hours and for his unwavering love and support.

The research presented in this dissertation was funded by the First TEAM project “Spatiotemporal photon correlation measurements for quantum metrology and superresolution microscopy” co-financed by the European Union under the European Regional Development Fund (POIR.04.04.00-00-3004/17-00) as well as the project titled “Super-resolution imaging in scattering media based on fluorescence intensity correlations”, funded by the National Science Center (NCN) within the OPUS 24 programme.

Contents

Declaration of Authorship	iii
Abstract	vii
Streszczenie	ix
Acknowledgements	xi
1 Introduction	1
1.1 Backflow in quantum mechanics	3
1.1.1 An unusual example of a state exhibiting backflow	4
1.2 Backflow in optics	6
1.2.1 Counter-propagating solutions to the paraxial Helmholtz equation	7
1.2.2 Anomalous values of local transverse momentum	9
Using superoscillations for super-resolution imaging	9
1.3 Concluding remarks	10
2 Transverse local momentum and its measurement	13
2.1 Measuring local momentum using the Shack-Hartmann wavefront sensor	13
2.1.1 Algorithm to measure centroid displacements	15
2.1.2 How ‘local’ is local momentum?	16
2.1.3 The algorithm’s error in estimating a spot’s centroid	17
2.2 The connection between local momentum and Poynting vector	18
2.2.1 The Poynting-canonical dilemma in circularly polarized vortex beams	19
2.3 Concluding remarks	21
3 Backflow in the interference of two Gaussian beams	23
3.1 Introduction to the concept	23
3.2 A polarisation based common path Mach-Zehnder interferometer	25
3.3 Experimental results	26
3.3.1 Explaining the difference in heights of the peaks of $k_{s,x}$	27
3.3.2 Ensuring backflow beyond the tails of the Gaussian spectra of the constituent beams	29
3.3.3 Measuring ‘local momentum’ with microlenses of finite size	31
3.3.4 A slight deviation of the data from the theoretical plot in the bright fringes	31
3.4 Concluding remarks	32

4	Observation of Azimuthal backflow	35
4.1	Introduction	35
4.1.1	Theoretical Model	36
4.1.2	Angular extent of the region of backflow	38
4.1.3	Azimuthal backflow persists upon beam propagation	39
4.1.4	Exploring azimuthal backflow in the superposition of Laguerre-Gauss beams	40
4.2	The Experiment	42
4.2.1	Experimental Results	43
4.2.2	Error Analysis	46
4.3	Concluding remarks	46
5	Optical backflow in the single photon regime	49
5.1	Introduction	49
5.1.1	Simulations with Poisson noise	49
5.2	The experiment	51
5.2.1	A source of single photons generated by SPDC	52
5.2.2	Heralding one photon via the detection of its counterpart using an intensified camera	52
5.2.3	Setup to observe azimuthal backflow with heralded single photons	53
5.2.4	Simulating the experiment with an attenuated laser	54
5.2.5	Difficulties in realising the experiment with heralded single photons and possible solutions	55
5.3	Concluding remarks	57
6	Quantum backflow with electrons: a proposal	63
6.1	Introduction and motivation	63
6.2	A very brief introduction to the TEM and its operation	64
6.3	Backflow with electrons in a TEM	65
6.3.1	Theoretical description under the paraxial approximation	65
6.4	Images of a double slit from a TEM in diffraction mode	70
6.5	Concluding remarks	71
7	Conclusion and outlook	73
7.1	Dissertation summary	73
7.2	Outlook	74
7.2.1	On the distinction between canonical momentum and Poynting momentum	74
7.2.2	On the observations of optical backflow with classical light	74
7.2.3	On the attempt to observe optical backflow with single photons	75
7.2.4	On the experimental proposal to observe quantum backflow in a TEM	75
	Bibliography	77

List of Figures

1.1	Visualization of double slit interference.	1
1.2	A visual example of a state exhibiting backflow.	5
1.3	The unconventional example of backflow using a slit in momentum space.	6
1.4	Example of counter-propagating paraxial wave-packet.	8
2.1	A Shack-Hartmann Wavefront Sensor.	14
2.2	Detecting the centroids of two Gaussian spots in a spotfield using the stream-processing algorithm.	16
2.3	An illustration of misidentified spots in a simulated spotfield.	17
2.4	Schematic of the experimental setup to measure transverse local momentum of circularly polarized LG beams.	20
2.5	Experimental study of the distinction between canonical momentum and Poynting vector.	21
3.1	Visualization of Backflow in Two-Plane Wave Interference.	24
3.2	Schematic representation of the experimental setup to observe backflow in the x component of the local momentum.	25
3.3	Experimental observation of backflow in transverse momentum.	26
3.4	The effect of the amplitude ratio and the angle between the beams on the observation of backflow.	28
3.5	The effect of non-overlapping beams.	30
3.6	The effect of finite-sized microlenses.	32
4.1	Visualization of the superposition of two beams carrying helical phases.	36
4.2	Schematic representation of azimuthal backflow in the superposition of two beams carrying helical phases at the plane of superposition.	37
4.3	Quantitative comparison between values of b	39
4.4	Visual representation of azimuthal backflow in the superposition of two beams carrying helical phases away from the plane of superposition.	41
4.5	Two-dimensional representation of azimuthal backflow in the superposition of LG beams.	42
4.6	Schematic of the experimental setup to observe azimuthal backflow.	43
4.7	Observation of azimuthal backflow—result and method.	44
4.8	Experimental observation of azimuthal backflow.	45
4.9	Statistical error in measuring local OAM of the superposition.	47
4.10	Examining cross-talks in spotfields—a possible cause of systematic errors.	48
5.1	Simulated spotfield images with added noise.	50

5.2	Simulated local OAM with Poisson noise.	51
5.3	Experimental setup to generate single photons via SPDC and to optimise coincidences between the signal and idler arms.	53
5.4	Schematic representation of the intensified sCMOS camera and the constituents of the image intensifier.	54
5.5	Experimental setup to observe quantum optical backflow with heralded single photons.	55
5.6	Azimuthal backflow observed with an attenuated laser in the single photon counting regime.	56
5.7	Speckle-like spots owing to humidity that condenses on the sCMOS sensor, on account of cooling.	58
5.8	Sample photon spotfield from a Gaussian mask on the SLM and 24 hours of photon acquisition.	59
5.9	Detected spot centroids for the spotfield in Fig. (5.8).	60
5.10	Detected spot centroids and local wave-vectors using heralded signal photons.	61
5.11	Sample of dark counts/ background with the signal photons blocked, collected for 24 hours.	61
6.1	The two modes of operation of the imaging system in a TEM.	65
6.2	A toy model of the setup to observe backflow with electrons.	66
6.3	A set of parameters leading to backflow.	68
6.4	A set of parameters leading to backflow assuming no relative amplitude ratio between the slits.	69
6.5	Images collected in diffraction mode from a TEM using a double slit sample	70

List of Abbreviations

SHWFS	Shack-Hartmann Wavefront Sensor
MLA	Microlens Array
CoM	Center-of-Mass
SOL	Superoscillatory Lens
OAM	Orbital Angular Momentum
LG	Laguerre-Gauss
CMOS	Complementary Metal-Oxide-Semiconductor
II	Image Intensifier
APD	Avalanche Photo-Diode
PPKTP	Periodically Poled K(Potassium) T(Titanyl) P(Phosphate)
SPDC	Spontaneous Parametric Down-conversion
MCP	Microchannel Plate
TEM	Transmission Electron Microscope
DP	Diffraction Pattern
BFL	Back-focal Plane
SAD	Selected Area Diffraction

Physical Constants

Speed of Light $c = 2.997\,924\,58 \times 10^8 \text{ m s}^{-1}$ (exact)
Reduced Planck Constant $\hbar = 1.054\,571\,817 \times 10^{-34} \text{ J s}$

Dedicated to my parents and teachers

Chapter 1

Introduction

A plethora of counterintuitive effects that have been encountered in quantum mechanics can be attributed to the wave nature of matter: tunnelling, superposition, to name a few. Richard Feynman famously said that the double-slit experiment, which provides an example of the superposition principle, is "impossible to explain in any classical way" and "has in it the heart of quantum mechanics. In reality, it contains the only mystery." Admittedly, the advent of entangled states of two or more particles has led to further mysteries. Nonetheless, for the purpose of this dissertation, Thomas Young's double-slit experiment (see Fig. (1.1)) with classical light and its variants, that have since been performed ubiquitously with electrons [1], neutrons [2], photons [3], atoms [4] and molecules [5], merit our attention. A coherent train of particles is shot at two parallel slits and is registered, one by one, on a screen in the far field of slits. An interference pattern emerges on the screen after some time. Thus, the total probability density of finding the particle at any position behind the slits is the modulus square of the sums of the probability amplitudes of arriving at the said position via each of the slits. The striking feature of this experiment is that not only the intensity (energy), but also the phase, of the resultant fields behind the slits, is generally not a spatially homogeneous distribution. This very redistribution of energy and phase allowed by the superposition principle can account for another lesser known and surprising phenomenon called 'backflow'. In general, backflow occurs when wave-functions are a superposition of states carrying entirely positive momenta (Fourier components), and yet their *local* probability current (phase gradient) can sometimes be negative [6].

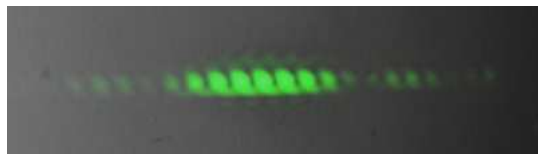


FIGURE 1.1: **Visualization of double slit interference.** Light from a green laser passing through two slits 0.4 mm wide and 0.1 mm apart leads to this pattern of bright and dark fringes in the far field. Source-Wikipedia.

In the late sixties, GR Allcock [7, 8, 9] realised that, for a free particle, obeying the one dimensional Schrödinger equation, described by a wave function centred in $x < 0$ consisting *entirely* of positive momenta, the probability of remaining in $x < 0$ may nevertheless increase with time. That is, the quantum-mechanical current at the origin can be negative and the probability can flow "backwards". In general, the question of 'when' a detector clicks due to a particle or the time-of-arrival problem, is a nuanced one. A state with only positive momentum is such that, if we measure the momentum, then we find a positive value with certainty. This is not equivalent

to stating that the particle moves *only* from the left to the right when we do not measure it. In fact, interference may produce a temporary inversion of the motion at a detector placed at the origin [10, 11]. We can conclude from Allcock's studies that the probability current is not a good measure of the time-of-arrival. Further advances on the time-of-arrival problem were made by Muga *et al.* [12, 13, 14]. Following this, in 1994 [15], a systematic study showed that the probability of the particle remaining in $x < 0$ may increase with time, but only by 4%, at most. More recently, the works of Arseni Goussev and collaborators showed that for charged particles moving on a ring, this bound increases to about 12% [16]. To overcome such bounds that make the experimental observation of the phenomenon difficult, researchers studied backflow in two dimensions for a charged particle moving either in a uniform magnetic field in the infinite (x, y) plane [17, 18] or on a finite disk such that a magnetic flux line passes through the center of the disk [19]. In such two-dimensional systems, the probability of backflow can be unbounded. The effect has also been explored in relativistic wave equations [20, 21].

Notwithstanding the volume of theoretical studies on backflow in quantum mechanics and experiment-friendly proposals [22, 23], there are no known experimental demonstrations of this effect. Nonetheless, the fact that band-limited functions can contain anomalously high (low) local phase gradients, i.e., the concept of superoscillations (suboscillations) in waves, has been noted by Michael Berry, to be equivalent to backflow in quantum mechanics [6]. It was proposed by Berry and Popescu [24] and verified experimentally [25, 26] that the phenomenon of superoscillations can be used to realise far-field sub-wavelength optical focusing without the use of evanescent waves. Other areas of application include optical and electron beam shaping [27, 28] and particle trapping [29]. The reader is referred to a sub-section in (1.2.2) for further insights on the applications of superoscillations in super-resolution imaging.

In 2020, the connection between backflow and suboscillations was utilized by Eliezer *et al.* [30] to experimentally demonstrate anomalous values of transverse local momentum in a complex superposition of optical waves, an analogue of backflow in quantum mechanics. We realised that despite this development, the phenomenon of backflow and its connection to superoscillations, remained somewhat elusive. We, therefore, experimentally demonstrated 'optical' backflow using the simple interference of two beams of unequal amplitudes [31, 32]. In fact, our findings highlight that backflow in these scenarios is very common owing to the practical impossibility of creating the constituent beams with perfectly equal amplitudes. Utilising one-shot measurements allowed by the Shack-Hartmann wavefront sensor (SHWFS), we observe anomalous values of transverse local momentum in the dark fringes of such an interference pattern. We thus experimentally highlighted the connection between high phase gradients and backflow, hitherto merely a theoretical concept. Additionally, as discussed in later chapters, our findings can have implications for studies on optical tweezers [33, 29], for designing ultra-precise atomic clocks [34, 35] and light-matter interaction at large.

The structure of this dissertation is as follows. The above written general introduction to the subject is supported by a technical introduction to the tools required to further understand the subject—a theoretical introduction to backflow in quantum mechanics using tools such a probability density and probability current, parallels between backflow in quantum mechanics and in optics, and an introduction to the concept of local momentum. Once the reader is acquainted with the necessary tools, Chapter 2 provides an introduction to the method of measuring local momentum of optical waves with a Shack-Hartmann wavefront sensor. Furthermore, the detection

technique described in Chapter 2 is utilised in Chapters 3 and 4 to experimentally demonstrate optical backflow using the superposition of two Gaussian beams, two beams carrying orbital angular momentum (azimuthal backflow). Chapter 5 describes an experiment demonstrating azimuthal backflow with single photons and shows that the results are consistent with the classical case. Chapter 6 is a proposal to demonstrate quantum backflow with electrons in a Transmission Electron Microscope (TEM). The dissertation concludes in Chapter 7 with a summary and future plans.

1.1 Backflow in quantum mechanics

In this section, we present a mathematical introduction to the concept of backflow. The knowledge of definitions of quantities from quantum mechanics is assumed.

We consider a free particle with initial position-space wave-function $\Psi(x, 0)$ concentrated in $x < 0$ and consisting entirely of positive momenta p . The position-space wave function is a Fourier transform of the momentum-space wave-function $\Phi(p)$.

$$\Psi(x, 0) = \int_0^{\infty} dp \Phi(p) \frac{e^{ipx/\hbar}}{\sqrt{2\pi\hbar}}, \quad (1.1)$$

$$\int_{-\infty}^{\infty} dx |\Psi(x, 0)|^2 = 1 = \int_0^{\infty} dp |\Phi(p)|^2 \quad (1.2)$$

The time evolution is governed by the one-dimensional Schrödinger equation (in the absence of a potential).

$$i \frac{\partial \Psi(x, t)}{\partial t} = -\frac{\hbar}{2m} \frac{\partial^2 \Psi(x, t)}{\partial x^2}, \quad (1.3)$$

$$\Psi(x, t) = \int_0^{\infty} dp \Phi(p) e^{-i\frac{p^2 t}{2m}} \frac{e^{ipx/\hbar}}{\sqrt{2\pi\hbar}} \quad (1.4)$$

The flow of probability density is governed by the probability current $J(x, t)$. The continuity equation connects the probability density function to the probability current.

$$\frac{\partial |\Psi(x, t)|^2}{\partial t} + \frac{\partial J(x, t)}{\partial x} = 0, \quad (1.5)$$

$$J(x, t) = \frac{\hbar}{m} \text{Im} \left\{ \Psi^*(x, t) \frac{\partial \Psi(x, t)}{\partial x} \right\} \quad (1.6)$$

Let us now consider the probability flux crossing the origin within the time interval $[t_1, t_2]$ [36]. It follows from the integral version of eqn. (1.5) that

$$\int_{-\infty}^0 dx |\Psi(x, t_1)|^2 - \int_{-\infty}^0 dx |\Psi(x, t_2)|^2 = \int_{t_1}^{t_2} dt J(0, t), \quad (1.7)$$

$$\text{Therefore, } P(t_1) - P(t_2) = \int_{t_1}^{t_2} dt J(0, t)$$

Here, $P(t)$ is the probability of the particle remaining in $x < 0$ at time instance t . Thus, for the particle in our consideration, according to its definition, backflow occurs when $P(t_1) - P(t_2) < 0$ for $t_1 < t_2$. More specifically, as seen from eqn.(1.7), although the momentum is positive with 100% certainty, backflow can occur when the probability current at the origin, $J(0, t)$, is negative.

Over the years, several specific examples of $\Psi(x, 0)$ have been shown to exhibit backflow (the superposition of two plane waves carrying only positive momenta [15], states exhibiting maximum backflow [37]). Even the superposition of two Gaussian wavepackets, although not containing only positive momenta, can allow us to observe backflow [36]. See Fig. (1.2) for a visual example (without associated mathematical expressions) of the well-known superposition of two Gaussian wavepackets exhibiting backflow. Subplots (A) and (B) show the probability density, in momentum and position space respectively, of the two Gaussian wavepackets of unequal amplitudes. Subplot (C) is a bird's-eye view of the probability density as a function of position and time. If a screen is placed at $x = 0$, then the probability current, plotted in (D), negative in some instances of time, can be recorded. For further details, the reader is referred to the figure's caption.

We also mathematically describe below a simple experimentally realizable example of a slit in momentum space that, to the best of our knowledge, hasn't been explored previously. We will refer to this example later in Chapter 7.

1.1.1 An unusual example of a state exhibiting backflow

Let us consider the particle's momentum space distribution to be a small slit centered around positive value p_0 with a width of Δ_p . The momentum distribution is plotted in Fig. (1.3a). Also see Fig. (1.4a) for a schematic representation using an optical model. Therefore, using eqn. (1.1), the momentum and initial position space (obtained by Fourier transforming the former) wave-functions are as follows.

$$\begin{aligned}\Phi_1(p) &= \frac{1}{\sqrt{\Delta_p}} \left[\Theta\left(p - \left(p_0 - \frac{\Delta_p}{2}\right)\right) - \Theta\left(p - \left(p_0 + \frac{\Delta_p}{2}\right)\right) \right], \\ \Psi_1(x, 0) &= \sqrt{\frac{2\hbar}{\pi\Delta_p}} \frac{e^{ip_0x/\hbar}}{x} \sin\left(\frac{\Delta_p}{2\hbar}x\right)\end{aligned}\quad (1.8)$$

Here, $\Theta()$, is the unit step function [38]. According to eqn. (1.4), the wave-function at a later time instance is given by

$$\Psi_1(x, t) = \frac{e^{-ip_0^2t/2\hbar m + ip_0x/\hbar}}{\sqrt{2\pi\hbar\Delta_p}} \int_{-\Delta_p/2}^{\Delta_p/2} dp e^{-p^2t/2\hbar m} e^{ip(x-p_0t/m)/\hbar} \quad (1.9)$$

After a suitable change of coordinates, the probability density can be expressed as follows.

$$|\Psi_1(x, t)|^2 = \frac{1}{2\pi\hbar\Delta_p} \int_{-\Delta_p/2}^{\Delta_p/2} du \int_{-\Delta_p+2|u|}^{\Delta_p-2|u|} dv e^{iv[x-(p_0+u)t/m]/\hbar} \quad (1.10)$$

Let us now mathematically express the probability of the particle to remain in $x < L$ at time t , where L is not necessarily the origin.

$$\begin{aligned}P(t|x < L) &= \int_{-\infty}^L dx |\Psi_1(x, t)|^2 \\ &= \frac{1}{2} + \frac{1}{\pi\Delta_p} \int_{-\Delta_p/2}^{\Delta_p/2} du \int_0^{[L-(p_0+u)t/m](\Delta_p-2|u|)/\hbar} dv \frac{\sin v}{v}\end{aligned}\quad (1.11)$$

For the ease of our calculations, we can introduce the following dimensionless parameters— $\alpha = \frac{L\Delta_p}{\hbar}$, $\beta = \frac{2p_0}{\Delta_p}$, and $\tau = \frac{\Delta_p^2}{2\hbar m}t$. Once the integration variable is changed to $\tilde{u} = \frac{2u}{\Delta_p}$,

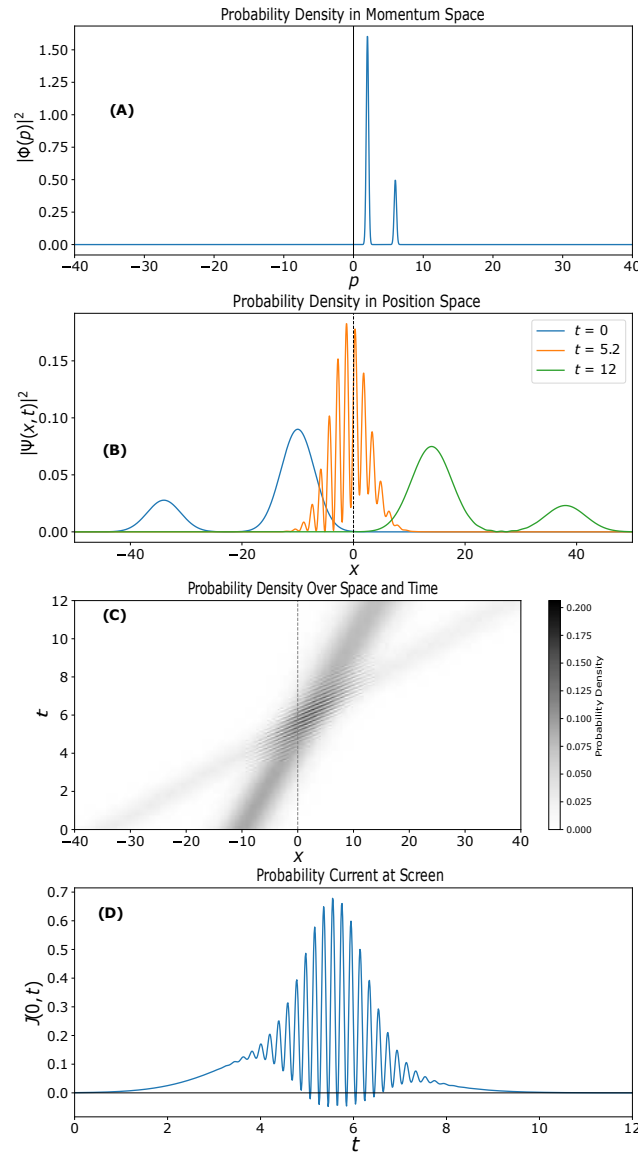


FIGURE 1.2: **A visual example of a state exhibiting backflow.** Two Gaussian wavepackets initially centered in $x_1 = -10$ and $x_2 = -34$, both with initial variance of position equal to 3, move with average momentum $p_1 = 2$ and $p_2 = 6$, respectively. The variance in momentum is $1/6$. The first wavepacket is higher in amplitude than the second by a factor of 1.8. All parameters are dimensionless and \hbar and m are chosen to be unity for the sake of simplicity. It is assumed that a detector is placed at $x = 0$ (indicated by dashed lines in the plots). (A) The distribution of probability in momentum space is chosen to be quite narrow. Thus, negative value of momenta arising from this distribution can be neglected for all practical purposes. (B) The probability density $|\Psi(x, t)|^2$ as a function of position, at three different times (t) are plotted. The second packet overcomes the first when they are both in the region around the origin, where the detector is placed. In this area the two packets interfere, but then they separate again at a later time. (C) The probability density of the position as a function of position and time are shown. (D) The probability current $J(0, t)$ at the detector as a function of time. Negative values indicate backflow.

the flux crossing L within the time interval $[t_1, t_2]$ can be expressed as follows.

$$\begin{aligned}
 P(t_1|x < L) - P(t_2|x < L) &= \frac{1}{2\pi} \int_{-1}^1 d\tilde{u} \int_{(\alpha - \beta\tau_2 - \tau_2\tilde{u})(1 - |\tilde{u}|)}^{(\alpha - \beta\tau_1 - \tau_1\tilde{u})(1 - |\tilde{u}|)} dv \frac{\sin v}{v} \\
 &= \frac{1}{2\pi} \int_{-1}^1 d\tilde{u} [\text{Si}\{(\alpha - \beta\tau_1 - \tau_1\tilde{u})(1 - |\tilde{u}|)\} - \text{Si}\{(\alpha - \beta\tau_2 - \tau_2\tilde{u})(1 - |\tilde{u}|)\}]
 \end{aligned} \tag{1.12}$$

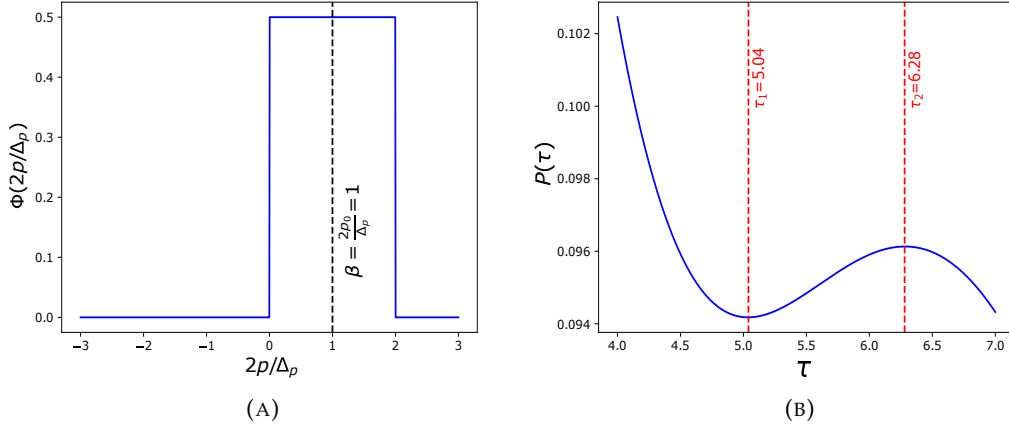


FIGURE 1.3: **The unconventional example of backflow using a slit in momentum space.** A slit in momentum-space exhibits backflow in position-space. Parameters: $\alpha = 0$; $\beta = 1$. (A) Momentum space wave-function with scaled coordinates. (B) Probability of remaining in $x < L$, where $L = 0$; grows by 0.2% between τ_1 and τ_2 . Consequently, the intensity $|\Psi_1(x, t)|^2$ crossing $x > L$ grows between t_1 and t_2 grows by 0.2%, for the right set of physical parameters.

Here, $\text{Si}(x) = \int_0^x \frac{dv}{v} \sin(v)$. Given L , for suitably chosen values of the parameters, α and β , times τ_1 and τ_2 can be found such that the above-written flux (and the probability current) is negative between them. As seen in Fig. (1.3b), quite surprisingly, the probability to remain in $x < 0$ grows with time for the interval between τ_1 and τ_2 . The probability current at $x = 0$, or the rate of change of probability, is also negative. The analogy between the probability current in optics and the Poynting momentum for scalar optical fields is discussed in the following section.

1.2 Backflow in optics

Optical backflow or counter-propagation in both transverse and longitudinal directions have been theoretically explored in [6]. Counter-propagation in the transverse direction for certain paraxial wave-packets, follows naturally from the mathematical equivalence between the paraxial Helmholtz equation and the Schrödinger equation.

1.2.1 Counter-propagating solutions to the paraxial Helmholtz equation

In the paraxial approximation of the Helmholtz equation, the complex amplitude $A(x, y, z) = u(x, y, z)e^{ikz}$ contains a sinusoidal plane wave represented by the exponential factor and $u(x, y, z)$ which approximately solves

$$i\frac{\partial u(x, y, z)}{\partial z} = -\frac{1}{2k}\nabla_{\perp}^2 u(x, y, z), \quad (1.13)$$

where ∇_{\perp} is the transverse Laplacian operator and $k = 2\pi/\lambda$, the wavenumber and is equivalent to m/\hbar in eqn. (1.3). Here, z , is the primary direction of propagation and is equivalent to t in eqn. (1.3).

Consider a generic one-dimensional monochromatic scalar wave with boundary value

$$A(x, z = 0) = \sum_{n=0}^N c_n e^{ik_n x}, \quad (1.14)$$

where $k_n \geq 0$ are the transverse momenta of the constituent plane waves with $\max\{k_n\} \ll k$ and c_n are complex to account for relative phases between the constituents. Thus, $A(x, z = 0)$ is a generic superposition of plane waves with each constituent travelling to the right (positive x). Assuming that the wave is travelling in the positive z direction, the solution of eqn. (1.10) is

$$A(x, z) = e^{ikz} \sum_{n=0}^N c_n e^{i(k_n x - \frac{k_n^2 z}{k})} \quad (1.15)$$

Following the equivalence between eqns. (1.11) and (1.2), backflow in the x, z plane, i.e., leftward propagation over some slices of forward propagation, is identical to the above described backflow in the spacetime plane x, t [6].

Let's now revisit the familiar example of the single slit centered around a positive $x' = x_0$ (1.1.1). As shown in Fig. (1.4a), let's consider a one-dimensional aperture of width Δ in the front-focal plane of a convex lens with normalized amplitude transmittance given by $\frac{1}{\sqrt{\Delta}} \text{rect}\left(\frac{x' - x_0}{\Delta}\right)$, where $\text{rect}()$ is the rectangular function [39], illuminated by a monochromatic plane wave. The field at the back-focal plane of the lens is a Fourier transform evaluated at $\xi/\lambda f$:

$$U_f(\xi) = -i\sqrt{\frac{\Delta}{\lambda f}} e^{-i2\pi x_0 \frac{\xi}{\lambda f}} \text{sinc}\left(\frac{\Delta \xi}{\lambda f}\right). \quad (1.16)$$

Here $\text{sinc}(x) = \sin(\pi x)/(\pi x)$ and $\lambda = 2\pi/k$ is the wavelength. It may be verified that the field in eqn. (1.16) is normalized to 1 over all of ξ -space. Utilising the Fresnel integral [40], the field that propagates from the back-focal plane of the lens is given by

$$A(x, z) = -i\frac{e^{ikz}}{\sqrt{\lambda f \Delta}} e^{-i\frac{kz x_0^2}{2f^2}} e^{-i\frac{kx x_0}{f}} \int_{-\Delta/2}^{\Delta/2} d\xi e^{-i\frac{kz \xi^2}{2f^2}} e^{i\frac{k\xi}{f}[x + \frac{x_0 z}{f}]} \quad (1.17)$$

Eqn. (1.17) is quite similar to eqn. (1.9), barring some unimportant phase factors. All rays are assumed to be paraxial, i.e., close to the optical axis with low angles of diffraction. Thus, following a similar method, it can be shown that the probability of the photon/electron in a transmission electron microscope re-entering in $x > L$ at

propagation distance z : is expressed as follows.

$$P(z|x > L) = \frac{1}{2} - \frac{1}{2\pi} \int_{-1}^1 d\tilde{u} \text{Si}((\alpha - \beta\tilde{z} - \tilde{z}\tilde{u})(1 - |\tilde{z}|)), \quad (1.18)$$

where $\alpha = \frac{k\Delta L}{f}$, $\beta = \frac{2(-x_0)}{\Delta}$, $\tilde{z} = \frac{k\Delta^2 z}{2f^2}$, and the integration variable \tilde{u} are dimen-

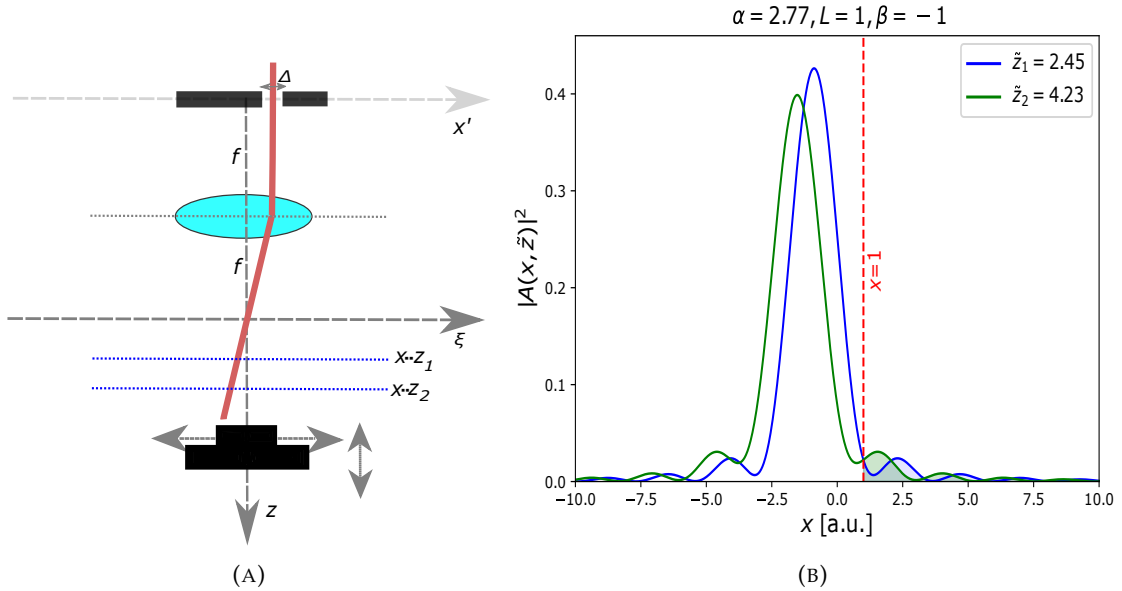


FIGURE 1.4: Example of counter-propagating paraxial wave-packet. (A) Simple optical setup to observe backflow using a single slit. After the back-focal plane of the intensity of the electron beam should propagate towards the negative x . However, backflow occurs when the intensity moves back to the positive x between planes z_1 and z_2 . The intensity at any $x - z$ plane can be measured by appropriately scanning a camera. A growth in the intensity integrated over the right half plane of the camera should be observed between z_1 and z_2 . All angles are small such that the paraxial approximation is valid. (B) The normalised intensity given by $|A(x, \tilde{z})|^2 = \frac{\alpha}{4\pi L} \int_{-1}^1 d\tilde{u} \int_{-(1-|\tilde{u}|)}^{(1-|\tilde{u}|)} d\tilde{v} e^{i\tilde{v}[\frac{\alpha}{L}x - \tilde{z}(\beta + \tilde{u})]}$ grows towards the positive x direction, across $x > L = 1$ at a larger propagation distance \tilde{z}_2 compared to \tilde{z}_1 by about 0.5%. This is verified by comparing the area of the green shaded region to that of the blue shaded region. Here, x and L are in the same units (a.u.). The parameters α , β and L are specified in the plot.

sionless parameters, similar to those in eqn. (1.12). As seen from the expressions of α in eqns. (1.12) and (1.18), momentum-space under the paraxial approximation, is conjugate-position-space, scaled appropriately by the product of wavelength and focal length. Hence, as shown in Fig. (1.3), the parameters $\alpha = 0, \beta = -1$, allow for around 0.2% backflow between $\tilde{z}_1 = 5.04$ and $\tilde{z}_2 = 6.28$. Corresponding sets of physical parameters, viable under the paraxial approximation can also be found. In Chapter 6, this concept will be explored further. However, in order to understand the contents of Chapters 2-5, the next section, which doesn't involve any evolution or propagation, can be useful.

1.2.2 Anomalous values of local transverse momentum

Let us reconsider the generic one-dimensional monochromatic scalar wave with boundary value $A(x) = \sum_{n=0}^N c_n e^{ik_n x}$, where $k_n \geq 0$ are the transverse momenta of the constituent plane waves and c_n are complex (c.f. eqn. (1.14)). It may appear that the wave travels only towards positive x at $z = 0$. However, depending on the values of c_n , this may not be true. In order to understand this further, let us express the wave in the following integral form [6].

$$A(x) = \rho(x) \exp \left\{ i \int_0^x dx' k(x') \right\}, \quad (1.19)$$

in which both the amplitude $\rho(x)$ and the local wavenumber (gradient of phase of the wave)

$$k(x) = \partial_x \arg A(x), \quad (1.20)$$

are real. The local wavenumber can also be expressed as a real weak value of the momentum operator post-selected in position [41] $-k(x) = \text{Re} \frac{\langle x | \hat{k} | A \rangle}{\langle x | A \rangle}$. When $k(x) > 0$, the wave locally travels forward; when $k(x) < 0$, the wave locally travels backwards in certain regions of x and this can occur even when $k_n \geq 0$. In general, when $k(x)$ varies in scales unrepresented by the Fourier spectrum, super or suboscillations or backflow, can occur [24]. In fact, there is no fundamental limit on how large or small the local wavevenumber can be. As a result, the free-space optical field created by the interference of several band-limited waves, such as by diffraction of a plane wave on a structured mask, can have deeply sub-wavelength spatial features [26]. Such features can be used for super-resolution imaging [42] (see sub-section below); the disadvantage is that they are associated with regions of low intensity surrounded by high intensity side lobes. Michael Berry proposed to use combinations of frequencies below 1 Hz (well below the human hearing range) to reproduce Beethoven's ninth symphony [43]. However, the signal strength required for this is $\exp\{10^{19}\}$ times conventional signals.

For scalar fields, the Poynting vector is co-directional with the local wave-vector (x -component in eqn. (1.17)) [44].

$$P(r) = \text{Im} \{ A^*(r, z) \nabla A(r, z) \} = |A(r, z)|^2 \nabla \arg A(r, z) \quad (1.21)$$

The similarity between the expressions of the quantum mechanical current in eqn. (1.6) and the Poynting vector in eqn. (1.21), for scalar fields, suggests that, for such fields, anomalous values of the Poynting vector/local wave-vector components correspond to backflow in optics. However, the local wave-vector and the Poynting vector are not necessarily co-directional for vector fields and Chapter 2 sheds light on this. A description of our experiments measuring anomalous local momenta at a chosen z plane are presented in Chapters 3 and 4.

Using superoscillations for super-resolution imaging

As explained earlier in section (1.2.2), and in the upcoming chapters, this dissertation emphasizes our experimental investigation into the superoscillatory (Faster than Fourier) behavior of local phase gradients, characterized by anomalously steep phase changes within confined spatial regions. In contrast, recent research has focused on combining multiple coherent sinusoidal components to generate super-oscillatory sub-diffraction intensity hotspots with optical wave-functions [45, 42,

46] and electron wave-functions [28]. In fact, it can be shown using the Helmholtz equation that such intensity hotspots naturally arise when local phase gradients are anomalously high [45].

Such intensity hotspots have previously been engineered by directing light through nanohole arrays [25, 47] (often referred to as a Superoscillatory lens (SOL)) and have been explored as a means of achieving super-resolution without relying on evanescent waves [24]. However, a significant limitation is the reduced intensity and the presence of brighter sidebands as the hotspots become smaller. The energy in these sidebands grows exponentially with their separation distance but only polynomially with the inverse of the hotspot size (or equivalently with the superoscillation rate) [48]. This implies that maintaining the same power level in the hotspot requires only a polynomial increase in the total power of the light source.

Recently, superoscillatory microscopy has been successfully demonstrated for label-free imaging of living biological cells [49]. For practical applications, a conventional microscope objective lens cannot simply be replaced with a superoscillatory lens (SOL). When imaging objects larger than the field of view (limited by the separation between sidebands, i.e., the diameter of the halo), light scattering from halo-illuminated regions distorts the images. This issue can be addressed in a confocal microscope setup by using a conventional high-numerical-aperture objective lens while illuminating the sample with a tightly focused superoscillatory pattern (the SOL). Imaging is achieved by scanning the sample relative to the SOL focus and employing a detector with a small confocal aperture to reject most of the scattering from halo-illuminated areas. Superoscillatory illumination of the object, thus, creates a superoscillatory image.

1.3 Concluding remarks

The term ‘quantum backflow’ underscores the stark contrast between classical and quantum dynamics of particles– a tennis ball, while moving forward with strictly positive momentum, cannot suddenly change its course but an electron moving forward with strictly positive momentum, can have an increasing probability to be found backwards at later instances of time. However, the broader concept of ‘backflow’, resulting from wave interference, is ubiquitous in systems supporting coherent waves. Related to this, there is an ongoing debate on the interpretation of backflow as a purely quantum phenomenon [21, 50, 51, 52].

The measurement of transverse local momentum was previously used to plot Bohmian trajectories of photons [53]. Later, a classical interpretation of this experiment with the concept of momentum weak-values was provided by Bliokh *et al* [54].

The notion that the center-of-mass (CoM) of a wave-packet in free space propagates along straight trajectories is in accordance with Ehrenfest’s theorem [55]. This is also observed in example given in Fig. 1.4b, wherein the CoM of the beam moves to the left between \tilde{z}_1 and \tilde{z}_2 . However, the straight-line motion of the CoM, doesn’t restrict the growth in the intensity measured on the right of $x = 1$ between \tilde{z}_1 and \tilde{z}_2 . This behaviour can be observed from the intensity cross-sections on just two $x - z$ planes. In a somewhat similar yet distinct manner, in accelerating beams [56], while the CoM propagates along a straight line, the peak intensity accelerates along the direction of propagation. In order to observe this, one needs to measure the intensity cross-section across at least three different $x - z$ planes. Additionally, a purely positive (negative) momentum distribution (c.f. Fig. 1.3a), that gives rise to backflow, cannot produce accelerating beams.

A direct mathematical connection between states exhibiting anomalous transverse local momentum at a given z plane and those exhibiting counter propagation in z , hasn't yet been firmly established.

Contributions: The author developed the structure and content of this chapter. She expresses her gratitude to Prof. Tomasz Paterek, Dr. Arseni Goussev, and Prof. Thomas Juffmann for their invaluable discussions, exchange of ideas, and shared insights, which greatly contributed to the writing of this chapter.

Chapter 2

Transverse local momentum and its measurement

The purpose of this chapter is to introduce the measurement of local transverse momentum (see eqn. (1.20)) using a microlens array focusing onto a CMOS (complementary metal-oxide-semiconductor) device, a combination known as the Shack-Hartmann wavefront sensor (SHWFS) [57]. As described in [30] (see Fig. 2), the transverse local momentum can also be measured by isolating regions in the position space with a slit and following this up with Fourier transform using a lens. However, this method involves scanning the slit across the position space. Contrariwise, the Shack-Hartmann wavefront sensor enables single-shot measurements of local momentum.

The second part of the present chapter discusses the connection between local momentum and the Poynting vector for vector fields. For linearly polarized, i.e., spinless fields, the two are co-directional.

2.1 Measuring local momentum using the Shack-Hartmann wavefront sensor

As shown in Fig. (2.1) pattern of spots (spotfield; Fig. (2.1b)) is formed as each lens of the microlens array focuses an area of the incoming wavefront (locus of all points having the same phase) onto the corresponding region on the CMOS sensor at the back-focal plane of the array. In accordance with the principle of the SHWFS, a reference spotfield is generated by impinging a reference beam such as a wide Gaussian beam on the microlens array. The transverse displacement of each spot in the spotfield of the incoming wavefront with respect to the corresponding spot in the spotfield of the reference wavefront is measured. As we shall show here, these displacements are proportional to the transverse local wave-vector components. This wave-front sensor works under the assumption that the spots in the spotfield of the incoming wavefront are distinct and don't overlap.

Fig. (2.1a) is an example of a commercially available microlens array with a pitch (d) of 150 μm and focal length $f_m = 5.6$ mm (of each microlens). Fig. (2.1c) is a schematic representation of the side-view of such a microlens array focusing on a CMOS sensor. As seen from geometric considerations, the y -component of the gradient of the wavefront impinging on the i -th microlens, is proportional to $\Delta y_i / f_m$, under the small angle approximation. We thus have,

$$k_{x,i}, k_{y,i} = \frac{2\pi}{\lambda} \left(\frac{\Delta x_i}{f_m}, \frac{\Delta y_i}{f_m} \right) \quad (2.1)$$

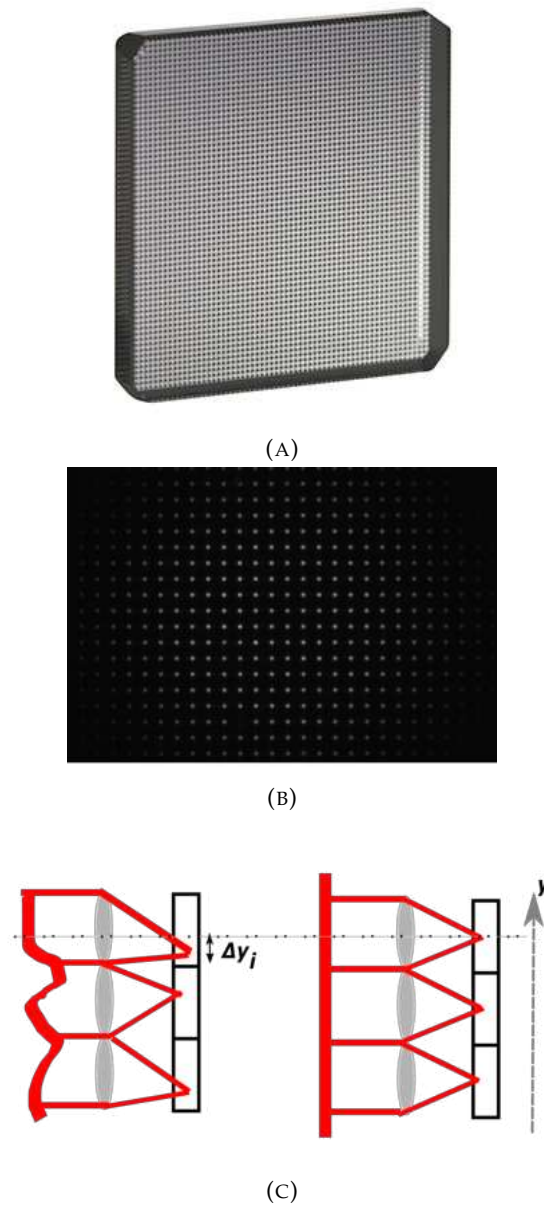


FIGURE 2.1: **A Shack-Hartmann Wavefront Sensor.** (A) A commercially available two-dimensional microlens array. Thorlabs MLA150-5C - 10 mm x 10 mm. (B) A sample spotfield due an incoming spherical wavefront generated when the microlens array in (A) focuses on a CMOS device. (C) Concept of the setup. Consider a distorted wavefront impinging on the microlens array (side view). Following the Shack-Hartmann technique, by finding the centroids of the spot-field and measuring their displacement Δy_i with respect to a reference, the wavefront is reconstructed. The local wave-vector is derived for the i -th microlens.

The maximum possible displacement in x or y without making the spots overlap is half of the pitch ($d/2$). In general, while the scales in which Δx_i and Δy_i vary are in the range of sub-pixels of the CMOS device, $d/2$ is usually in the range of several pixels. In the event that a microlens intercepts a few (N) photons (N independent events), then, the uncertainty, in measuring the local momentum behind it, in the x or y direction is $\frac{2\pi}{\lambda} \frac{\pm d/2}{f_m \sqrt{N}}$ [58]. When there is enough light, the above-described uncertainty due to Poisson noise is insignificant. Under these circumstances, the sub-pixel displacement of each spot in the spotfield with respect to a reference, is relevant. Displacements in the range of camera sub-pixels can be measured by employing an algorithm discussed in [59]. A brief review of this algorithm is presented below.

2.1.1 Algorithm to measure centroid displacements

A typical method to estimate the centroid/CoM coordinates of a focal spot on the CMOS is to multiply the position of each pixel (i) with its associated intensity ($I(i)$), sum this product over all the pixels ($-M \leq i \leq M$) and divide the sum by the sum of intensities over all the pixels. Thus, in a simple one-dimensional scenario, the x coordinate of the centroid/CoM is the following.

$$\hat{C}_x = \frac{\sum_{i=-M}^M iI(i)}{\sum_{i=-M}^M I(i)}. \quad (2.2)$$

The accuracy of the displacement measurements discussed above is directly related to the method used to estimate the centroid of a focal spot. A challenge of centroid estimation is to identify the useful signal within a sub-aperture on the detector. For the experiments discussed in this dissertation, we use a centroid estimation method proposed by Kong *et al.* [59], based on stream processing, wherein a floating window can be selected to match the spot size without cutting off useful signal pixels. This approach of using a CoM window that floats with the incoming pixel of the detector is known to be useful for reducing the effects of background and noise compared to the traditional CoM approach in eqn. (2.2).

The numerator in eqn. (2.2) can be interpreted as the sum of a multiplication between a linear filter $F(i) = [-M, \dots, M]$ of size $2M + 1$ and the intensity distribution $I(i)$. The denominator can also be interpreted as the same operation, but with a filter $J(i) = 1, \forall i \in [-M, \dots, M]$. Thus, applying the aforementioned filters to all the pixels, the x coordinate of the centroid in eqn. (2.2) can be used to calculate another quantity— $\hat{C}_x(i)$, the center-of-mass of intensity $I(i)$, at the i -th pixel, calculated and centered on the same pixel location.

$$\hat{C}_x(i) = \frac{\sum_{m=-M}^M F(m)I(i+m)}{\sum_{m=-M}^M I(i+m)} = \frac{F(i) * I(i)}{J(i) * I(i)}, \quad (2.3)$$

where, $*$ denotes correlation. $\hat{C}_x(i)$ represents the estimated centroid of different parts of the signal $I(i)$. In order to further understand this, let us reconsider the filter $F(m) = m - M, \forall m \in [-M, \dots, M]$. The expression on the left hand side, in eqn. (2.3) can then be modified as follows.

$$\hat{C}_x(i) = \frac{\sum_{m=-M}^M mI(i+m)}{\sum_{m=-M}^M I(i+m)} - M \quad (2.4)$$

This form of the expression makes it evident that the action of the operator \hat{C}_x on the i -th pixel, tells us whether the centroid of $I(i)$ is to left or right of the said pixel. As we shall see in the example below, much like that of the derivative of intensity across a spot, the sign of $\hat{C}_x(i)$ changes as we cross the centroid/center-of-mass (CoM) of the entire spot. Such zero-crossing of $\hat{C}_x(i)$ allow us to determine the centroid of a spot. In general, the lengths of the filters $F(i)$ and $J(i)$ do not need to be the same as that of $I(i)$.

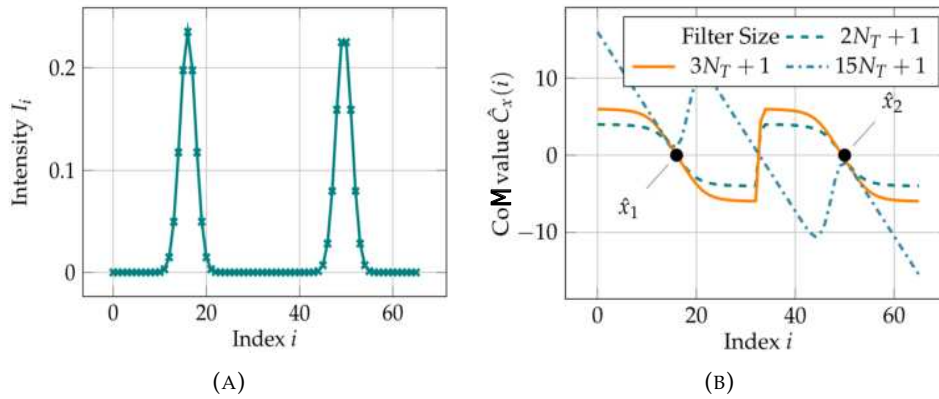


FIGURE 2.2: **Detecting the centroids of two Gaussian spots in a spotfield using the stream-processing algorithm.** Adapted from [59]. (A) The intensity distribution (per pixel on the camera)– $I(i)$ –of a one-dimensional signal that is a concatenation of two Gaussians. The Full-width-half-maximum (FWMH) of each Gaussian is $N_T = 4$ pixels and together they span over 33 pixels. While, the peak of the Gaussian on the left sits on pixel number i_1 , that of the Gaussian on the right is situated at the middle of two pixels, i.e., has a sub-pixel location. (B) Estimated centroids for different pixels parts of $I(i)$ – $\hat{C}_x(i)$ –are calculated for different filter sizes. A zero-crossing from positive to negative values of $\hat{C}_x(i)$, indicates a detected spot centroid. When the filter size is increased to $15N_T + 1$, the centroid of the concatenation is detected instead of the individual centroids. The optimized width of the filter is, approximately, the size of each spot– $2N_T + 1$.

In Fig. (2.2), which is adapted from [59] (Fig. (1)), the centroid of the Gaussian on the left $\hat{x}_1 = i_1$. However, the centroid of the spot on the right \hat{x}_2 , sits between $i_2 - 1$ and i_2 . Assuming that $\hat{C}_x(i)$ is linear between the $i_2 - 1$ -th pixel and the i_2 -th pixel and i_2 is the first pixel with negative $\hat{C}_x(i)$ value, we have

$$\hat{x}_2 = i_2 + \frac{\hat{C}_x(i_2)}{\hat{C}_x(i_2 - 1) - \hat{C}_x(i_2)} \quad (2.5)$$

Relevant codes in Python to implement the above described algorithm in two dimensions can be found in the following [Github repository](#). The latest version of the code was written by Bernard Gorzkowski.

2.1.2 How ‘local’ is local momentum?

It is well known [40], that the width d of the central Airy lobe, in x or y directions, generated at the back-focal plane of a lens, when the incoming beam covers the entire

surface of the lens of diameter D and focal length f_m , is

$$d = \frac{1.22\lambda f_m}{D} \quad (2.6)$$

If the focal length and diameter of the lens are changed proportionately, then d remains the same. However, increasing D , can cause a loss of sampling of the features of the wavefront. Akondi *et al.* discuss errors that might arise due to non-uniform illumination on microlenses [60]. Spotfields can be simulated by means of two-dimensional convolution of the Fourier transform of the part of the field impinging on a microlens and an Airy spot produced at the focal plane of the microlens. The local momentum obtained from detecting the displacements of the centroids in the simulated spotfield, with respect to a reference, can then be compared to mathematically expected local momentum, in order to identify imperfections due to the finite size of the microlenses. A version of this code can also be found in the aforementioned Github repository.

2.1.3 The algorithm's error in estimating a spot's centroid

Due to the boundary effect and noise, the stream processing algorithm may misidentify fake spots as potential centroids (c.f. Fig. (2.3)). Hence, a threshold must be applied to the local sum of pixels within the center of gravity window to eliminate those fake spots. However, in extreme situations, adaptive optics systems have to work under strong noise and weak signal conditions. Besides, there may exist strong interference of light from the environment. Fake spots may be brighter than real spots, and if the spot is not detected, centroid calculation with such methods is completely wrong [61].

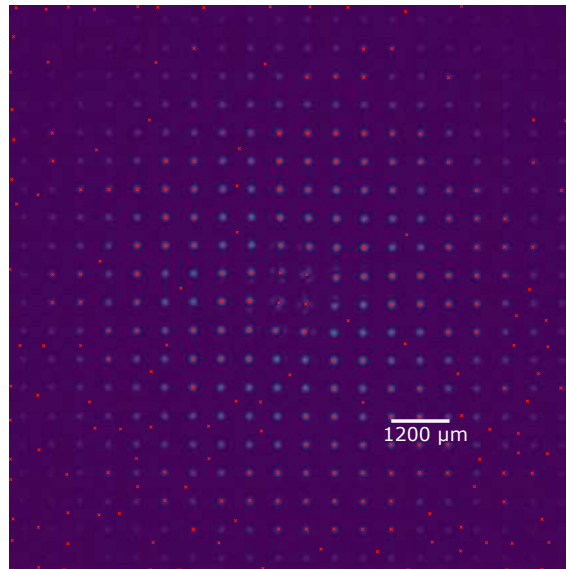


FIGURE 2.3: **An illustration of misidentified spots in a simulated spotfield.** A spotfield was simulated, assuming the wavefront to be helical (carrying orbital angular momentum). Poisson noise and Gaussian readout noise were included in the simulation. Identified centroids are marked with red crosses. While many real centroids are undetected, several fake centroids are identified.

2.2 The connection between local momentum and Poynting vector

Most textbooks on optics and electromagnetism (Born and Wolf [62], for instance) introduce the Poynting vector as the main and only quantity characterizing the momentum or energy-flux density. While the Poynting vector is universally well defined for arbitrary electromagnetic fields in any media, it is not directly observable in standard optical experiments as it does not determine the optical force on small particles. Additionally, if only the Poynting vector is considered, then difficulties arise in determining the spin and orbital parts of the angular momentum of light [63]. In order to overcome these challenges, more recently, an alternative *canonical* (also called 'orbital') momentum density (so far called the local momentum in this dissertation) was introduced for monochromatic structured optical fields in free space or isotropic media [64, 54]. Specifically, in [54] it was shown that local differences between the Poynting vector and the canonical momentum can cause discrepancies such as the circular-polarization-dependent components of the Poynting vector orthogonal to the canonical momentum. It has already been established that small probe particles or atoms experience local optical forces proportional to the canonical momentum density (while the contribution proportional to the Poynting vector is much weaker) [65, 66]. Here, in contrast to the optomechanical methods, we utilize the SHWFS to measure the local momentum of circularly polarized vortex beams [67].

The time-averaged energy density W , Poynting momentum density Π , and canonical momentum density P , for monochromatic paraxial optical fields in free space can be written, as follows, in Gaussian units omitting inessential common factors, and using the equivalence of the electric and magnetic field contributions under the paraxial approximation [64].

$$\begin{aligned} W &\simeq |E|^2, \\ \Pi &= \frac{1}{c} \text{Re}\{E^* \times H\}, \\ P &\simeq \frac{1}{\omega} \text{Im}\{E^* \cdot \nabla E\} \end{aligned} \quad (2.7)$$

As discussed earlier in section (1.2.2), the canonical momentum density represents a natural optical counterpart of the probability current ($J(x, t)$) in quantum mechanics and, as is evident from its expression (P in eqn. (2.7)), essentially the local wave-vector multiplied by the intensity. It can also be associated with the 'weak' value of the canonical momentum operator $\hat{p} = i\nabla$.

The local difference between Π and P can be determined by the spin momentum density S .

$$\begin{aligned} \Pi &= P + \frac{1}{2} \nabla \times S, \\ S &\simeq \frac{1}{\omega} \text{Im}\{E^* \times E\} \end{aligned} \quad (2.8)$$

Let us now study circularly polarized Laguerre-Gauss beam with zero radial index (see [68] for expressions of the transverse and longitudinal electric field components) using the Shack-Hartmann wavefront sensor. Previous studies of vortex beams using the Shack-Hartmann wavefront sensor [69, 70] dealt with linearly polarized paraxial beams and hence didn't note the difference between canonical and Poynting momentum densities (recall from eqn. (1.21) that the two are co-directional

for scalar fields).

2.2.1 The Poynting-canonical dilemma in circularly polarized vortex beams

For circularly polarized Laguerre-Gauss (LG) beams [68] with zero radial index, the expressions for energy density, canonical momentum density, and Poynting momentum density are the following respectively.

$$W = \frac{r^{2|\ell|}}{w(z)^{2|\ell|+2}} e^{-\frac{2r^2}{w(z)^2}} \quad (2.9)$$

$$P = \frac{1}{c} \left(\frac{\ell}{kr} \hat{\phi} + \frac{r}{R(z)} \hat{r} + \hat{z} \right) W \quad (2.10)$$

$$\Pi \simeq \frac{1}{c} \left[\left(\frac{\ell}{kr} - \frac{\sigma|\ell|}{kr} + \frac{2\sigma r}{kw(z)^2} \right) \hat{\phi} + \frac{r}{R(z)} \hat{r} + \hat{z} \right] W \quad (2.11)$$

Here, $w(z)$ is the Gaussian-envelope radius at propagation distance z involving the waist radius w_0 and the Rayleigh diffraction length $z_R = kw_0^2/2$ ($k = \omega/c$ is the wavenumber): $w(z) = w_0 \sqrt{1 + z^2/z_R^2}$. $R(z) = z(1 + z^2/z_R^2)$ is the radius of curvature of the wavefront. ℓ is the azimuthal index and $\sigma = \pm 1$ denotes the helicity of circular polarization.

Fig. (2.4) illustrates a schematic of the experimental setup. The LG beams, with azimuthal indices $\ell = 0, \pm 1$ were generated by using phase masks displayed on a phase-only spatial light modulator, as shown in the inset A of Fig. (2.4). A continuous wave laser with the wavelength $\lambda = 780$ nm (Thorlabs CLD1015) was expanded and directed onto the SLM. To simultaneously modulate phase and amplitude using a phase-only SLM, the technique described in [71] was employed, such that the desired field was obtained after filtering the first diffraction order. Polarizer P1 was used to set the linear polarization of the incident beam prior to the SLM. Then, the light reflected from the SLM was converted to have circular polarization using a quarter wave plate (QWP) oriented at 45° with respect to P1. Polarizer P2 was used to determine the orientations of the fast and slow axes of the QWP, and it was removed after that. Also, to determine the circular-polarization helicity σ , a Q-plate (QP) of the order $q=1/2$ (Thorlabs-WPV10L-780) was employed [72] and removed afterwards. This procedure ensured the generation of LG beams with the desired circular polarization.

Next, the SLM was imaged using lenses L3 and L4 onto the microlens array (ThorLabs-MLA-150-5C-M; each lens has a pitch of $150 \mu\text{m}$ and a focal length of 5.6 mm) that focused the beam onto the CMOS camera (mvBlueFOX-200wG, pixel size $6 \mu\text{m}$). The inset B in Fig. (2.4) depicts the spotfield pattern generated on the CMOS when the mask shown in the inset A was applied on the SLM. To create a reference spotfield for the Shack-Hartmann Wavefront Sensor (SHWFS), a wide Gaussian beam hologram was displayed on the SLM, and the reflected light was similarly imaged onto the microlens array. For the reference beam, the polarization settings for both the incident and reflected light were adjusted following the same procedure outlined earlier.

The displacements of the centroids of each spot in the spotfield generated by the LG beam were measured relative to the corresponding spots in the reference spotfield. The Cartesian coordinates of these displacements were then converted to the azimuthal component of the displacement [32]. Then, the azimuthal displacement of the i th spot centroid, $\Delta\phi_i$, is divided by the focal length f_m of each microlens

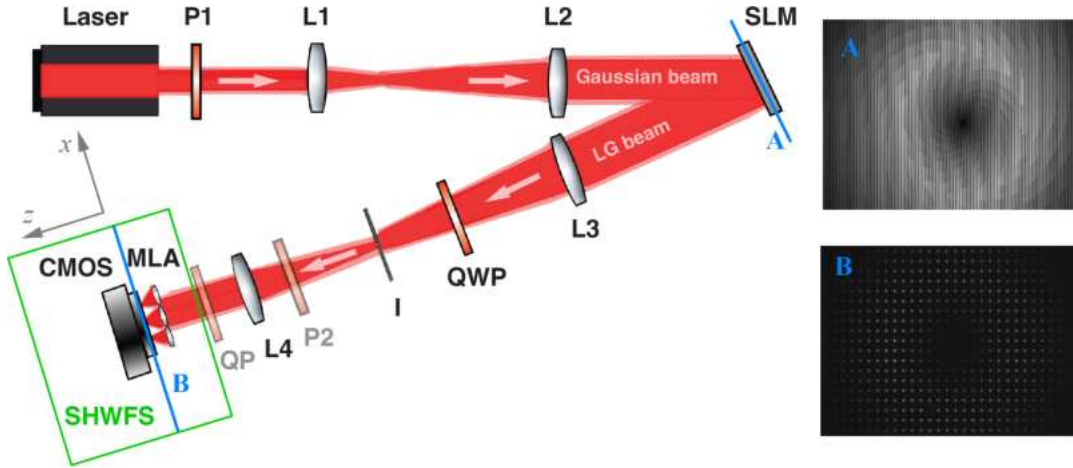


FIGURE 2.4: **Schematic of the experimental setup to measure transverse local momentum of circularly polarized LG beams.** The setup consists of polarizers P1 and P2; spatial light modulator (SLM); iris (I); quarter wave plate (QWP); Q-plate (QP); micro-lens array (MLA); lenses L1 ($f = 50$ mm), L2 ($f = 500$ mm), L3 ($f = 250$ mm), and L4 ($f = 150$ mm); and complementary metal-oxide semiconductor sensor (CMOS). The Shack-Hartmann wavefront sensor (SHWFS) consists of the MLA and the CMOS. Inset A shows a sample hologram to produce the desired LG beam with $|\ell| = 1$. Inset B shows the corresponding spotfield observed on the CMOS sensor.

and multiplied by the corresponding intensity I_i of the spot. The resulting quantity $P_{\varphi i}^{\text{exp}} = I_i \Delta \varphi_i / f_m$ provides the experimentally measured azimuthal component of the momentum density, which is in agreement with the canonical momentum (eqn. 2.10) $P_{\varphi} = I \ell / kr$ (see Fig. 2.5). To improve accuracy, multiple frames of the same spotfield were recorded, and the intensity and canonical momentum density measurements were grouped into bins corresponding to radial segments r_j . For each radial bin r_j , the average intensity $\langle I \rangle_j$ and azimuthal momentum density $\langle P_{\varphi}^{\text{exp}} \rangle_j$ were calculated over all frames.

The measurement results are displayed in Fig. 2.5. Grey symbols represent the experimentally measured intensity $\langle I \rangle_j$ as a function of radius r , and the solid grey curves depict the theoretical intensity profile $W(r)$ (Eq. 2.9), optimally fitted to the experimental data. The red and blue curves show the theoretical distributions of the azimuthal components of the canonical momentum density $P_{\varphi}(r)$ and the Poynting momentum density $\Pi_{\varphi}(r)$ from Eqs. 2.10 and 2.11, respectively. The red symbols, representing the measured azimuthal momentum densities, clearly align with the canonical momentum $P_{\varphi}(r)$ rather than the Poynting momentum $\Pi_{\varphi}(r)$. Notably, the canonical momentum is independent of the polarization helicity σ and remains sign-consistent across the beam radius. In contrast, the azimuthal Poynting momentum depends on σ and reverses its sign with radius r , following the $\sigma \ell$ symmetry.

These experimental observations corroborate theoretical predictions, specifically the argument that a Shack-Hartmann Wavefront Sensor (SHWFS) measures the weak value of the momentum operator, effectively providing the canonical momentum density [73].

Statistical errors in the measured azimuthal momentum density (red points in Fig. 2.1) range from 5×10^{-3} to 6×10^{-2} across different radii. The maximum statistical error occurs near the vortex core, where low spot intensities lead to less precise

centroid detection. For vortex beams ($\ell \neq 0$), systematic deviations from the theoretical curves are evident around $r/w_0 = 0.5$, corresponding to regions of high intensity gradients (see grey curves). These deviations may arise from cross-talk between neighboring microlenses, as discussed in the supplementary section of [32].

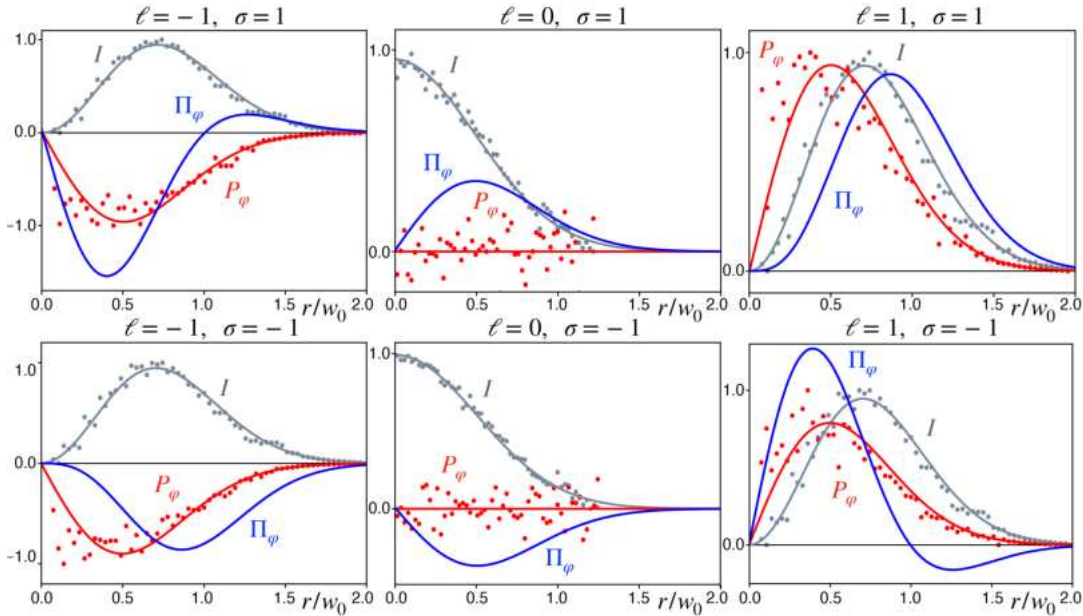


FIGURE 2.5: **Experimental study of the distinction between canonical momentum and Poynting vector.** Experimental (dots) versus theoretical (curves) results for the radial distributions of the intensity and azimuthal component of the momentum density in LG beams with $\ell = 0, \pm 1$ and circular polarization $\sigma = \pm 1$ in the $z = 0$ plane (plotted in arbitrary units). The experimental results are obtained using the Shack-Hartmann wavefront sensor, as explained in the section (2.1). The displacements in cartesian coordinates were transformed to those in polar coordinates. These are consistent with the canonical momentum density independent of circular polarization, rather than with the circular polarization-dependent Poynting vector (eqns. (2.10) and (2.11)).

Note that the change in sign of Π_ϕ when $\ell\sigma = -1$, does not signify *azimuthal backflow* as this can occur only due to the interference of at least two orbital angular momentum eigenmodes (c.f. Chapter 4).

2.3 Concluding remarks

The method of measuring transverse local momentum using a SHWFS is described. The local or canonical momentum and the Poynting vector are not one and the same for vector fields. In order to illustrate this, we have performed experimental measurements of the transverse momentum density in circularly polarized vortex LG beams via a SHWFS. This yielded polarization-independent results consistent with the canonical current rather than the Poynting vector. For the rest of the dissertation, fields with uniform linear polarization will be considered.

Contributions: In the work [67], the author has constructed the experimental setup, performed the experiment, analysed the data, performed simulations, prepared graphics, and written parts of the manuscript. Radek Łapkiewicz and the author have designed the setup. Konstantin Bliokh has conceptualised the idea of the work. Konstantin Bliokh and Aleksandr Bekshaev have performed theoretical calculations, prepared graphics, and written most of the manuscript. Bernard Gorzkowski has assisted in performing the data analysis. Anat Daniel has assisted in writing the manuscript. Konstantin Bliokh and Radek Łapkiewicz have supervised the project.

Chapter 3

Backflow in the interference of two Gaussian beams

In the present chapter we discuss the observation of anomalous transverse local momenta in the superposition of two wide Gaussian beams of unequal amplitudes. Such a superposition is prepared using a polarization based Mach-Zehnder interferometer. The measurement of local momenta is performed using the SHWFS (discussed in Chapter 2). Although the interference of two beams has been widely studied since Thomas Young's experiment in 1801, the wavefront of such a superposition, when the beams are unequal in amplitude, isn't entirely intuitive. As described below, the concept of the present work, stems from the nature of this wavefront.

3.1 Introduction to the concept

For the sake of simplicity, instead of working with Gaussian beams, let us consider the superposition of two plane waves with unequal amplitudes and equal but opposite inclinations to the z -axis.

$$\Psi(x, z) = e^{i(z+ax)} + be^{i(z-ax)}. \quad (3.1)$$

Here, $b \in [0, 1]$ is the ratio between the amplitudes of the beams and $2a$ is a measure of the angle between the propagation directions of the two plane waves— $\vec{k}_1 = (a, 1)$, $\vec{k}_2 = (-a, 1)$, x and z are the transverse and longitudinal directions respectively. All the parameters are dimensionless. The intensity distribution of this superposition is $|\Psi(x, z)|^2 = 1 + b^2 + 2b \cos(2ax)$ (see gray scale map in Fig. 1). When $b < 1$, the *wavy* nature of the wavefront— $\arg\{\Psi(x, z)\} = z + \arctan\left[\frac{1-b}{1+b} \tan(ax)\right]$ —of this superposition (see yellow curves in Fig. (3.1)) has intrigued Michael Berry and coauthors [44, 64]. This very nature of the wavefront, accounts for stronger phase gradients— $\vec{k}_s = \vec{\nabla} \arg\{\Psi(x, z)\}$ —in the dark fringes (represented by the red arrows in Fig. (3.1)). The local wave-vector of the superposition \vec{k}_s can be expressed as follows.

$$\vec{k}_s = \left(\frac{a(1-b^2)}{1+b^2+2b \cos(2ax)}, 1 \right) \quad (3.2)$$

It is clearly seen from eqn. (3.2), the x -component of the local wave-vector of the superposition vanishes when $b = 1$, i.e., for the case of equal amplitudes. It may also be noticed the x -component of \vec{k}_s is higher in magnitude than $|a|$, when the intensity of the superposition is lower. These anomalously high values of the x -component can be thought of as backflow, in the context of section 1.2.2 by considering an appropriate zero axis of the x -component of the local wave-vector. Upon understanding

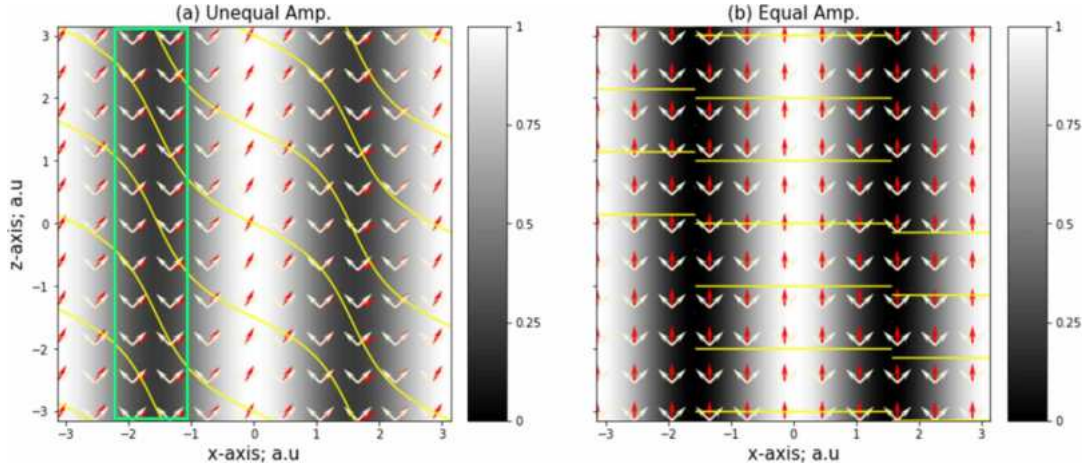


FIGURE 3.1: Visualization of Backflow in Two-Plane Wave Interference. This simulation illustrates the intensity distribution and wavefront of two interfering plane waves with unequal amplitudes propagating along the z -axis. The intensity distribution is described by $|\psi(x, z)|^2 = 1 + b^2 + 2b \cos(2ax)$, where b represents the amplitude ratio, and $2 \arctan a$ denotes the angle between the propagation directions of the two plane waves. Yellow curves correspond to the wavefronts, defined by $\arg\{\psi(x, z)\} = \text{const}$, with $a = 1$. The local wave-vector of the superposition, $\vec{k}_s = \nabla \arg\{\psi(x, z)\}$, is depicted by red arrows and is expressed as $\vec{k}_s = \left(\frac{a(1-b^2)}{1+b^2+2b \cos(2ax)}, 1 \right)$. The white arrows represent the wave-vectors of the constituent plane waves, $\vec{k}_1 = (a, 1)$ and $\vec{k}_2 = (-a, 1)$, respectively. In panel (a), where $b = 0.35$, the wavefront exhibits a wavy structure, and backflow occurs in regions of dark fringes, as indicated by the green box. In these areas, \vec{k}_s lies outside the triangle formed by \vec{k}_1 and \vec{k}_2 , signifying that the x -component of the local wave-vector exceeds that of the individual plane waves. In panel (b), with $b \rightarrow 1$, the wavefronts become flat with phase jumps (singularities) in the zero intensity lines of the fringes, and no backflow is observed since \vec{k}_s remains bounded by \vec{k}_1 and \vec{k}_2 in all regions. This visualization highlights how backflow emerges naturally from simple optical interference of unequal beams, emphasizing the wave-like nature of the phenomenon.

the above-described simple scenario, let us now consider a similar superposition but with Gaussian envelopes as plane waves are infinite in extent and cannot be produced experimentally. The Gaussian beams overlap at their waist ($z = 0$)

$$\Psi_G(x, z) = (e^{iax} + be^{-iax}) \frac{w_0}{w(z)} e^{-\frac{r^2}{w^2(z)}} e^{i\left(\frac{kr^2}{2R(z)} - \phi(z) + kz\right)}. \quad (3.3)$$

Here, $w(z) = w_0 \sqrt{1 + (z/z_R)^2}$ and $R(z) = \frac{z^2 + z_R^2}{z}$ represent the Gaussian beam waist and inverse curvature respectively. $z_R = \frac{kw_0^2}{2}$ is the Rayleigh range of the beam. $\phi(z) = \arctan\left(\frac{z}{z_R}\right)$ is the Gouy phase that appears from propagation along z . It can be shown (see supplementary section of [31]) that the x -component of the local wave-vector of $\Psi_G(x, z)$, akin to \vec{k}_s , exhibits backflow in the region of interference, i.e., in the Fresnel propagation range from the plane of interference ($z = 0$). In fact, at $z = 0$, the behaviour of the local wave-vector of the Ψ_G , is identical to \vec{k}_s .

3.2 A polarisation based common path Mach-Zehnder interferometer

Fig. (3.2) is an illustration of the experimental setup. A superposition of two unequal Gaussian beams is prepared by passing a 780 nm polarized laser beam through a half wave plate (HWP) and two identical polarizing beam displacers (PBD, ThorLabs BD40) with another HWP between them. The first HWP controls b , i.e., the amplitude ratio between the two orthogonal displaced beams generated by PBD1. The second polarising beam displacer–PBD2, together with the HWP placed prior to it, rotated by 45° in the basis of PBD1, compensates for the path difference between the beams generated by PBD1. The combination of the second HWP and PBD2 generates four beams and allows us to control the spatial separation between the chosen orthogonal beams. This transverse spatial separation between the chosen parallel beams determines their angle of intersection (related to a) at the back-focal plane A of lens L1 ($f = 150$ mm). Plane A is thus the plane of interference between

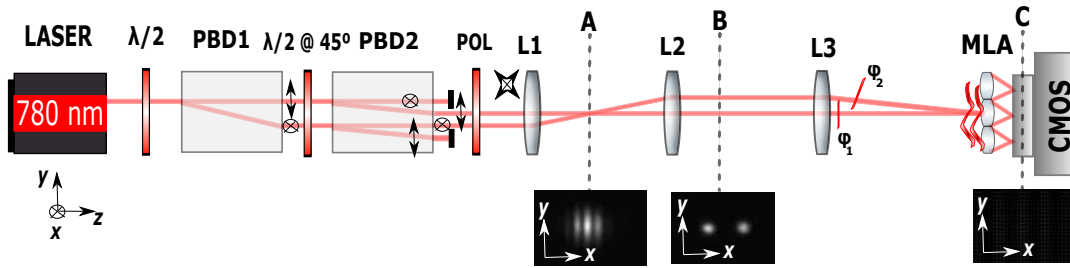


FIGURE 3.2: **Schematic representation of the experimental setup to observe backflow in the x component of the local momentum.** $\lambda/2$ –half wave plate; PBD–polarising beam displacer; POL–polariser; L–lens; MLA–microlens array; CMOS– complementary metal-oxide sensor. The superposition of two Gaussian beams of unequal amplitudes is generated at plane A using a polarization based Mach-Zehnder interferometer. The plane of interference (A) is magnified by a $4f$ imaging system consisting of L2 and L3, thus emulating a superposition of plane waves. ϕ_1 and ϕ_2 indicate the wavefronts of the individual beams. The wavefront of the superposition is analysed by a combination of MLA and CMOS, i.e., a SHWFS. A spotfield of vertical fringes on the camera sensor ensures that only the x component of the local wave-vector is of significance. Yet, in general, for tilted fringes, the predicted backflow remains unchanged. See text for further details on the setup.

the beams (See x - y cross-section of sample fringes obtained by placing the sensor at A), provided that their polarizations are made diagonal by virtue of the polarizer prior to L1. This plane is then imaged onto the microlens array (ThorLabs-MLA-150-5C-M; pitch=150 μm) using a $4f$ imaging system (L2, $f_{FT} = 35$ mm and L3, $f = 1000$ mm), with a magnification (M) of 28.6. This magnification allows us to emulate the superposition of plane waves, as the Gaussian beams impinging on the MLA have a small but finite spread in momentum. By placing sensor at the back-focal plane of L2, i.e., at plane B, the transverse momentum distribution (spectrum) of

the beams is measured (see the two spots below B). A spot-field, behind the MLA, of the x - y cross-section of the fringes, is observed at plane C on the CMOS device (mvBlueFOX-200wG). A sample of such a spot-field is shown below the sensor. The centroid of each spot in this spotfield is then compared to a reference (not shown in the figure), which is not measured directly, but calculated: corresponding to each microlens, the centroid position of the spot given by each beam is obtained by blocking the other one, and their mean position is assigned as the reference position. It is worth noting that the diffraction spread introduced by each microlens does not change the position of the centroid thereby assuring that it is determined only by the associated local momentum.

3.3 Experimental results

Let us now discuss the results obtained from the aforementioned setup and the method of analysing the data. As expected from the wavy wavefront discussed

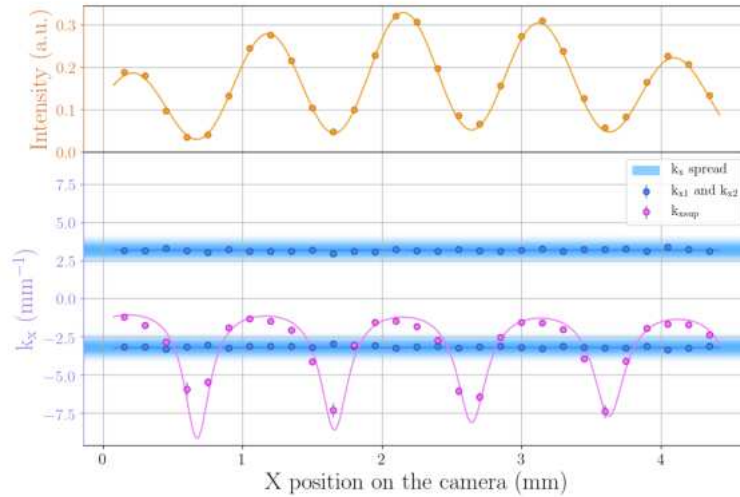


FIGURE 3.3: **Experimental observation of backflow in transverse momentum.** The orange dots are experimentally obtained values of intensity behind each microlens. The orange curve is a fit of the intensity data to a sinusoidal function with a Gaussian envelope. The blue and the magenta dots represent the experimental values of $k_{1,x}$, $k_{2,x}$ and $k_{s,x}$ (mm^{-1}) respectively, at the position of each microlens, extracted from one row of the spot field matrix (as seen from the inset below plane C in Fig. (3.2)). The error of each data point in a given x position is found by estimating the standard deviation of centroids in the corresponding column of the spot field matrix. The blue lines, $k_{1,x}$ and $k_{2,x}$ fit the data to a constant value, as expected from the behavior of Gaussian beams at their waists. Values of the parameters a (mm^{-1}) and b , extracted from the fit intensity, are used to plot the magenta curve, that represents the theoretical prediction of the superposition's local wave-vector ($k_{s,x}$). In the dark fringes, the experimental values of $k_{s,x}$, while being in good agreement with the theory, are seen to exceed not only $k_{1,x}$ (the x -component of the wave-vector of the brighter beam) but also the spread of the Fourier transform (blue shaded region). See main text for further details.

in section 3.1, the plot in Fig. (3.3) shows the oscillating local wave-vector of the superposition (magenta curve and dots). Backflow is observed in the transverse x direction, in regions where the local wave-vector of the superposition exceeds its constituent Gaussian momentum distributions, i.e. the spectrum of the first beam, (centered at $k_{1,x}$, width $\pm 3\sigma$) and of the second beam (centered at $k_{2,x}$, width $\pm 3\sigma$). This result can be associated with Fig. (3.1), where k_s lies outside the triangle formed by the mean directions of the constituent beams— k_1 and k_2 , thus leading to backflow. Here, $k_{1,x}, k_{2,x}$ (blue dots) and $k_{s,x}$ (magenta dots) are estimated by measuring centroid displacements from the reference, as discussed in Chapter (2)). The blue shaded regions centered on $k_{1,x}$ and $k_{2,x}$ represent the widths ($\pm 3\sigma$) of the individual beams' Fourier spectrum obtained by appropriately scaling the standard deviation of Gaussian intensity cross-sections recorded at the Fourier plane of L2 (see inset below plane B in Fig. (3.2)). $\sigma = \frac{2\pi\Delta L}{M\lambda f_{FT}}$, where ΔL is one standard deviation obtained from the fitting of a 2D Gaussian function to the intensity profile recorded at the Fourier plane of L2, and M is the magnification of the imaging system.

The orange dots represent experimentally obtained values of intensity at the back-focal plane of each microlens. While, the x coordinate of each dot is the centroid position of the corresponding spot from the reference spot field, its y coordinate represents the mean value of all the pixels in a given spot of the spotfield from the fringes, divided by the exposure time of the camera. The orange curve is a fit of the intensity data to $e^{-\frac{2x^2}{w_0^2}}(1 + b^2 + 2b \cos(2ax))$, where w_0 is the identical width of each Gaussian beam at $z = 0$, i.e., their waist planes. The amplitude ratio measured in the experiment— $b = 0.45$ obtained by fitting Gaussian functions to the images of the constituent beams and taking the ratio of the Gaussian amplitudes—is a constraint in the fit of the intensity of the superposition. The value of $a = 3.19 \text{ mm}^{-1}$ is extracted from the fit intensity curve. These parameters are then used to calculate and plot the theoretical prediction of $k_{s,x}$ (magenta curve).

In order to acquire further insight, we experimentally study the dependence of backflow on the amplitude ratio (b) and the angle between the two superposed beams (a). Fig. (3.4) shows the features of backflow in a given interval of x .

While the experimentally measured $k_{s,x}$ is in excellent agreement with the theoretical prediction, there are some nuances in the data and its analysis that lend the experiment some differences from the simplistic theoretical model discussed in section (3.1). We discuss these in the subsections below.

3.3.1 Explaining the difference in heights of the peaks of $k_{s,x}$

It may be observed that the heights of the peaks corresponding to backflow are slightly different across the x position (unlike the prediction from eqn. (3.2)). This is owed to a slight shift between the centers of the constituent Gaussian beams as they don't overlap perfectly on the MLA, owing to a minor misalignment of the imaging system. It is interesting to note that, despite taking this correction into account, backflow can clearly be observed.

Let us consider the superposition of two plane waves of unequal amplitudes with Gaussian envelopes with their centers shifted in equal and opposite directions along x by ζ .

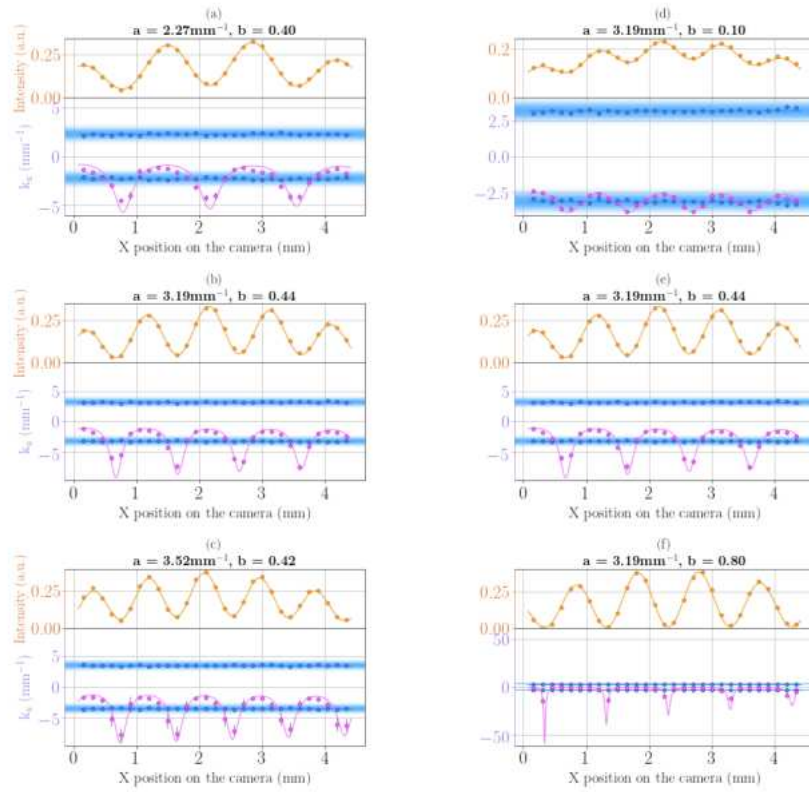


FIGURE 3.4: **The effect of the amplitude ratio and the angle between the beams on the observation of backflow.** (a)–(c) Ratio, b , is constant (up to the second digit after the decimal point) and the angle between the beams is increasing. As the angle increases, the peaks of backflow are higher and appear is more frequently. Namely, the observed backflow has a better chance to exceed the spectrum for higher angles, but simultaneously, its detection requires finer sampling (see subsection (3.3.3)) in the x direction and therefore higher spatial resolution. (d)–(f) The angle between the beams, a , is constant and the amplitude ratio is increasing. Note how the interference contrast changes. As a is the same in all the cases, backflow appears with the same frequency across the interval of x . On the other hand, the displacement due to backflow is greater as the ratio between the beams increases. When b is closer to unity (but $b \neq 1$; otherwise, we reach a singularity in the dark fringe) the x -component of the local wave-vector is more likely to exceed the spectrum (i.e. backflow) as the peaks are higher, but might not be sampled owing to the spatial resolution of the measuring device. A case where backflow is not observed is (d), where the displacements do not exceed the spectrum. In order to observe it, one can magnify further the Gaussian beams and accordingly shrink their spectra. In (f) the changing heights of the theoretically predicted peaks are due to the non-overlapping beams as mentioned in the main text. Yet, the observation of backflow is not affected. See the main text for further information.

$$\Psi_S(x, y, z) = \frac{w_0}{w(z)} e^{-\frac{y^2}{w^2(z)}} e^{i\left(\frac{ky^2}{R(z)} - \phi(z) + kz\right)} \left[e^{iax} e^{-\frac{(x+\xi)^2}{w^2(z)}} e^{i\frac{k(x+\xi)^2}{R(z)}} + b e^{-iax} e^{-\frac{(x-\xi)^2}{w^2(z)}} e^{i\frac{k(x-\xi)^2}{R(z)}} \right], \quad (3.4)$$

where, w_0 , $w(z)$, $R(z)$, and $\phi(z)$, are parameters of the Gaussian beam, defined above. Here a and x are in the units of inverse of length and length respectively. b , as usual, is unitless. When the Gaussian envelopes have a large Rayleigh range and plane of interest is $z = 0$, eqn. (3.4) can be approximately modified to the following.

$$\Psi_S(x, y, z) \approx e^{ikz} e^{-\frac{x^2+y^2+\zeta^2}{w_0^2}} \left[e^{-\frac{2x\zeta}{w_0^2}} e^{iax} + b e^{\frac{2x\zeta}{w_0^2}} e^{-iax} \right] \quad (3.5)$$

Thus, the phase and its x gradient can be expressed as follows.

$$\arg\{\Psi_S(x, y, z)\} = z + \arctan \left[\frac{1 - B(x)}{1 + B(x)} \tan(ax) \right], \quad (3.6)$$

where $B(x) = b e^{\frac{4x\zeta}{w_0^2}}$, is the position dependent ratio between the beams.

$$k_x = \frac{\partial}{\partial x} \arg\{\Psi_S(x, y, z)\} = \frac{a \left(e^{-\frac{4x\zeta}{w_0^2}} - b^2 e^{\frac{4x\zeta}{w_0^2}} - \frac{4b\zeta}{aw_0^2} \sin(2ax) \right)}{e^{-\frac{4x\zeta}{w_0^2}} + b^2 e^{\frac{4x\zeta}{w_0^2}} + 2b \cos(2ax)} \quad (3.7)$$

The factor $\frac{4b\zeta}{aw_0^2}$ appearing in the third term of the numerator in eqn. (3.7), was experimentally measured to be approximately $0.02b$, for all values of a . Therefore, the effect of the non-overlapping beams can be considered to be negligible for ratios that are not close to unity. Although, the degree of brightness changes across the camera, for ratios much less than unity, one beam is consistently brighter than the other, and hence the peaks have the same signs but are gradually smaller in heights (Figs. (3.3-3.4)). However, for b close to unity, the effect on the heights of the peaks is clearly visible, as seen in Fig. (3.4) (f). Additionally, when the ratio is closer to unity ($b = 0.98$) one beam is brighter than the other across only half of the camera and hence the signs of the peaks flip in addition to being different in heights. See Fig. (3.5).

3.3.2 Ensuring backflow beyond the tails of the Gaussian spectra of the constituent beams

The Fourier spectra of the constituent wide Gaussian beams, although narrow, are infinite in extent, and hence it is required to carefully certify backflow i.e., to ensure that the 'anomalous' local linear momentum does not arise from the infinite tail of the Fourier spectrum. In order to confirm that we observed backflow, it is required to estimate the contribution of the momentum values which lie in the tail of the Gaussian spectrum of the individual beams, and show that it is negligible compared to the 'anomalous' local momentum values arising from interference [36, 74]. For this estimation, the backflow probability P_{BF} is given by integrating the intensity over the regions of x positions within one fringe where anomalous momentum values are observed, and dividing by the intensity over one period of the fringe. The probability of finding the anomalous values within the Gaussian tails of the spectrum P_{SP} is given by integrating the spectrum over the part of its tail that can lead to such anomalous momentum values, and dividing by the integral over the full spectrum.

Let us now mathematically describe P_{BF} and P_{SP} . While obtaining a mathematical expression for the latter, we can restrict ourselves to the measured spectrum at

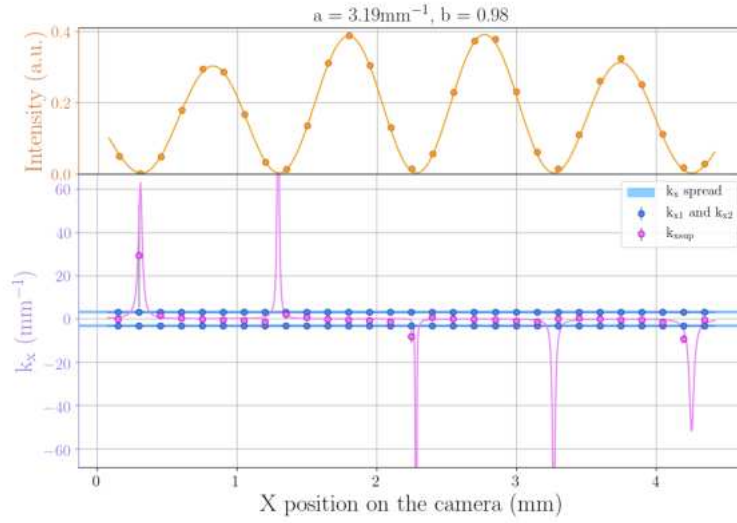


FIGURE 3.5: **The effect of non-overlapping beams.** The sign of the peaks of backflow flips when the amplitude ratio is very close to unity, and the beams don't overlap. Backflow is still observed as the x -component of the local wave-vector of the superposition exceeds the x -component of the wave-vector of the beam that is locally brighter.

plane B (Fig. (3.2)) as the probability P_{SP} remains unchanged, despite the magnification. The probability of backflow is expressed as follows.

$$P_{BF} = \frac{\int_{x_0}^{x_0+\text{fringe size}} dx dy \mathbb{1}_{k_x < k_{x,\text{ref}}}(x) I(x, y)}{\int_{x_0}^{x_0+\text{fringe size}} \int_{-\infty}^{\infty} dx dy I(x, y)}. \quad (3.8)$$

Here, x_0 is the position of an arbitrary fringe. $I(x, y)$ is the fit of the distribution of the intensity cross-section. $k_{x,\text{ref}}$ is the transverse momentum value chosen as a cut-off for the tails of the spectra. $\mathbb{1}_{k_x < k_{x,\text{ref}}}(x)$ is the identity function (equals 1 when k_x is lower than $k_{x,\text{ref}}$, 0 elsewhere).

Now, the probability of finding the anomalous values within the Gaussian tails of the spectra is given by

$$P_{SP} = \frac{\int_{-\infty}^{k_{x,\text{ref}}} \int_{-\infty}^{\infty} dk_x dk_y e^{-\frac{\lambda^2 f_{FT}^2}{4\pi^2 w_{FT}^2} \{(k_x - k_{1,x})^2 + k_y^2\}}}{\int_{-\infty}^{\infty} \int_{-\infty}^{\infty} dk_x dk_y e^{-\frac{\lambda^2 f_{FT}^2}{4\pi^2 w_{FT}^2} \{(k_x - k_{1,x})^2 + k_y^2\}}}. \quad (3.9)$$

Here, w_{FT} is the waist of the Gaussian spectrum of the brighter beam at the Fourier plane of the lens L2 of focal length f_{FT} . The beam's mean transverse momentum is $k_{1,x}$. Depending on the direction of backflow, $k_{2,x}$ may also be considered.

For the data presented in Fig. (3.3), we found P_{BF} to be larger than P_{SP} by three orders of magnitude, hence, confirming backflow. On repeating this procedure for the data presented in the subplots of Fig. (3.4), except in the case of (d), P_{BF} to be larger than P_{SP} by at least three orders of magnitude, again confirming backflow.

3.3.3 Measuring 'local momentum' with microlenses of finite size

As discussed in section (2.1.2) of the previous chapter, sampling the wavefront by the microlenses owing to their finite size leads to a deviation in the measured centroid displacement, and hence the measured transverse local momentum $k_{s,x}^D$ is different from its theoretical counterpart $k_{s,x}$, which assumes infinitely small lenses ($\lim_{D \rightarrow 0}$). Here, we provide a quantitative analysis of this discrepancy.

The wave-vector associated with the displacement of the microlens spot centroid along the x -axis, under the Fresnel approximation of the Huygens-Fresnel principle, on the pixelated sensor at the focus of the microlens array (centered on (x_c, y_c)) is given by [60, 75, 76]

$$k_{s,x}^D = \frac{\int_{y_c - \frac{D}{2}}^{y_c + \frac{D}{2}} \int_{x_c - \frac{D}{2}}^{x_c + \frac{D}{2}} dx dy \frac{\partial}{\partial x} \arg\{\Psi(x, y)\}}{\int_{y_c - \frac{D}{2}}^{y_c + \frac{D}{2}} \int_{x_c - \frac{D}{2}}^{x_c + \frac{D}{2}} dx dy I(x, y)}. \quad (3.10)$$

Here $I(x, y)$ and $\arg\{\Psi(x, y)\}$ are intensity profile and wavefront at the microlens respectively, and the integration is performed over the area of a microlens. For the simple case of superposition of two plane waves described in section (3.1), considering each microlens to be centered on a point x_c , the expression for the angular displacement in eqn. (3.10) simplifies to the following.

$$k_{s,x}^D = \frac{a(1 - b^2)}{1 + b^2 + 2b \cos(2ax_c) \frac{\sin(Da)}{Da}}. \quad (3.11)$$

Clearly, $\lim_{D \rightarrow 0} k_{s,x}^D \rightarrow k_{s,x}$, i.e., eqn. (3.11) is identical to the x component in eqn. (3.2), if the microlenses are infinitely small. In our case, $D = 150 \mu\text{m}$ and all the measured angles are also quite small. However, it cannot be assumed that the term $\frac{\sin(Da)}{Da} \approx 1$ for all values of b . The maximum $k_{s,x}$ that can be measured with the setup is dependent on the angle between the beams (a) we set. Fig. (3.6) shows the plot of $k_{s,x}$ (grey) and $k_{s,x}^D$ (magenta) for a given $a = 3.19 \text{ mm}^{-1}$ and different values of b (panels (a-f)). It is clearly visible that for b values that are close to 1, the deviation (namely the difference between $k_{s,x}$ and $k_{s,x}^D$) due to the finite size of the lens is substantial. For b close to 1 the values of $k_{s,x}$ reach to maximum, but at the same time their derivative relative to x is higher. Under such circumstances, the wavefront passing through a single microlens cannot be approximated as constant, and the measured centroid offset cannot be associated with a single wavefront slope anymore. For calculations of the maximum value of $k_{s,x}^D$ for a given value of a , see supplementary information in [31].

3.3.4 A slight deviation of the data from the theoretical plot in the bright fringes

A close observation of Fig. (3.3) and the subplots in Fig. (3.4) reveals that the magenta dots exhibit a slight deviation from the magenta curve in the region of transition between the bright and dark fringes. There are two possible factors responsible for this deviation. (1) The CMOS sensor was not placed exactly at the geometrical focus of the microlens array, which led to aberrations in the measured centroid position, particularly in the regions of higher intensity gradients [75, 76]. (2) The theoretical model doesn't consider cross-talks between microlenses, i.e., the influence

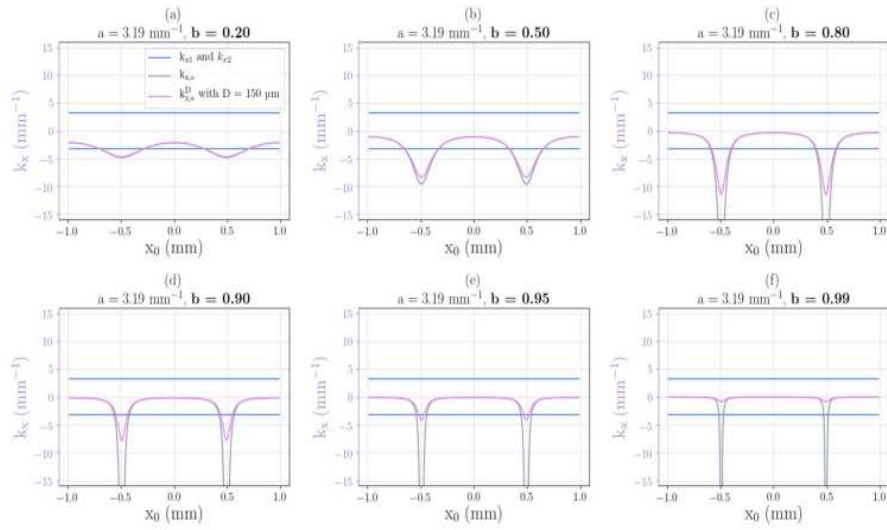


FIGURE 3.6: **The effect of finite-sized microlenses.** A comparison between $k_{s,x}$ (grey) and $k_{s,x}^D$ (magenta) for a given $a = 3.19 \text{ mm}^{-1}$ and different values of b . For values of b closer to unity (d-f), the difference between the peaks of $k_{s,x}$ and $k_{s,x}^D$ are substantial. This can also be observed in the difference between the values of magenta dots and the magenta curves near the peaks in Figs. (3.3-3.4)

of overlapping diffraction rings of adjacent lenses. These cross-talks, as we shall explore further in the following chapter, may cause the aforementioned deviation.

3.4 Concluding remarks

In summary, we demonstrate backflow by measuring the local transverse component of the wave-vector of the superposition of two wide Gaussian beams, and show that, in the dark intensity regions, it exceeds the spectrum of its constituents. The interference takes place in free space thereby excluding effects related to anisotropy or dispersion of media. We note that due to measuring the spectrum (local transverse momentum) by implementing the Fourier transform with a lens (microlens), the demonstration is confined to the paraxial approximation [40]. The diffraction spread introduced by each microlens, i.e., the size of each focal spot in the spotfield is much greater than the amount of displacement of the spot centroid. However, this uncertainty doesn't play a role here as the experiment doesn't operate in the shot noise limit.

Our study on optical waves makes use of a simple experimental configuration and can possibly be extended to various types of systems including matter waves [77, 78, 79, 80], single photons [81, 82], and mechanical waves. Apart from preparing a superposition of two wavepackets, observation of backflow requires a measurement of local momentum, which is relatively straightforward and involves only spatial filtering and detection in the far field. In the case of single photons, for example, we could repeat the experiment and expect the results to be consistent with the current ones achieved using classical beams (see Chapter (5) for further information).

Backflow thus far was considered to be exotic and difficult to observe. Here, on the contrary, we show that it would be hard not to observe backflow as it is experimentally infeasible to satisfy the criterion of equal intensity of the interfering beams. Additionally, we can control the parameters (i.e. amplitude ratio and angle) and understand their physical relevance in observing the effect. Unlike the previous study [30] which involves constraints on state preparation (for example the resolution of the SLM), we show that it is not necessary to engineer a state that manifests backflow *a priori*, as such an engineering might be difficult in particular physical systems. The two-dimensional single shot local momentum measurement using a Shack–Hartmann wavefront sensor, devoid of scanning, can be advantageous in systems manifesting backflow in any two transverse directions, for example in beams containing orbital angular momentum or any azimuthal degree of freedom (see Chapter (4) for further information). Moreover, our setup enables studying backflow for partially coherent superpositions (corresponding to mixed quantum states) as local transverse momenta of partially coherent light can be measured with a Shack–Hartmann wavefront sensor [73]. This, however, awaits further theoretical investigations.

Contributions: In the work [31], the author has constructed the experimental setup, performed the experiment, performed theoretical calculations, assisted in conceptualising the idea, in analysing the data, and in writing the manuscript. Anat Daniel has assisted in conceptualising the idea, performing the experiment, and writing the manuscript. Bernard Gorzkowski has assisted in conceptualising the idea and in analysing the data. Radek Łapkiewicz has assisted in conceptualising the idea, has designed the experimental setup, and has supervised the project.

Chapter 4

Observation of Azimuthal backflow

Light beams with azimuthal (helical) phase dependence $e^{i\ell\phi}$ were identified to be carrying orbital angular momentum (OAM) by Allen *et al.* in 1992 [83]. They were experimentally generated for the first time in 1993, by employing cylindrical lenses [84], and since then beams carrying OAM have found applications in numerous fields such as optical tweezers [85], optical microscopy [86], interactions with chiral molecules [87], etc. States of light with azimuthal phase dependence are also analogous to the eigenstates of the angular momentum operator in quantum mechanics— L_z . In the present chapter, based on [32], we examine the interference of classical light carrying only negative orbital angular momenta, and in the dark fringes of such an interference, we observe positive local orbital angular momentum. This finding has implications for the studies of light matter interactions.

4.1 Introduction

In the recent experimental observations, one-dimensional transverse local momentum of a superposition of beams was measured by scanning a slit [30] or by using the Shack–Hartmann wavefront sensor technique [31], respectively. The Shack–Hartmann wavefront sensor technique also allows for one-shot measurement of the two-dimensional transverse local momentum, as reported for the case of azimuthally phased beams in [69]. Another method, employing digital-hologram-based modal decompositions, for measuring local OAM is given in [88, 89]. In the present chapter, similar to the last chapter, we use the Shack–Hartman sensor to measure the local OAM of the superposition of two beams with helical phases, thereby moving from linear optical backflow to azimuthal backflow. In practice, we examine the superposition of two beams carrying only negative orbital angular momentum and observe, in the dark fringes of such an interference pattern, positive local OAM. This is what we term azimuthal backflow. We clarify that, by “local OAM” of a scalar field at each point, we refer to the product of the azimuthal component of the local momentum at that point and its corresponding radius.

Zacharias and Bahabad [90] have previously utilized the superposition of Bessel beams with OAM to realize transverse super-oscillatory intensity patterns. Our current demonstration of azimuthal backflow in beams carrying OAM can be interpreted as superoscillations in phase. The backflow presented here is thus a manifestation of rapid changes in phase, which could be of importance in applications that involve light–matter interactions such as in optical trapping or in enhancing chiral response of molecules [87, 91]. Apart from these, our demonstration is a step in the direction of observing quantum backflow in two dimensions, which has been theoretically found to be more robust than one-dimensional backflow [19].

4.1.1 Theoretical Model

It is often thought that beams containing vortices alone can carry OAM [92]. This is a misconception, probably arising from the familiar special beams that are eigenstates of OAM [e.g. individual Laguerre–Gauss (LG) beams and Bessel-Gauss (BG) beams]. General beams can be represented by superpositions of eigenstates, for which there is no relation between the OAM in the beam and its vortices [93]. We dispel the aforementioned misconception and use a simple model described below to create the superposition of beams carrying helical phases to demonstrate azimuthal backflow. At $z = 0$, these superpositions do not have any vortices. As we shall see later (subsection (4.1.4)), the presence of vortices in the superposition of conventional beams with helical phases such as Laguerre–Gauss (LG) and higher-order Bessel–Gauss (BG) beams can cause the measurement of azimuthal backflow to be challenging due to the sparsity of local regions in which such backflow can be observed. Fig.

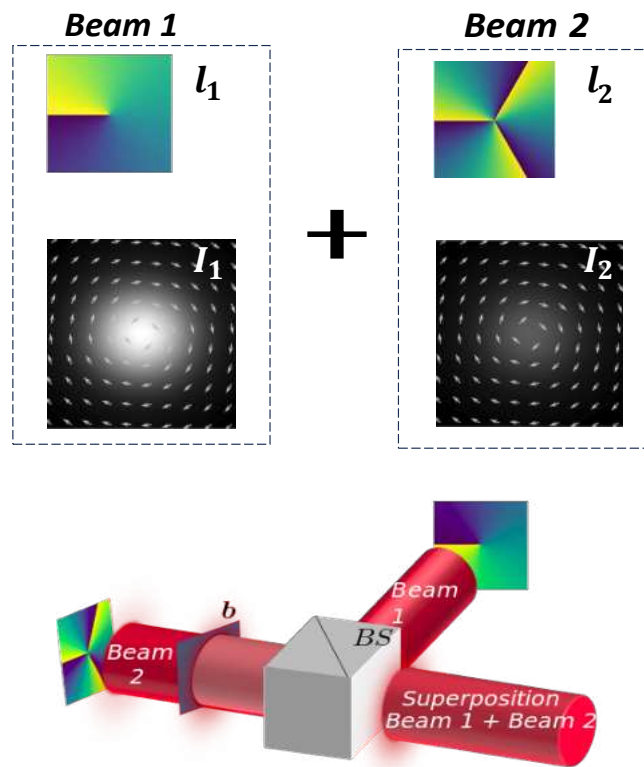


FIGURE 4.1: **Visualization of the superposition of two beams carrying helical phases.** Two Gaussian beams—beam 1 and beam 2—with intensities I_1 and I_2 , respectively, and amplitude ratio $b=0.6$ between them, each of waist $w_0=1$ mm, carrying negative helical phases $\ell_1=-1$ and $\ell_2=-3$, respectively, are superposed. The normalized azimuthal components of local wave-vectors $-k_{\phi,1,2}/|k_{\phi,1,2}|$ are indicated with gray arrows on top of the intensity pattern of each beam. A conceptual realization of such a superposition with a beam splitter (BS) is shown in the bottom panel. The $z = 0$ plane (see Fig. (4.2)) is the image plane (lenses not shown) of the phase plates indicated with blue-green colour-map.

(4.1) is a schematic of the superposition of two Gaussian beams with unequal amplitudes, carrying helical phases of orders ℓ_1 and ℓ_2 (both negative or positive) respectively. In inset (A), we provide a schematic of an interferometer setup in which

such a demonstration can be realized. Here, we provide a mathematical description of the propagation of this superposition along the z -axis. We restrict ourselves to quasi-monochromatic scalar fields under the paraxial approximation, instead of the more rigorous approach using Maxwell's equations. For $z = 0$, i.e., no propagation from the image plane of the helical phase plates at the output of the beam splitter in inset A, the scalar field is given by

$$\Psi_S(r, \phi, z = 0) = e^{-\frac{r^2}{w_0^2}} (e^{i\ell_1\phi} + be^{i\ell_2\phi}), \quad (4.1)$$

where (r, ϕ) are the polar coordinates and $|b| \in [0, 1]$ is a constant ratio between the amplitudes of the two interfering Gaussian beams, each of waist w_0 . The ϕ component of the gradient of the wavefront— $\frac{\partial}{r\partial\phi} \arg\{\Psi(r, \phi, z = 0)\}$ —can be expressed as follows.

$$k_{\phi,S} = \frac{1}{2r} \left(\ell_1 + \ell_2 + \frac{(\ell_1 - \ell_2)(1 - b^2)}{1 + b^2 + 2b \cos\{(\ell_1 - \ell_2)\phi\}} \right). \quad (4.2)$$

As seen from eq. (4.2), $k_{\phi,S}$ has the potential to point in the counterclockwise (clockwise) direction at any given radius, depending on ϕ and b , thus indicating backflow. This is represented in Fig. (4.2) for $\ell_1 = -1$ and $\ell_2 = -3$. Note that there is no backflow when the beams are equal in amplitude. In Fig. (4.2) (a), the grayscale

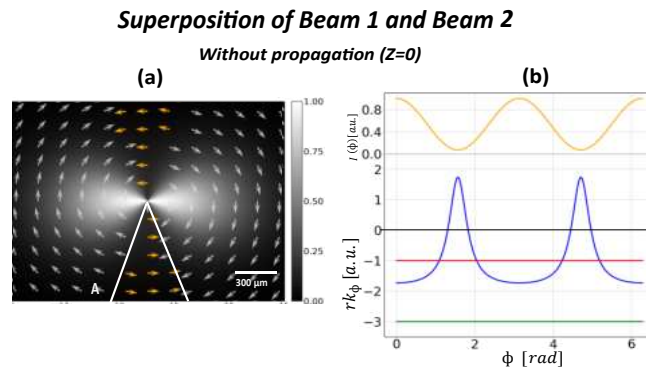


FIGURE 4.2: **Schematic representation of azimuthal backflow in the superposition of two beams carrying helical phases at the plane of superposition.** (a) Two-dimensional cross-section of the intensity distribution on the plane of the superposition without propagation (grayscale map) with $b = 0.6$ and normalized azimuthal components of local wave-vectors $-k_{\phi,S}/|k_{\phi,S}|$ (scale bar indicated at the bottom right corner). While the gray arrows, in the bright fringes, point in clockwise direction (defined by the signs of ℓ_1 and ℓ_2), the orange arrows, in the dark fringes, point in the counter-clockwise direction, thus illustrating backflow. One such region of backflow, in a given dark fringe, is marked by the white triangle labelled A. (b) The local OAM rk_ϕ for each constituent (red, green constant lines) and the superposition (blue) and the intensity (orange) at a constant radius as functions of the azimuthal angle ϕ . The values of the blue curve, indicating *positive* local OAM (above the gray line), i.e., backflow, coincide with the minima of the orange curve, i.e., the dark fringes.

map represents the intensity distribution of the field in eqn. (4.1), on top of which the normalised ϕ component of the local wave-vector— $k_{\phi,S}/|k_{\phi,S}|$ —has been marked with arrows. The arrows marked in gray in the bright fringes, point in the clockwise direction, i.e., in the directions of $k_{\phi,1}$ and $k_{\phi,2}$, while the orange arrows in the

dark fringes point in the counterclockwise direction and correspond to azimuthal backflow.

A quantitative representation of the same azimuthal backflow is shown in the plot in Fig. (4.2) (b). We plot $rk_{\phi,1}$ (red), $rk_{\phi,2}$ (green), and $rk_{\phi,S}$ (blue), which are measures of the local OAM [69] of each constituent and the superposition in eqn. (4.1), as functions of ϕ . While $rk_{\phi,1}$ and $rk_{\phi,2}$ are constant negative values as expected, the positive values of $rk_{\phi,S}$ in the dark fringes of intensity at a constant radius ($I(\phi)$; plotted in orange), are a manifestation of azimuthal backflow. Clearly, this representation is consistent with the plots in the last chapter.

4.1.2 Angular extent of the region of backflow

The angular extent of the region of backflow naturally depends on the parameters ℓ_1 , ℓ_2 and b . In fact, an optimal value of b , for chosen ℓ_1 , ℓ_2 , can maximize angular extent of azimuthal backflow.

In order to find the boundaries of the regions of azimuthal backflow, we need to set $rk_{\phi,S} = 0$. It can be observed from eqn. (4.2), that this condition leads to the following.

$$\cos((\ell_1 - \ell_2)\phi) = -\frac{\frac{1}{b} + b\frac{\ell_2}{\ell_1}}{1 + \frac{\ell_2}{\ell_1}}. \quad (4.3)$$

It is observed from equation 4.3, starting from $\phi = 0$ (bright region, no backflow), the first crossings are at $\phi = \pm \frac{1}{|\ell_1 - \ell_2|} \arccos(-\frac{\frac{1}{b} + b\frac{\ell_2}{\ell_1}}{1 + \frac{\ell_2}{\ell_1}})$. The angular extent of this bright 'no-backflow' region is:

$$\Delta\phi = \frac{2}{|\ell_1 - \ell_2|} \arccos(-\frac{\frac{1}{b} + b\frac{\ell_2}{\ell_1}}{1 + \frac{\ell_2}{\ell_1}}) \quad (4.4)$$

The angular extent of one complete fringe is $\frac{2\pi}{|\ell_1 - \ell_2|}$. For simplicity's sake we consider the proportion of the 'no-backflow' region within a fringe:

$$\Delta\tilde{\phi} = \Delta\phi \frac{|\ell_1 - \ell_2|}{2\pi} = \frac{1}{\pi} \arccos(-\frac{\frac{1}{b} + b\frac{\ell_2}{\ell_1}}{1 + \frac{\ell_2}{\ell_1}}) \quad (4.5)$$

We want a b value such that this region is minimized, we search for $\frac{\partial\Delta\tilde{\phi}}{\partial b} = 0$

$$\frac{1}{\pi} \frac{-\frac{1}{b^2} + \frac{\ell_2}{\ell_1}}{\sqrt{(1 + \frac{\ell_2}{\ell_1})^2 - (\frac{1}{b} + b\frac{\ell_2}{\ell_1})^2}} = 0 \Rightarrow b = +\sqrt{\frac{\ell_1}{\ell_2}} \quad (4.6)$$

The b value that maximizes the angular extent of the backflow region is therefore $b = \sqrt{\frac{\ell_1}{\ell_2}}$. With this value of b , we can also calculate the proportion of the fringe where backflow is observed:

$$\begin{aligned} \text{Backflow proportion} &= 1 - \Delta\tilde{\phi}|_{b=\sqrt{\frac{\ell_1}{\ell_2}}} \\ &= 1 - \frac{1}{\pi} \arccos\left(\frac{-2}{\sqrt{\frac{\ell_1}{\ell_2}} + \sqrt{\frac{\ell_2}{\ell_1}}}\right) \end{aligned} \quad (4.7)$$

The aforementioned analysis leads to the understanding that not every value of $b \in (0,1)$ can lead to azimuthal backflow (the exclusion of the lower and the upper bounds is self-explanatory). Quantitative plots of $rk_{\phi,s}$, similar to Fig. (4.2) (c) of the main text can help us visualize this. In Fig. (4.3), the top panel shows plots of the intensity cross-section of the superposition in eqn. (4.1), at a given radius $I(\phi) = 1 + b^2 + 2b \cos(\ell_1 - \ell_2)\phi$ for two different values of b . The lower panel, along with ℓ_1 and ℓ_2 , shows the corresponding plots of $rk_{\phi,s}$.

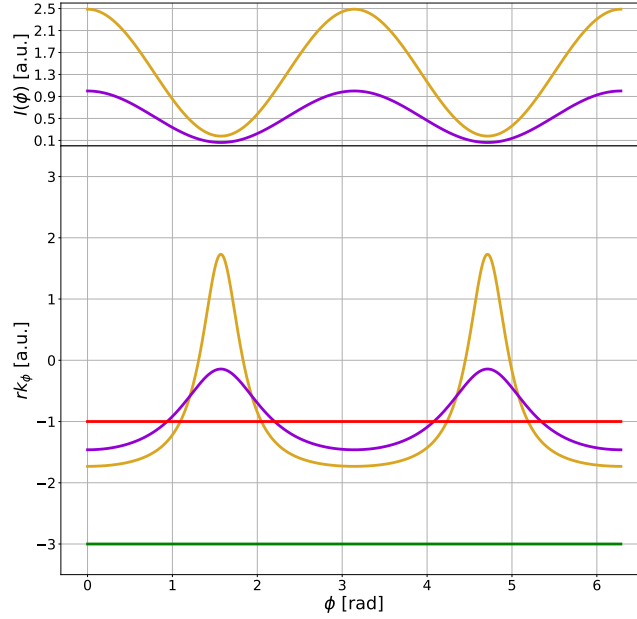


FIGURE 4.3: Here $\ell_1 = -1, \ell_2 = -3$. Top panel shows $I(\phi)$ for $b = \sqrt{\frac{\ell_1}{\ell_2}} \approx 0.6$, i.e., the optimal ratio (gold) and $b = 0.3$ (violet). The bottom panel shows $rk_{\phi,1}$ (red), $rk_{\phi,2}$ (green) and the two plots of $rk_{\phi,s}$ for the corresponding values of b from the top panel. It is evident from the violet plot that when $b = 0.3$, the angular extent of the region of backflow is 0, i.e., no backflow is observed. The local OAM of the constituent beams and the superposition are all negative.

4.1.3 Azimuthal backflow persists upon beam propagation

As seen from subsection (4.1.2), azimuthal backflow can already be observed using the field in eqn. (4.1). However, we wish to provide a complete description of the field's propagation and to theoretically study the azimuthal backflow at other planes. The field at any ($z > 0$), (i.e., after it propagates) is given by solving the Fresnel diffraction integral [40, 94], considering free propagation of the field in eqn. (4.1):

$$\Psi_S(r', \phi', z) = \frac{k}{iz} e^{ikz} e^{i\frac{kr'^2}{2z}} \left(F_{\ell_1}(kr'/z) e^{i\ell_1(\phi' - \frac{\pi}{2})} + b F_{\ell_2}(kr'/z) e^{i\ell_2(\phi' - \frac{\pi}{2})} \right), \quad (4.8)$$

where (r', ϕ') are the transverse coordinates and $F_{\ell_i}(kr'/z)$ is the ℓ_i -th order Hankel transform of the function $e^{-\frac{r^2}{w_0^2}} e^{i\frac{kr^2}{2z}}$, obtained using the ℓ_i -th order Bessel function $J_{\ell_i}(kr'r/z)$. The explicit expression of $F_{\ell_i}(kr'/z)$ can be found in tables of integral transforms [95].

Assuming, $b \in \mathbb{R}$, the azimuthal component of the local wave-vector of the superposition in eqn. (4.8) is the following.

$$k_{\phi',s} = \frac{1}{2r'} \left\{ l_1 + l_2 + \frac{(l_1 - l_2)(1 - B(r')^2)}{1 + B(r')^2 + 2B(r') \cos\{(l_1 - l_2)(\phi' - \frac{\pi}{2}) + C(r')\}} \right\}, \quad (4.9)$$

where $B(r') = b \frac{|F_{\ell_2}(kr'/z)|}{|F_{\ell_1}(kr'/z)|}$ is a position-dependent amplitude ratio and $C(r') = \arg\{F_{\ell_1}(kr'/z)\} - \arg\{F_{\ell_2}(kr'/z)\}$ is the position-dependent phase. Observe the similarities between eqn. (4.2) and eqn. (4.9). While the azimuthal components of the local wave-vectors of the constituents $k_{\phi',1} = \frac{\ell_1}{r'}$ and $k_{\phi',2} = \frac{\ell_2}{r'}$ are independent of ϕ' and have a constant clockwise (counterclockwise) for negative (positive) signs of ℓ_1 and ℓ_2 direction at any given radius, it is seen that $k_{\phi',s}$ depends on ϕ' . This is a prerequisite for observing azimuthal backflow.

We use eqns. (4.8) and (4.9) to plot the intensity distribution $|\Psi_S(r', \phi', z)|$ and the normalized local wave-vectors $k_{\phi',s}/|k_{\phi',s}|$, respectively. The two-dimensional plot is given in Fig. (4.4)(a). Comparing Fig. (4.4)(a) to Fig. 4.2 (b), we see on the grayscale map of the intensity distribution, that for $z > 0$, a vortex around $r' = 0$ is formed and no azimuthal backflow exists within this region. The value of z determines the radius of this vortex. Apart from this observation, the arrow-fields in both figures are similar. However, from the quantitative point of view, for $z > 0$, we see from eqn. (4.8) that the local OAM depends on the radius r' . In contrast to a single plot in the case of $z = 0$ [c.f. Fig. 4.2 (c)], here, for each radius there is a corresponding plot of local OAM and intensity cross-section as functions of ϕ' [c.f. Fig. (4.4)(b)].

It is worth noting that in Fig. (4.2) (b) and Fig. (4.4) (b), there's a non-zero amount of energy in the dark regions because the beams have unequal amplitudes. The intensity in these regions is relatively low but nonetheless detectable.

4.1.4 Exploring azimuthal backflow in the superposition of Laguerre-Gauss beams

Consider the LG beam $u_{\ell,p}$ in cylindrical polar coordinates (r, ϕ, z)

$$u_{\ell,p}(r, \phi, z) = \sqrt{\frac{2p!}{\pi(p + |\ell|)!}} \frac{1}{w(z)} \left(\frac{r\sqrt{2}}{w(z)} \right)^{|\ell|} L_p^{|\ell|} \left(\frac{2r^2}{w(z)^2} \right) e^{-r^2/w^2(z)} e^{i\{kz + \frac{kr^2}{2R(z)} - \psi(z) + \ell\phi\}}, \quad (4.10)$$

where $L_p^{|\ell|}$ is the associated Laguerre polynomial, $z_R = \frac{kw_0^2}{2}$, is the Rayleigh range, $w(z) = w_0 \sqrt{1 + \left(\frac{z}{z_R}\right)^2}$ is the beam waist and $\frac{1}{R(z)} = \frac{z}{z^2 + z_R^2}$ is the inverse radius of curvature. The Gouy phase is $\psi(z) = (2p + |\ell|) \arctan\left(\frac{z}{z_R}\right)$. Linear polarization is assumed.

For the sake of simplicity, we are interested in the superposition $\tilde{\Psi}(r, \phi, z = 0) = u_{\ell_1,p_1} + bu_{\ell_2,p_2}$, for $b \in [0, 1]$. In order to examine the prospect of azimuthal backflow

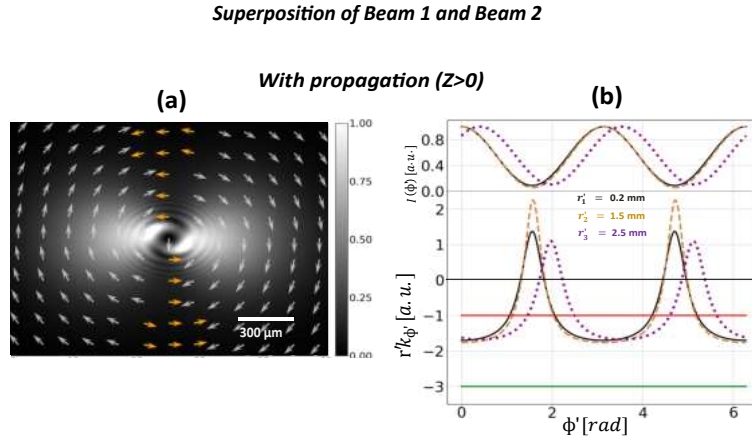


FIGURE 4.4: **Visual representation of azimuthal backflow in the superposition of two beams carrying helical phases away from the plane of superposition.** Here $b = 0.6$, and $w_0 = 1$ mm, $z = 20$ mm, and $\ell_1 = -1$ and $\ell_2 = -3$. (a) Two-dimensional cross-section of the intensity distribution (grayscale map) on a plane after propagation and normalized $k_{\phi',s}$. As in Fig. (4.2) (a), the azimuthal component of the local wave-vector exhibits backflow outside the central vortex. (b) Quantitative plots of local OAM $r'k_{\phi'}$ considering local amplitude ratio $B(r')$ and local phase $C(r')$. The red and green lines represent the constants $r'k_{\phi',1}$ and $r'k_{\phi',2}$. Three different values of r' : $r'_1 = 0.2$ mm (black solid line), $r'_2 = 1.5$ mm (brown dashed line), $r'_3 = 2.5$ mm (purple dotted line) are used to plot their respective $r'k_{\phi',s}$. The black, brown, and purple curves peak at the minima of the respective black, brown, and purple curves of the intensity cross-section in the upper panel. Again, the positive values of $r'k_{\phi',s}$ (above the gray line) are indicative of backflow, respectively.

in such a superposition, we calculate the azimuthal component of the local wave-vector $k_{\phi,s}$ (note that the radial component of the local wave-vector is non-zero).

$$\frac{1}{r} \frac{\partial}{\partial \phi} \arg \tilde{\Psi}(r, \phi) = \frac{1}{2r} \left(\ell_1 + \ell_2 + \frac{(\ell_1 - \ell_2)(1 - b(r, \ell_1, p_1, \ell_2, p_2)^2)}{1 + b(r, \ell_1, p_1, \ell_2, p_2)^2 + 2b(r, \ell_1, p_1, \ell_2, p_2) \cos\{(\ell_1 - \ell_2)\phi\}} \right), \quad (4.11)$$

where $b(r, \ell_1, p_1, \ell_2, p_2) = b \sqrt{\frac{p_2!(p_1+|\ell_1|)!}{p_1!(p_2+|\ell_2|)!}} \left(\frac{r\sqrt{2}}{w_0}\right)^{|\ell_2|-|\ell_1|} \frac{L_{p_2}^{|\ell_2|}\left(\frac{2r^2}{w_0^2}\right)}{L_{p_1}^{|\ell_1|}\left(\frac{2r^2}{w_0^2}\right)}$. Equation 4.11 is

thus similar in nature to equation 3 of the main text, owing to the term $b(r, \ell_1, p_1, \ell_2, p_2)$, which has a complex radial dependence. Thus, only specific values of the parameters involved can lead to azimuthal backflow. As seen from the examples in Figure 4.5 the regions of azimuthal backflow are restrictive and sparse. Given that in the experiment, we would use microlenses of a finite size (which adds to aberrations) to sample these regions, measuring the azimuthal backflow would be quite challenging in these cases. A similar argument holds for the superposition of higher order Bessel-Gauss (BG) beams.

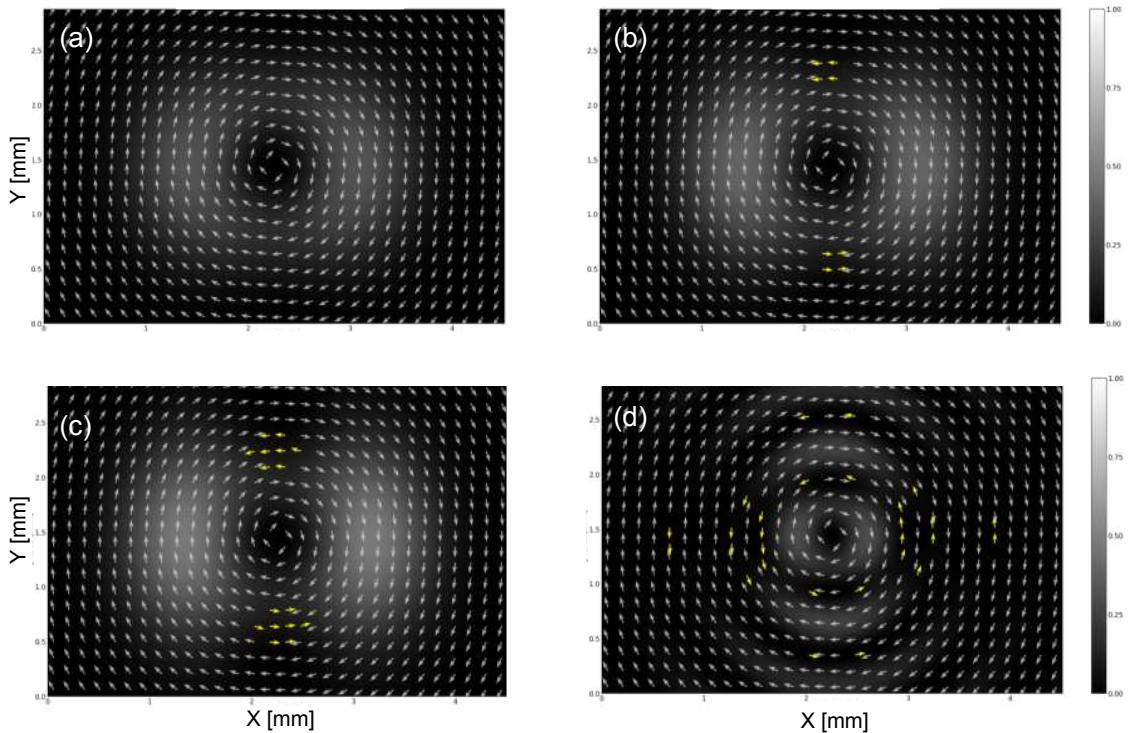


FIGURE 4.5: **Two-dimensional representation of azimuthal backflow in the superposition of LG beams.** As in Figs (4.2)(b) and (4.4)(b) of the main text, the intensity distribution is shown via grey-scale maps. Normalized $k_{\phi,s}$ are plotted with arrows. The yellow arrows correspond to azimuthal backflow. Here $\ell_1 = -1, \ell_2 = -3, w_0 = 1\text{mm}$. In (a)-(c) $p_1 = p_2 = 0$ and $b = 0.3, 0.6, 0.8$ respectively. Clearly, even if the radial index p of each constituent beam is set to 0, the complex radial dependence allows only specific regions of backflow to exist. In (d) $p_1 = 4, p_2 = 3, b = 0.8$. Non-zero radial indices lead to different distributions of the regions of backflow. Hence, azimuthal backflow in the superposition of LG beams is restrictive and localised, thus making it less applicable.

4.2 The Experiment

From subsection (4.1.3), it is thus understood that for $z > 0$, suitable radii ought to be chosen in order to observe azimuthal backflow utilizing the field in eq. (4.8). As the purpose of our experiment is to demonstrate azimuthal backflow, we limit our experimental demonstration to the field in eq. (4.1), i.e., at $z = 0$, wherein the local wave-vector has only an azimuthal component and this component in turn has no radial dependence.

A schematic representation of the experimental setup can be found in Fig. (4.6). The field in eq. (4.1) is realized by using phase masks on a phase-only spatial light modulator (Holoeye Pluto 2.0 SLM), as shown in inset A of Fig. (4.6). A 780 nm continuous wave laser (Thorlabs CLD1015) is reflected off the SLM. Since we use a phase-only SLM to simultaneously modulate phase and amplitude, we adopt the technique discussed in [71], so that the desired field is generated after filtering the first diffraction order. The SLM is imaged using lenses L_3 and L_4 onto the microlens array (ThorLabs-MLA-150-5C-M) that focuses the beam onto the CMOS

camera (mvBlueFOX-200wG). By definition, the image plane of the SLM refers to the $z = 0$ plane, as mentioned in the previous section. Inset B shows the spotfield generated on the CMOS when the mask in inset A is displayed on the SLM. Additionally, following the Shack–Hartmann sensor principle [57], a reference spotfield is generated by illuminating the microlens array with a wide Gaussian beam.

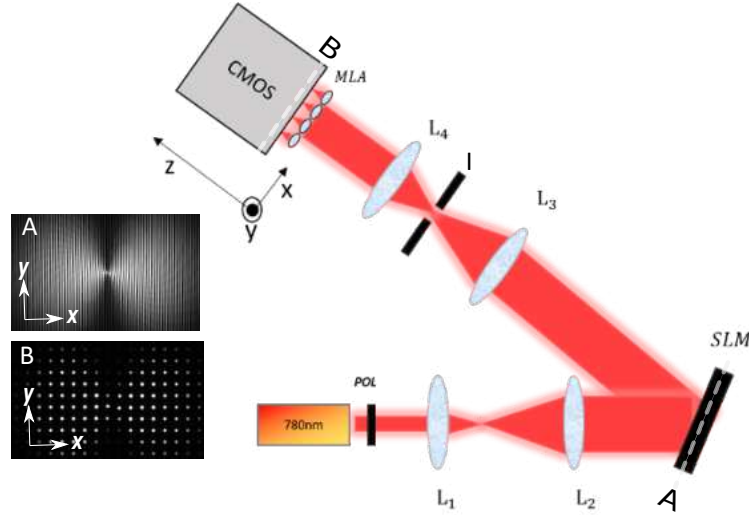


FIGURE 4.6: **Schematic of the experimental setup to observe azimuthal backflow.** POL, polarizer; SLM, spatial light modulator; MLA, micro-lens array; I, iris to spatially filter the first order of diffraction; L_1 , L_2 , L_3 , and L_4 are lenses. The laser beam is polarized and expanded by a factor of eight by lenses L_1 ($f = 50$ mm) and L_2 ($f = 400$ mm) to cover the spatial extent of the SLM. Inset A shows a sample hologram to produce the desired superposition field in eq. (4.1) with $\ell_1 = -1, \ell_2 = -3, b = 0.6$. This hologram is encoded on the plane of the SLM using the method described in [71]. The first diffraction order of the beam reflected from the SLM is spatially filtered by an iris (I) in the Fourier plane of the lens L_3 ($f = 250$ mm). The filtered beam is Fourier transformed once again by the lens L_4 ($f = 125$ mm) onto the microlens array (ThorLabs-MLA-150-5C-M), which is placed at the image plane of the SLM ($z = 0$). The micro lens array (each lens has a pitch of $150 \mu\text{m}$ and a focal length of 5.6 mm) focuses the light onto the CMOS camera (mvBlueFOX-200wG; pixel size $6 \mu\text{m}$). Inset B shows the corresponding spotfield observed on the CMOS sensor.

4.2.1 Experimental Results

The displacement of the centroids of the spotfield generated by the superposition (inset B of Fig. (4.6)) field w.r.t. that of the reference are measured in the x and y directions. These are combined to find the directions of the local wave-vectors of the superposition, as plotted in Fig. (4.7) (a) on top of each spot in the spotfield in inset B of Fig. (4.6). In agreement with the theoretical two-dimensional illustrations in Figs. (4.2)(a) and (4.4)(a), the yellow arrows here in the dark fringes correspond to the regions of backflow. Due to imperfections in the imaging and the finite sizes of the microlenses used to sample the wave-vectors, the yellow arrows in the regions between the dark and bright fringes have radial components (and are not purely azimuthal). Hence, in order to quantitatively analyze the azimuthal backflow, we generate one-dimensional plots of the local OAM [c.f. Fig. (4.2)(b)] in Fig. ().

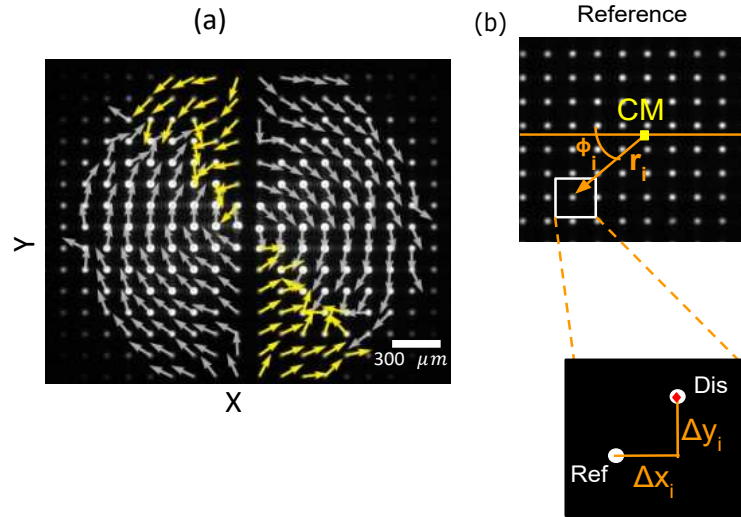


FIGURE 4.7: **Observation of azimuthal backflow—result and method.** (a) On every spot in inset B of Fig. (4.6), an arrow corresponding to the normalized direction of the total local wave-vector $\vec{k}/|\vec{k}|$ is displayed. The arrows are generated by combining the x and y displacements of the centroids of the spotfield in inset B relative to the reference (see inset of (b)). Due to imperfections in imaging and the finite size of the microlenses, the arrows contain both radial and azimuthal components. While the gray arrows point in the clockwise direction in accordance with the negative values of ℓ_1 and ℓ_2 , the yellow arrows, predominantly pointing in the counter-clockwise direction, indicate local regions in which backflow occurs. (b) illustrates the method used to extract the local OAM. The center of mass (CM) of the reference spotfield is marked in yellow. Then polar coordinates of the i th spot (r_i, ϕ_i) are found. For the i th spot in the reference (Ref), there is a corresponding displaced (Dis) spot (in spotfield of the constituent beams or the superposition) marked in red. $\Delta\phi_i$ is found by converting the displacements in cartesian coordinates Δx_i and Δy_i to displacements in polar coordinates. The local OAM is then given by $r_i \frac{2\pi}{\lambda f_m} \Delta\phi_i = r_i k_{\phi_i}$, f_m is the focal length of each microlens.

The data points of the plots given in Fig. 3 are generated as follows. In the spotfields of the constituent beams or the superposition, the i -th spot's centroid on the reference spotfield is displaced by Δx_i and Δy_i in the x and y directions, respectively. The displacements in the cartesian coordinates are transformed to displacements in the polar coordinates (r_i, ϕ_i). r_i is found by calculating the distance between the spotfield's global center of mass and the individual spot's centroid. ϕ_i is given by the angle between the horizontal axis and the line joining the center of mass and the individual spot's centroid. See the illustration in Fig. (4.7)(b) for a schematic representation. Following this, Δx_i and Δy_i are combined to find the angular displacement of the spot $\Delta\phi_i = -\sin\phi_i\Delta x_i + \cos\phi_i\Delta y_i$. To obtain the azimuthal component of the local wave-vector for the i -th displaced spot, the angular displacement is scaled using the focal length f_m of each microlens— $k_{\phi_i} = \frac{2\pi}{\lambda f_m} \Delta\phi_i$. The local OAM is then given by $r_i k_{\phi_i}$.

The experimentally measured local OAM is plotted in Fig. (4.8) for each constituent beam (red and green scatter plots) and the superposition (blue scatter plot). The solid red, green, and blue are the corresponding theoretical predictions, and we find the experimental data to be in good agreement with the theory. Here, the

constituent beams carry negative angular momenta; hence, all blue data points that correspond to positive values (above the black line) are indicative of azimuthal backflow.

The periodicity of the local OAM of the superposition depends on $|\ell_1 - \ell_2| = \Delta\ell$. For higher $\Delta\ell=3$ [Fig. (4.8)(B)], the number of peaks increases and the peaks are taller relative to the peaks in Fig. (4.8)(A) (for which $\Delta\ell=2$). Once $\Delta\ell$ is increased further, although the value of backflow increases substantially, its detection requires finer sampling, i.e., microlenses of smaller size [60, 75].

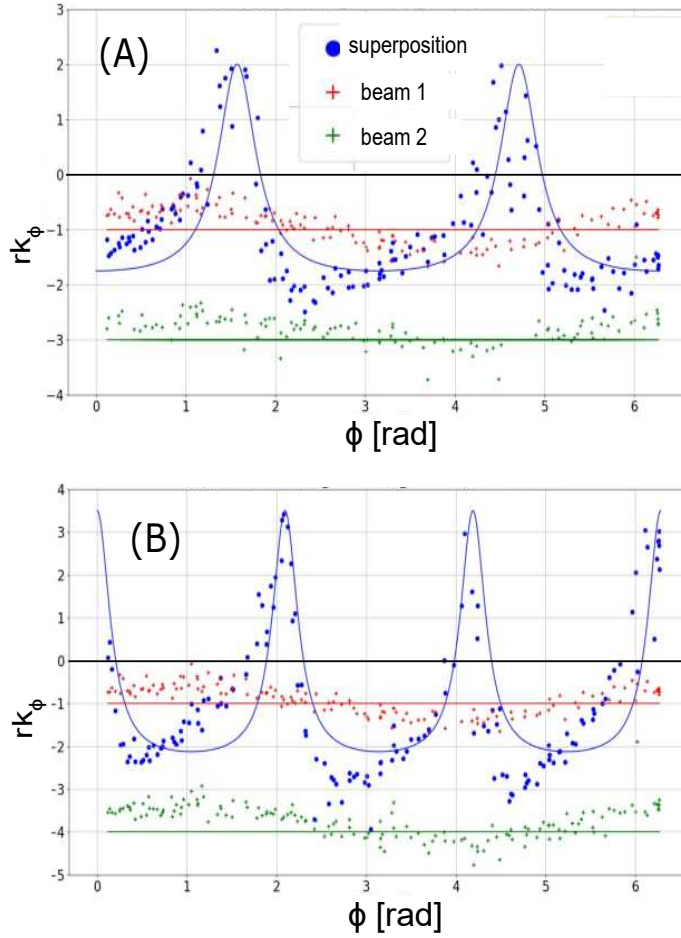


FIGURE 4.8: **Experimental observation of azimuthal backflow.** In (A) and (B), the scatter plots are data points and the solid curves are theoretical predictions. The y -axes representing local OAM are dimensionless and x -axes, representing azimuthal angle ϕ , are in radians. The red, green, and blue scatter plots of $rk_{\phi,1}$ (beam 1), $rk_{\phi,2}$ (beam 2), and $rk_{\phi,S}$ (superposition), respectively, are in good agreement with their corresponding theoretical predictions. In these examples, the constituent beams carry negative angular momenta; hence, all blue data points that are positive correspond to azimuthal backflow. In (A) and (B), the ratio $|b| = 0.6$ is the same, while $\Delta\ell = 2$ ($\ell_1=-1, \ell_2=-3$) and $\Delta\ell = 3$ ($\ell_1=-1, \ell_2=-4$), respectively. Note that in both (A) and (B), the minima of the blue scatter plot show slight deviations from the theoretical prediction. This is a systematic error owing to cross-talks between microlenses (further explored in the following subsection). The statistical error in $rk_{\phi,S}$ ranges from ± 0.02 to ± 1.3 . Yet, the observation of azimuthal backflow is unaffected by these errors.

4.2.2 Error Analysis

An estimation of statistical error in the quantitative measurement results presented in Fig. (4.8) (A) and (B) of the main text has been performed by repeating the experiment 20 times. In each of the 20 runs of the experiment, images of spotfields of the constituent beams and their superposition are saved. The local OAM $r_i k_{\phi_i}$ corresponding to each spot in the aforementioned images is obtained by the method explained above. In order to find the statistical error in our measurement of the local OAM of the superposition, the azimuthal angles ϕ_i are grouped into small sectors consisting of data from at most two microlenses. Then the corresponding $r_i k_{\phi_i}$ from every run of the experiment are stacked together. The mean local OAM $\langle r k_{\phi} \rangle$, corresponding to each such stack is found. The standard deviation of the mean local OAM from the sectors of angles are plotted in Fig. (4.9). The greenish-blue data points and their associated error bars in subplots (A) and (B) are reflective of the statistical error in measuring the local OAM of the superposition for the data presented in Fig. (4.8) (A) and (B) respectively.

As explored in the previous chapter, a possible cause of minor but systematic deviation of the local OAM of the superposition, i.e., the data points in Fig. (4.8) (A) and (B) from the associated theoretical plots, is the presence of cross-talks between the microlenses. A visualization of the cross talk is given in Fig. (4.10). Fig. (4.10a) is an experimentally obtained spot-field, one can observe bright diffraction rings surrounding each spot. (4.10b) is a simulated spot field based on the parameters of the experiment. The microlenses are assumed to be independent in this simulation for avoiding cross-talks (diffraction rings of neighbouring microlenses do not contribute either coherently or incoherently). Fig. (4.10c) is a simulated spot field based on the parameters of the experiment but here, the microlenses are no longer assumed to be independent. Namely, the diffraction rings of the microlenses are made to interfere with its neighbors. In experimental data, these cross-talks cause the detected centroids in the transition of regions of bright intensity to dark intensity to be shifted.

4.3 Concluding remarks

In this chapter, we have studied the phenomenon of azimuthal backflow both theoretically and experimentally, by utilizing the superposition of two beams carrying helical phases and having unequal amplitudes. We show explicitly that for two beams carrying negative OAM, the local OAM of their superposition is positive in certain spatial regions. As the angular spectra of the constituent beams are discrete, the backflow is directly certified from the measurement. This is advantageous compared to previous demonstrations [30, 31], where the Fourier spectra of the constituent beams are infinite, and hence it is required to carefully certify backflow i.e., to ensure that the local linear momentum does not arise from the infinite tail of the Fourier spectrum [74]. This is because beams carrying well-defined OAM can be experimentally generated, unlike plane waves.

It is worth reiterating that the azimuthal backflow in superpositions of LG/BG beams is hard to observe due to complex radial dependence (c.f. subsection (4.1.4)). For the beams that we propose, even if the azimuthal component of the local wave-vector has a radial dependence (i.e., for $z > 0$), the azimuthal backflow can be observed and is relatively robust.

Note that in our study, we use a scalar field description where the polarization of light is not of consequence. However, the research can be extended to vector fields

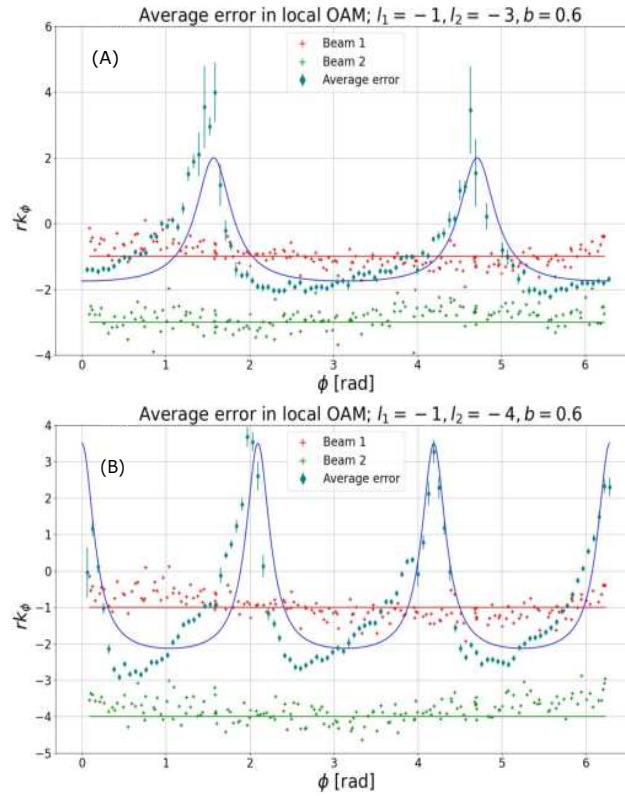


FIGURE 4.9: **Statistical error in measuring local OAM of the superposition.** The greenish-blue data points, represent the average local OAM of the superposition in the corresponding sector of the the stacked spotfields, as described in the text. The standard deviation of this mean value is plotted as an associated error bar in greenish-blue. Subplots (A) and (B) are obtained by repeating the measurement 20 times for the parameters in Fig. (4.8) (A) and (B) of the main text respectively. The statistical error is significantly higher in the dark fringes (c.f. Figure (4.2) (B) of the main text), as is evident from either subplot. This is owed to the inherent error detecting spot centroids in low intensity regions. Moreover, in (A), the statistical errors in the dark fringes are higher than those in (B). As the angular extent of a dark fringe in (A) is higher than those in (B), in the former case, more imperfections in the wavefront are sampled with higher resolution by the microlenses in the dark fringes. While generating (A), two anomalous data points (due to dust on specific microlenses), have been excluded from every run of the experiment.

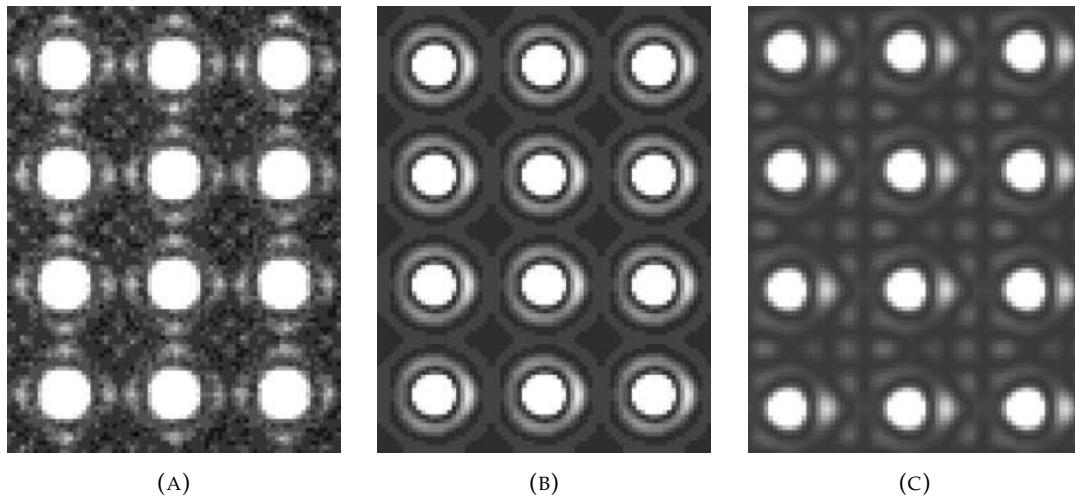


FIGURE 4.10: **Examining cross-talks in spotfields—a possible cause of systematic errors.** The contrast and the brightness in all the spotfields have been adjusted to make the cross-talks visible. (A) Spotfield obtained from the experiment. (B) Simulated spotfield assuming independent microlenses (diffraction rings of neighbouring microlenses do not contribute either coherently or incoherently). (C) Simulated spotfield where diffraction rings from neighbouring spots interfere. Note that (A) and (C) are similar and this interference effect causes the centroid positions to deviate slightly from theoretical predictions.

[96, 97, 63] as well. Particularly, in various recent theoretical works [98, 99, 100, 101, 102] energy backflow has been predicted in vector fields.

As explained in this chapter, azimuthal backflow is a consequence of strong phase gradients of fields over small spatial extents. Such gradients can affect the interactions of fields with atoms and molecules. For example, high phase gradients present in the superpositions we generate can be used to excite higher order multipole transitions in atoms. Such higher order transitions are possible, specifically, in cold atoms with wave-functions that sample a large region in space [103]. These transitions are relevant in designing ultra-precise atomic clocks [34, 35] or in generating atom probes for photons in low-light intensity regions [104]. A study of the interplay between the size of the wave-function of an atom placed in a superposition of negative angular momentum states of light and the region of backflow (positive local OAM) in such states would be interesting. The electric field pattern investigated by us can also be employed in manipulating small particles in optical tweezers [105] or even to enhance chiral light–matter interactions [87, 91].

Contributions: In the work [32], the author has designed and constructed the experimental setup, performed the experiment, analysed the data, performed theoretical calculations, performed simulations, and written the manuscript. Anat Daniel has assisted in writing the manuscript. Bernard Gorzkowski has assisted in performing the experiment and analysing the data. Radek Łapkiewicz has conceptualised the idea and supervised the project.

Chapter 5

Optical backflow in the single photon regime

5.1 Introduction

In this chapter, we extend our observations in Chapters 3 and 4 to the single photon regime. We utilize the interference of a single photon wave-function with itself [106] to observe the presence of anomalous transverse local momenta. Upon considering transverse properties of single photon wave-functions, the theoretical description of anomalous transverse local momenta can be shown to be equivalent to the classical case described in Chapters 3 and 4. Hence, the theoretical description is not repeated here. The primary difference between the experiments with classical light (previously described) and the single photon experiment (to be discussed here) is in the preparation of a heralded single photon source via spontaneous parametric down-conversion (SPDC). Under ideal circumstances, in the presence of photon-number-resolving detectors, the detection of a photon in the idler arm guarantees the detection of another photon in the signal arm.

Superoscillatory hotspots in intensity have been previously observed with single photons [82]. However, to the best of our knowledge, anomalous transverse local momenta or backflow haven't yet been observed with quantum particles and particularly in the single photon regime. Our results are a step in this direction.

The primary challenge in observing the anomalous transverse local momenta in dark fringes of the superposition of two beams in the single photon regime is the presence of Poisson noise and dark counts. This is explored in numerical simulations. Additionally, as a first step, the experimental conditions are simulated with an attenuated laser replacing the signal arm of a heralded single photon source prepared via a SPDC process by precisely gating (with the idler photons) an image intensifier that is a part of an intensified scientific CMOS device assembly.

5.1.1 Simulations with Poisson noise

The primary difference between the experiments presented in Chapters 3 and 4 and the one presented here is the presence of Poisson noise. Poisson noise, often referred to as *shot noise*, originates from the particle-like nature of light and is caused by fluctuations in photon numbers due to variations in their arrival times at the detector [107]. The number of photons detected by a sensor within a given time interval follows a discrete Poisson probability distribution, where a mean of N photons results

in an uncertainty of \sqrt{N} photons. Additionally, Gaussian noise or *thermal noise* originates from the random motion of charge carriers in the sensor material due to thermal energy, even in the absence of incident photons. Thermal noise is independent of the signal and manifests as random fluctuations in pixel values, following a Gaussian distribution with zero mean (non-zero mean in the presence of a background) [108]. A code to generate images with Poisson noise and thermal noise (based on a Gaussian distribution) can be found in this [Github](#) link. The current version of the code was written by Bernard Gorzkowski. Fig. (5.1) depicts some simulated spotfields and associated local wave-vectors. Fig. (5.2) is a plot generated by simulating

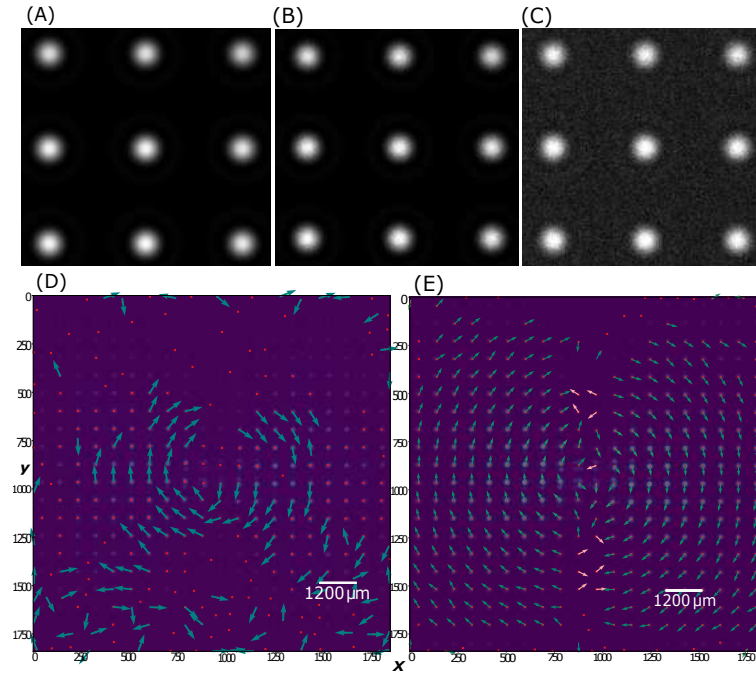


FIGURE 5.1: **Simulated Spotfield Images with Added Noise.** (A) Reference spotfield image derived by convolving an input Gaussian field with the Airy disc of a microlens, producing intensity values from 0 to 255. (B) Poisson noise is applied to the image in (A) by randomizing each pixel's value according to a Poisson distribution with the original pixel intensity as the mean, preserving the total detected photon counts. (C) Gaussian noise is superimposed on the Poisson-noised image, simulating experimental conditions. This sequence replicates noise characteristics observed in real spotfield measurements. (D) A spotfield generated from an input field of the form $\Psi(r, \phi) = e^{-r^2/w_0^2} \{e^{i\ell_1\phi} + be^{i\ell_2\phi}\}$, with $w_0 = 3.8 \mu\text{m}$, $\ell_1 = -3$, $\ell_2 = -5$, and $b = 0.8$. This configuration replicates experimental conditions, with Poisson noise (0.7 million detected counts) and negligible Gaussian noise. Green arrows represent normalized local wave-vectors proportional to displacements of the detected spot centroids (red crosses) relative to a reference Gaussian spotfield. No azimuthal backflow is visible since dark fringe centroids are undetected, and some centroids are misidentified. (E) Same as (D) but with 7 million total counts, leading to observable azimuthal backflow, indicated by counterclockwise pink arrows. This setting is ideal and as we shall see below, cannot be achieved in the current experimental setup. Note that spots close to center in the spotfields in (E) and (D) are not Gaussian owing to fast changes in phase.

spotfields with Poisson noise after fixing the total number of counts (i.e., detected

photons) over all the pixels. The mean and standard deviation of Gaussian noise, while generating the spotfields, are set to zero. The results are qualitatively similar to Fig. (4.8).

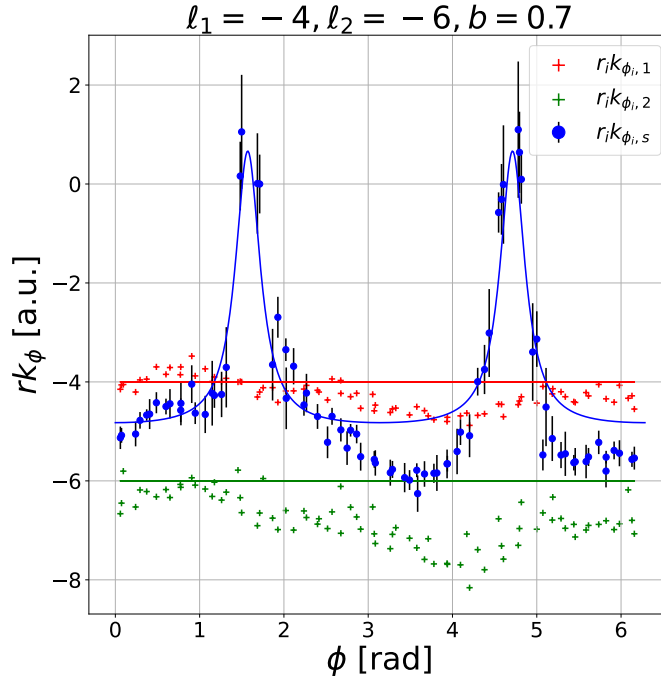


FIGURE 5.2: **Simulated Local OAM with Poisson Noise.** This plot closely resembles Fig. (4.8) generated from experimental data. Spotfields were generated using input fields defined as $\Psi_1(r, \phi) = e^{-r^2/w_0^2} e^{i\ell_1\phi}$, $\Psi_2(r, \phi) = e^{-r^2/w_0^2} e^{i\ell_2\phi}$, and $\Psi(r, \phi) = \Psi_1(r, \phi) + b\Psi_2(r, \phi)$, where $w_0 = 3.9 \mu\text{m}$, $\ell_1 = -4$, $\ell_2 = -6$, and $b = 0.7$. A Gaussian reference spotfield was also simulated. Poisson noise was applied to each spotfield, with the total photon count set to 7 million, as described in Fig. (5.1). Red, green, and blue symbols represent the local $r_k\phi_i$ values extracted from the centroid detection of spotfields corresponding to $\Psi_1(r, \phi)$, $\Psi_2(r, \phi)$, and $\Psi(r, \phi)$, respectively. Solid lines denote the theoretical local OAM for each field. The simulated data deviates from theoretical predictions due to systematic errors in the centroid detection process. Error bars on blue points correspond to $\pm 6\sigma/\sqrt{N_i}$, where σ is the standard deviation from Gaussian fits to each spot, and N_i is the photon count per spot. This is based on a total count of 7 million photons, which, experimentally, corresponds to 400 photons/second over 5 hours (assuming no dark counts). The simulation illustrates that with minimal dark counts, the chosen photon rate can reveal azimuthal backflow, despite momentum uncertainty associates with spot size (refer to section 2.1).

5.2 The experiment

The experiment consists of several components, which are outlined below. These include the preparation of a single-photon source, heralding the detection of one

photon by detecting its counterpart using an intensified camera, and constructing the setup to observe azimuthal backflow with single photons.

5.2.1 A source of single photons generated by SPDC

Firstly, the experiment involves preparing a source of single photons using co-linear, Type-II spontaneous parametric down conversion (SPDC). As depicted in Fig. (5.3), a periodically poled potassium titanyl phosphate (PPKTP) crystal, with a poling period of 10 μm and dimensions $1 \times 2 \times 5 \text{ mm}^3$, is pumped by a 405 nm continuous wave laser at 113.00 mW output power. A lens (L1) of focal length 150 mm focuses the appropriately polarised (using the half wave plate $\lambda/2$) pump beam onto the crystal, whose temperature is set at 24.03° Celsius, via a Peltier-based crystal oven operated by an external temperature controller (TC). After the crystal, the pump is filtered using a long-pass filter (F1), and orthogonally polarised bi-photons generated via SPDC, are separated into two arms (signal, idler) by a polarising beam splitter (PBS). Narrowband filters (F2) in either arm, centered on 810 nm, having a 3 nm full width half maximum (FWHM) each, are used to select degenerate single photons. The coincidences between the signal and idler arms are optimised by coupling the single photons to single mode fibers (SMFs), which are, in turn, directed to avalanche photo-diodes (APDs). The transistor-transistor logic (TTL) signals from these APDs are sent to a Field Programmable Gate Array (FPGA), which is connected to a computer. The FPGA is programmed in LabVIEW (code written by Jerzy Szuniewicz) to analyze the number of counts in each channel, as well as to detect coincidences—events where the two photons arrive within 10 ns of each other. Beam-walking techniques (with mirrors not shown in the schematic representation) are employed to optimise the coupling into the SMFs and thereby to optimise the coincidences by observing the LabVIEW interface.

5.2.2 Heralding one photon via the detection of its counterpart using an intensified camera

The second part of the experiment involves building the set-up shown in Fig. (5.5) to observe optical backflow with heralded single photons. The idler photon from the pair produced by the SPDC process described above, is registered by an APD, which, in turn, generates a short TTL pulse. This pulse is used to trigger our custom-built intensified scientific CMOS (sCMOS) camera [109] using a gating module (Photek GM300-3N) with a mean trigger rate of 150 kHz to herald the other photon from the pair and thereby create a heralded signal. DG in the figure stands for a delay generator (Stanford Delay Generator DG645) and is used to manipulate the original TTL pulse from the APD and control to set an electronic delay of 10 ns, a gap of 3.3 μs between consecutive pulses, and an effective opening time of the gating module to 40 ns. The signal photon is then transmitted through a 45 m long spool of a single mode fiber (SMF) to synchronize the gating time of the image intensifier and the arrival of the signal photon by compensating for the processing time of the image intensifier (II in Fig. (5.5)) and the DG. A relay lens (RL) is used to image the photon flashes on the phosphor screen of the image intensifier to the sCMOS. The image intensifier consists of a photo-cathode that generates a photoelectron from the incident photon, followed by a micro-channel plate (MCP) that amplifies the photoelectron into a burst of electrons, and lastly a scintillator, commonly referred to as a phosphor screen, on which the burst of electrons strikes to generate a flash of photons [110]; while the diameter of each microchannel is 6 μm , the pixel size of the sCMOS sensor

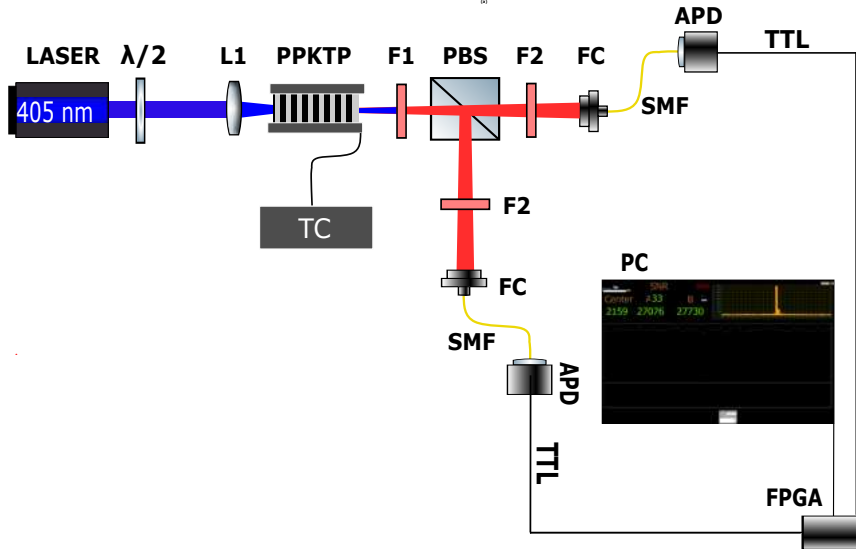


FIGURE 5.3: **Experimental setup to generate single photons via SPDC and to optimise coincidences between the signal and idler arms.** A 405 nm continuous wave laser pumps a PPKTP crystal (10 μm poling period, $1 \times 2 \times 5 \text{ mm}^3$ dimensions) at 113 mW, focused by lens L1 (150 mm focal length). The crystal temperature is maintained at 24.03°C by a Peltier oven (TC). After filtering out the pump (F1), orthogonally polarized bi-photons are split by a polarizing beam splitter (PBS) into signal and idler arms. Degenerate photons (810 nm, 3 nm FWHM) are selected by filters (F2), coupled into single-mode fibers (SMFs), and detected by avalanche photodiodes (APDs). Coincidence detection occurs through TTL signals processed by an FPGA interfaced with a PC. The rate of coincidence counts is 30 kHz and the rate of single counts is 250 kHz.

is $6.5 \mu\text{m}$. See Fig. (5.4) for a schematic representation of the intensified camera and the image intensifier. The purpose of this setup is to achieve an accurate temporal correlation between the camera's operation and the arrival of the signal photon from the experimental setup.

5.2.3 Setup to observe azimuthal backflow with heralded single photons

The experimental setup to generate a superposition of two beams and observe backflow in the local momentum is very similar to that described in Chapter 4 section 4.2. As shown in Fig. (5.5) the signal photons, after passing through the long spool of SMF, pass through a quarter wave plate ($\lambda/4$) and a half wave plate ($\lambda/2$) to ensure linear polarization. The polariser (POL) tunes the linear polarization to ensure that the first order diffraction pattern from the SLM has the maximum intensity. As discussed in earlier chapters, the plane of the SLM is imaged onto the microlens array (MLA; parameters same as those in previous chapters). The back-focal plane of the MLA (labelled as A in Fig. (5.5)) is imaged onto the photo-cathode of the image intensifier (labelled as B in Fig. (5.5)) with two achromatic doublets (L5 and L6).

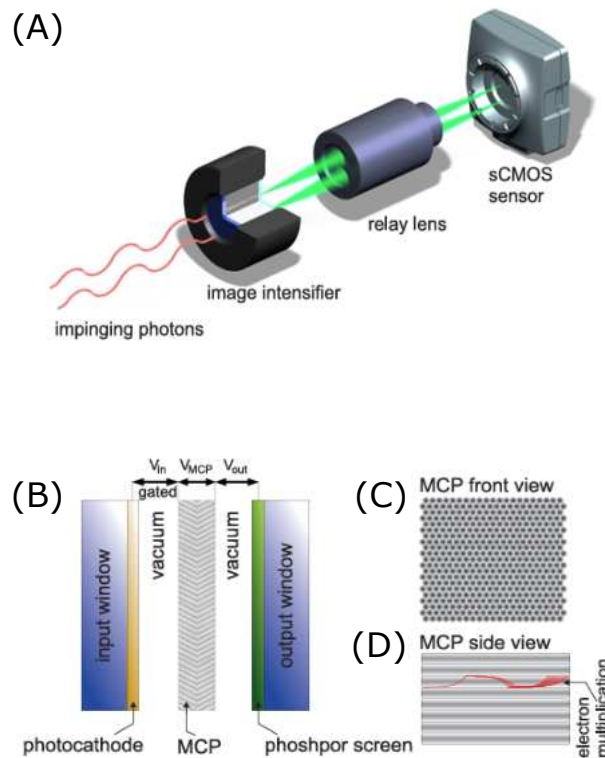


FIGURE 5.4: **Schematic representation of the intensified sCMOS camera and the constituents of the image intensifier.** Adapted from [110]. (A) The assembly of an intensified sCMOS camera, sensitive to single photons. Photons striking the image intensifier generate electrons, which are amplified within the device and then converted back into light on a phosphor screen. These flashes are captured by the sCMOS camera sensor using a bright relay lens. (B) Constituents of the image intensifier and its operation. Photons entering through the input window strike the photocathode, where the photoelectric effect takes place. The resulting electrons are accelerated by the gated voltage V_{in} towards the microchannel plate (MCP), where they undergo multiplication under the influence of the voltage V_{MCP} . The amplified electrons are further accelerated by the output voltage V_{out} before striking the phosphor screen, which emits flashes of light that exit through the output window. (C) When viewed from the front, the MCP comprises approximately 9 million individual tubes, each functioning as an electron multiplier. (D) An electron entering a single tube repeatedly collides with its walls, generating a significant charge avalanche.

5.2.4 Simulating the experiment with an attenuated laser

As a first step, we replace the signal photons in the experiment after the long loop of SMF with an attenuated continuous wave laser of wavelength 780 nm. We attenuate the laser of power 5 mW with absorptive neutral density filters of a combined optical density of 12. The idler photons from the source are used to open the gating module connected to the image intensifier, as described above. After acquiring camera frames for 5 minutes, a total number of approximately 0.7 million events was registered. In this case, due to the short time of acquisition, the dark counts

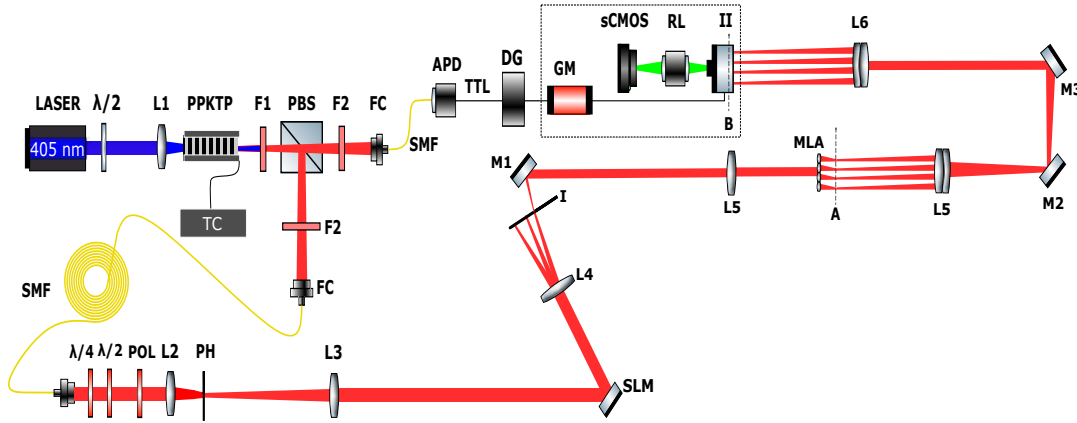


FIGURE 5.5: **Experimental setup to observe quantum optical backflow with heralded single photons.** The gating module (GM), image intensifier (II), relay lens (RL), and scientific CMOS (sCMOS) device comprise the intensified sCMOS camera (marked by a box). The idler photon from the Type-II collinear SPDC process described in Fig. (5.5) is used to synchronise the opening time of the gating module (GM) connected to the image intensifier (II) with the arrival of the signal photon from the experiment. The signal photons from the aforementioned SPDC process pass through a long spool of single mode fiber (SMF), followed by quarter wave plate ($\lambda/4$), a half wave plate ($\lambda/2$) and a polarizer (POL). They are spatially filtered by the lens L2 ($f=75$ mm), a pinhole (PH) and lens L3 ($f=300$ mm) and imaged onto the spatial light modulator (SLM). A hologram (not shown here) to generate the superposition of two beams, each carrying negative OAM, is applied on the SLM (see Chapter 4 for further details). The first diffraction order in the Fourier plane of lens L4 ($f=150$ mm) is isolated by an iris (I). The spatially filtered beam is then Fourier transformed again by lens L5 ($f=150$ mm) onto the microlens array (MLA). The back-focal plane of the MLA is imaged onto the photocathode of the II via achromatic doublets L5 ($f=50$ mm) and L6 ($f=200$ mm). M1, M2, and M3 are mirrors to redirect the beam path.

were negligible. The results are shown in Fig. (5.6). As explained in the figure caption, the counterclockwise motion of the pink arrows in the second subplot of Fig. (5.6) represents anomalous directions of local wave-vectors in the dark fringes of a superposition of two beams carrying negative OAM.

5.2.5 Difficulties in realising the experiment with heralded single photons and possible solutions

There are several challenges associated with realizing the experiment with heralded single photons with the existing setup. They are listed below along with possible solutions that are currently being implemented.

1. Humidity accumulation on the sCMOS sensor, when it is cooled, to reduce dark counts, causes speckle-like spots in a spotfield (see Fig. (5.7)). Thus, in order to obtain reasonable results, the cooling process had to be stopped and the sensor temperature was maintained at 26.5°C .
2. The arrival of signal photons onto the camera sensor is governed by the opening time (40 ns) of the gate of the image intensifier by pulses from the APD

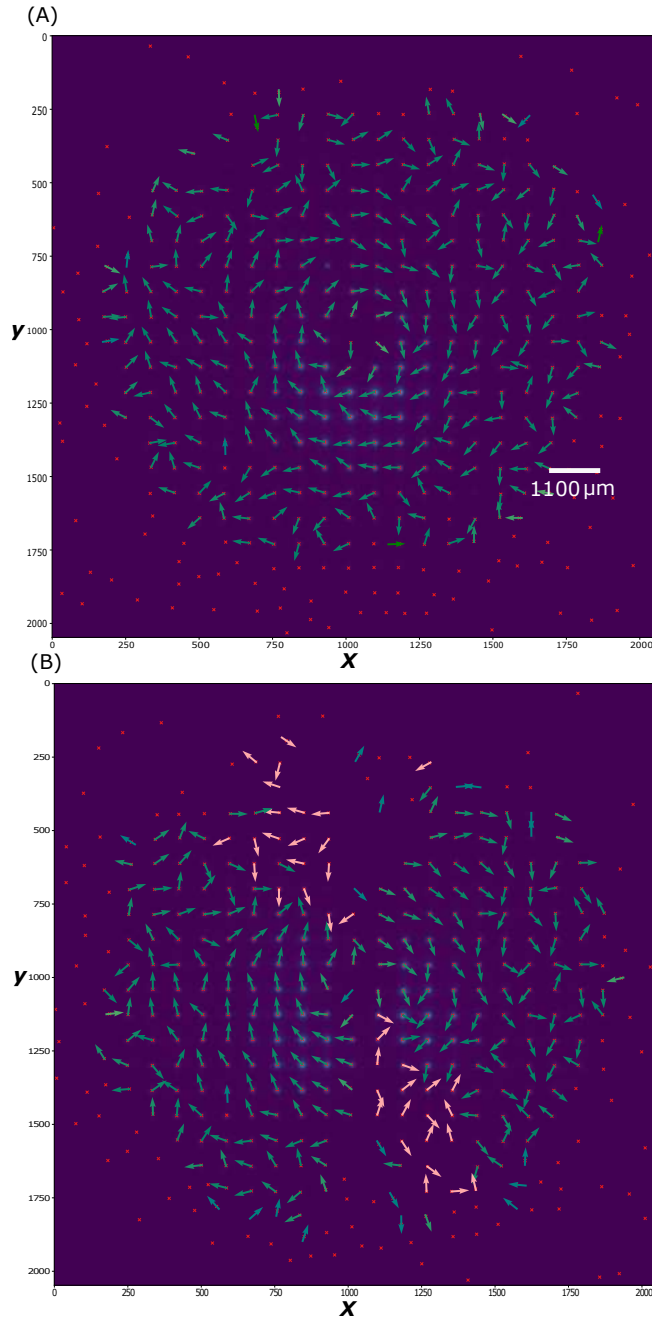


FIGURE 5.6: **Azimuthal backflow observed with an attenuated laser in the single photon counting regime.** The arrows on top of each detected spot (centroids marked with red crosses) represent the directions of normalized local wave-vectors (proportional to displacements of the corresponding spot centroids w.r.t. the reference spots). The axes are marked in pixels. The size of each pixel is $6.5 \times 6.5 \mu\text{m}^2$. (A) The normalized local wave-vectors in green of a beam with Gaussian amplitude and azimuthal phase of order $\ell = -3$. A general clockwise orientation of the arrows is observed, thus confirming the presence of a beam carrying a single OAM. A similar plot (not shown here) of normalized local wave-vectors on top of the spotfield can be observed for a beam with Gaussian amplitude and azimuthal phase of order $\ell = -5$. (B) The normalized local wave-vectors of the superposition of two beams, each with the same Gaussian amplitude profile, an amplitude ratio of 0.7, and azimuthal phases of order $\ell = -3$ and $\ell = -5$ respectively. The counterclockwise arrows in pink, in the dark fringes, are representative of azimuthal backflow. For higher radii, the directions of the arrows are often random, owing to decreasing intensity of the spots along the Gaussian tails.

that receives the idler photons. In addition, a dead time of $3.3 \mu\text{s}$ is set between the pulses to reduce the background. These conditions, along with the long loop of SME, and the properties of the chosen non-linear crystal, cause the total number of 'true' (heralded) signal photons detected per second to be as low as 400.

Over a 24-hour period, with any mask applied to the SLM, an average of 9 million events were recorded by the camera. In contrast, when the signal photons were blocked during the same 24-hour timeframe, an average of 7 million dark counts were detected. This indicates that, under the given experimental conditions, the signal-to-noise ratio is quite low.

3. The length of the PPKTP crystal (5 mm) and the focal lengths of the coupling lenses (8 mm), are suboptimal and ratio of coincidences to single counts is difficult to improve. For a discussion on the optimization of the pump beam focusing and crystal properties, the reader is directed to [111].

The aforementioned issues cause the centroids of the spotfields generated from heralded signal photons to be difficult to discern beyond the Poisson noise limit even when the photons are collected for a duration of 24 hours. See Fig. (5.8) for a sample image of the spotfield generated from the signal photons. The detected centroids are marked with red crosses in Fig. (5.9). Additionally, see Fig. (5.10) for a plot of local wave-vectors generated from a mask with azimuthal phase on the SLM, following the acquisition of heralded signal photons. It is important to note that most of the arrows are scattered. See Fig. (5.11) for a sample of the dark counts/background.

In order to observe backflow in transverse local momentum with single photons, the ratio of coincidences to singles from the SPDC source should be improved by utilizing a longer PPKTP crystal.

Additionally, the detection mechanism can be improved by utilizing a Timepix camera (TPX3CAM from Amsterdam Scientific Instruments) [112, 113, 114, 115]. These cameras were designed, in an initiative associated with CERN, to capture and time-stamp individual quantum events, such as a photon detection, with high temporal resolution (down to a couple of nanoseconds) as well as good spatial resolution (256×256 pixels; $55 \mu\text{m}$ pixel pitch). TTL pulses from the APD receiving the idler photon can be directly connected to the camera and can be used as time-stamps for the arrival of the signal photon. The image intensifier's gate can be externally opened, with a large duty cycle, under these circumstances. The use of the Timepix camera in the setup can reduce dark counts and improve the signal-to-noise ratio by at least a factor of 7, since the problems of the dead time of the image intensifier ($3.3 \mu\text{s}$) and the long coincidence window (40 ns compared to the Timepix's ~ 3 ns), can be bypassed.

5.3 Concluding remarks

This chapter outlines key advancements toward the observation of anomalous transverse local momenta in single-photon wave-functions. A simulation was conducted to analyze Poisson noise effects in the low-light regime. A heralded single-photon source was developed, and an experimental setup for observing quantum optical backflow was implemented, incorporating a $4f$ imaging system between the microlens array's back-focal plane and the image intensifier's photo-cathode. These efforts culminated in the observation of azimuthal backflow in the single-photon regime. Furthermore, local momenta consistent with a helical wavefront generated

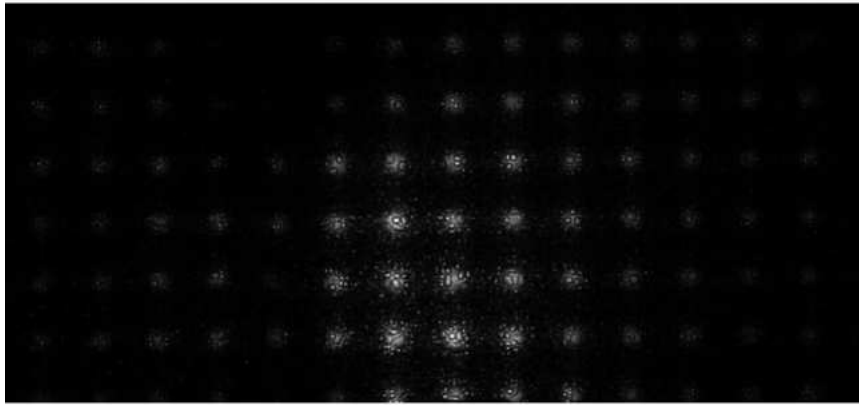


FIGURE 5.7: **Speckle-like spots owing to humidity that condenses on the sCMOS sensor, on account of cooling.** In order to avoid this, the sensor temperature was maintained at 26.5°C , leading to an increase in thermal noise.

from heralded single photons were successfully observed. Challenges encountered during the observation of azimuthal backflow using the heralded single-photon source were identified, and mitigation strategies were discussed.

Once understood, the high dimensionality of the orbital angular momentum state was harnessed in quantum communication tasks. See [116] and references therein for an overview. Similarly, the counterintuitive observation of azimuthal backflow in single photons may be extended to a system of entangled photons to investigate the combination of backflow and nonlocal correlations.

Contributions: The author has designed the experimental setup, constructed the experimental setup, performed the experiment, performed simulations, and analyzed the preliminary data. Jakub Lawandowski has assisted in constructing the experimental setup, the SPDC source, in particular. Bernard Gorzkowski has assisted in analyzing the preliminary data and in performing simulations. Radek Łapkiewicz has supervised the project.

After this chapter (and most of the dissertation) was written and long after its contents were presented at several scientific conferences [SQL 23, VCQ 23, Complex Waves 24, MIRAQLS 24, SQL 24], we recently learned of an almost identical work (slightly different detection mechanism) by Zhang *et al* [117].

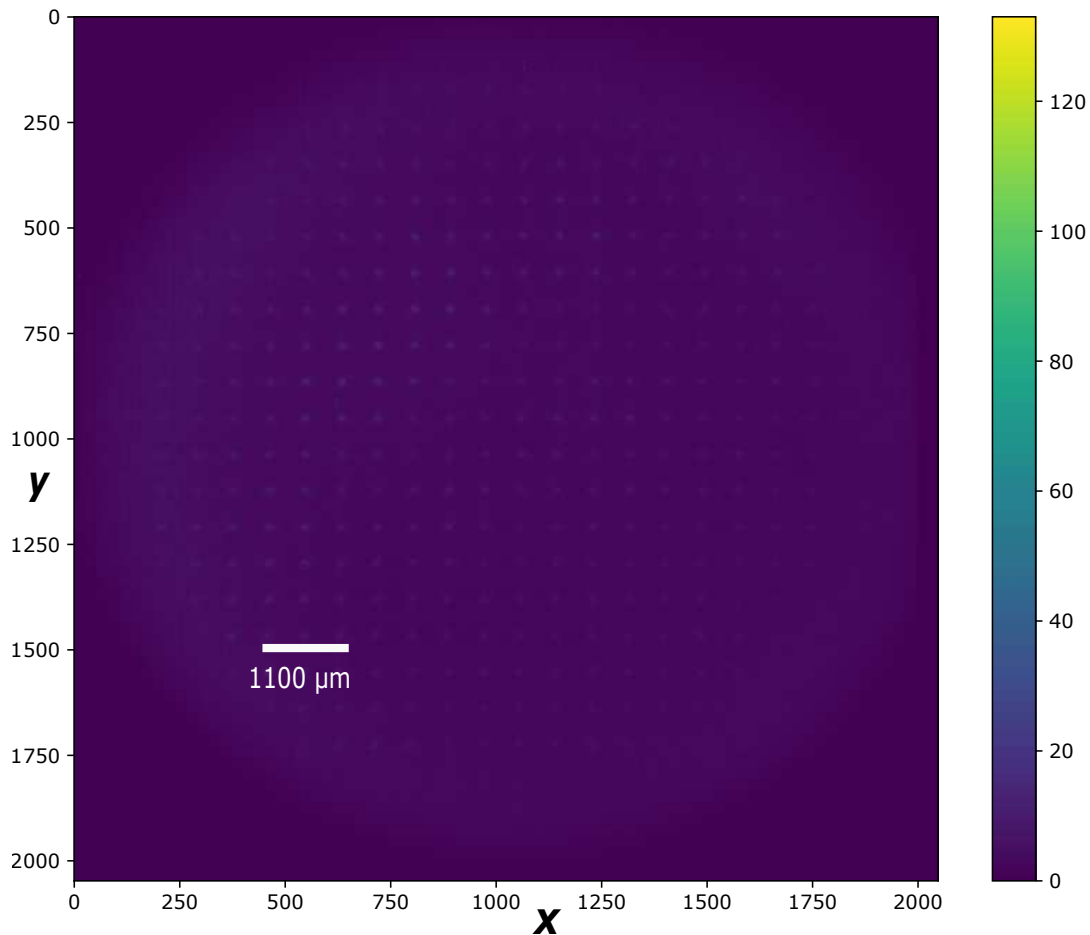


FIGURE 5.8: **Sample photon spotfield from a Gaussian mask on the SLM and 24 hours of photon acquisition.** The axes are represented in pixels. The scale bar shows the approximate separation between the centroids of two adjacent spots. The image is generated by adding a count to the pixel of a matrix of size 2048×2048 pixels where the Gaussian spot of the detected photon was centered on the camera. A halo, predominantly from dark counts, is seen towards the edge of the image. A diagonal pattern of bright and dark fringes are seen on the spots and can be fixed with some changes in the alignment.

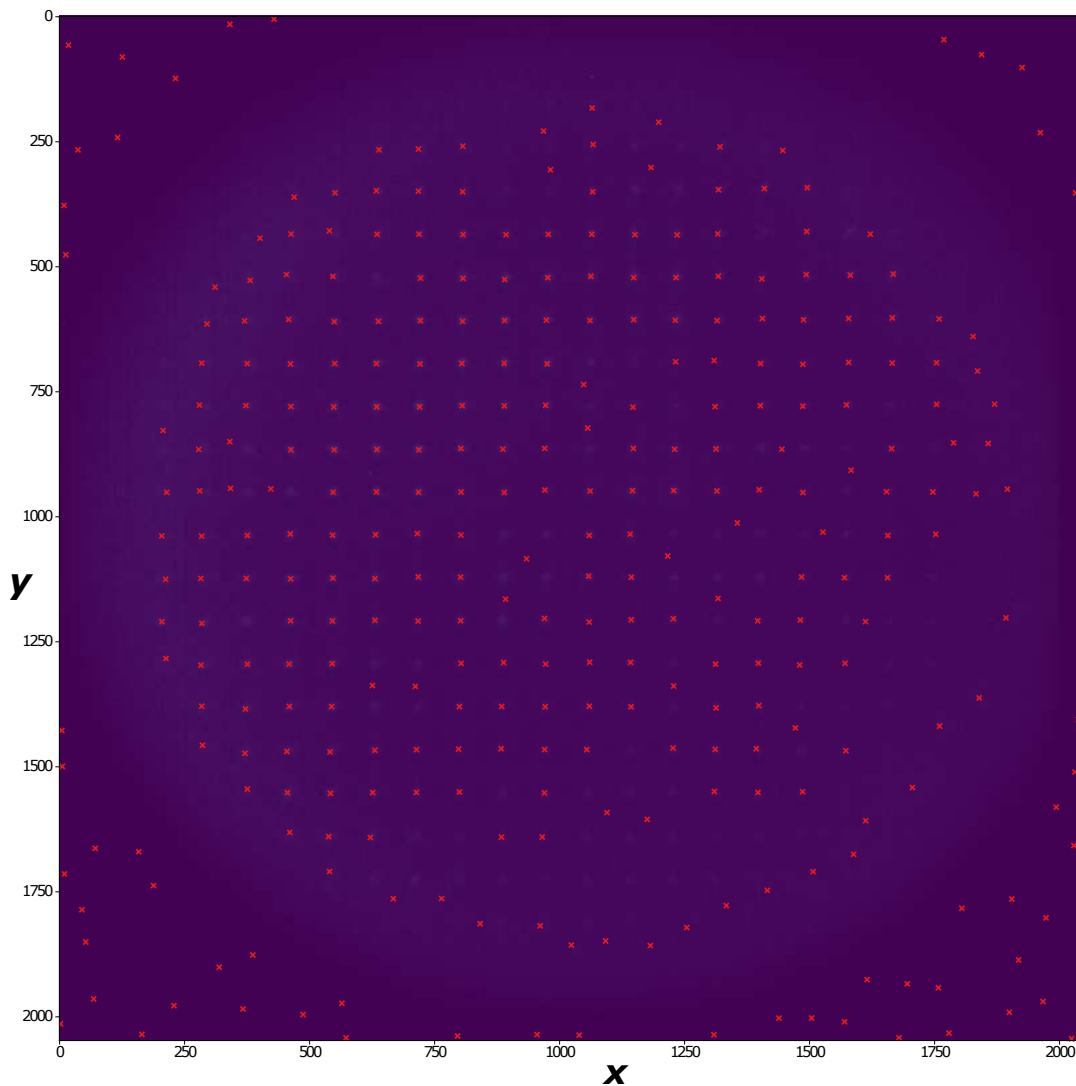


FIGURE 5.9: **Detected spot centroids for the spotfield in Fig. (5.8).** As discussed in section 2.1.3, owing to the low number of signal photons, several spots centroids are not identified, while others are misidentified. As the reference spot-centroids are misidentified, displacements of field spot-centroids w.r.t. the reference, i.e., measurement of the local wave-vector, are also erroneous.

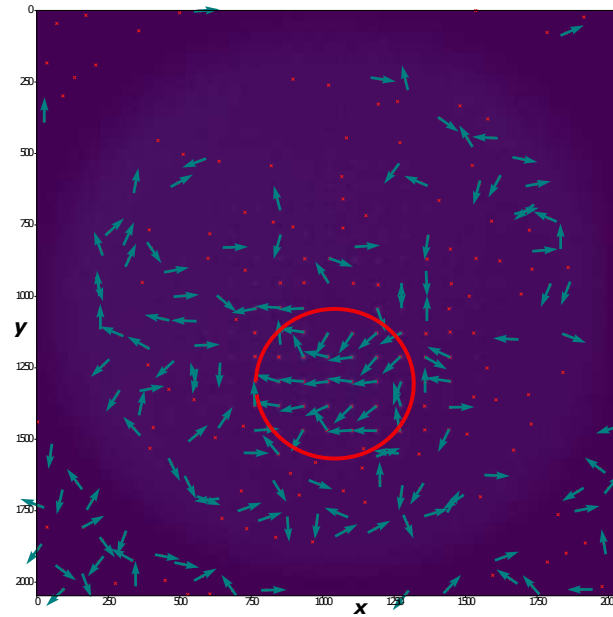


FIGURE 5.10: **Detected spot centroids and local wave-vectors using heralded single photons.** A mask with Gaussian amplitude and azimuthal phase ($\ell = -3$) was applied on the SLM. A spotfield is generated after 24 hours of collection of the heralded signal photons. It is compared to a reference spotfield (similar to the one presented in Fig. (5.8)) and the normalised local wave-vectors are obtained (plotted in green). The detected spot centroids are marked with red crosses. The axes are represented in pixels. The separation between two adjacent spots is $1100 \mu\text{m}$. The region marked in red, shows arrows pointing in the expected direction. However, owing to the Poisson noise and dark counts, most of the spot centroids are not detected.

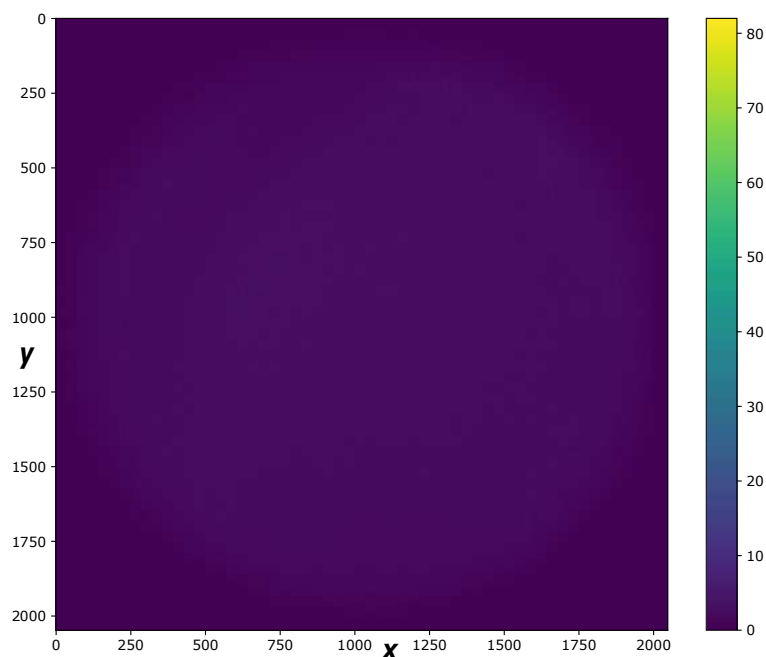


FIGURE 5.11: **Sample of dark counts/ background with the signal photons blocked, collected for 24 hours.** A dim halo that also appears in Fig. (5.8) is seen.

Chapter 6

Quantum backflow with electrons: a proposal

6.1 Introduction and motivation

In this chapter, we present a proposal to observe backflow of electrons within a transmission electron microscope (TEM). To date, there have been no experimental demonstrations of counter-propagation or probability backflow in massive quantum particles. The experimental realization of the proposed method is currently underway. This proposal aims to detect a counter-intuitive shift in intensity in the transverse direction between two consecutive planes along the electron beam's propagation axis (see Section 6.3).

To better contextualize this proposal, it is necessary to discuss the analogy between light optics and electron optics, which serves as a foundation for this chapter [118, 119]. The principles governing electron optics are conceptually analogous to those of light optics, as both systems exhibit wave-like behavior, albeit arising from different underlying mechanisms. This analogy is rooted in the wave-particle duality of electrons, as described by quantum mechanics, and the wave nature of light, as described by classical optics. When electrons are isolated from the environment, they exhibit wave-like properties characterized by the de Broglie wavelength. Analogous to lenses in light optics, electron optics in modern TEMs utilize magnetic lenses to bend or focus electron beams. As an electron traveling parallel to the optical axis enters a magnetic lens, the Lorentz force induces a helical trajectory while leaving the longitudinal momentum component largely unaffected. In advanced TEMs, the rotational motion caused by one lens is compensated for by adjustments in other lenses.

Under the paraxial approximation, akin to geometric optics, the effects of lenses on electrons traveling near the optical axis can be simplified. However, spherical aberrations arise from non-paraxial rays and require separate consideration. Additionally, diffraction phenomena such as Fresnel and Fraunhofer diffraction apply equally to both light and electrons.

For the purposes of this proposal, we assume that the electron beam emitted by the TEM source (see Section 6.2) and accelerated by a high voltage is approximately monochromatic or mono-energetic. This quasi-monochromatic beam is further assumed to remain close to the optical axis, which defines the propagation direction, as it passes through the TEM. During this process, the beam interacts with the sample and is influenced by the system's lenses. Within the paraxial approximation, the propagation along the optical axis can be interpreted as equivalent to the progression of time. Since TEM lenses minimally affect longitudinal motion, we can assume

(even beyond the paraxial approximation) that the transverse and longitudinal dynamics of the electrons are governed by separable wave-functions. Consequently, the electrons possess an effective mass and a de Broglie wavelength in the transverse direction, which differ from those along the propagation axis.

This proposal predicts that implementing the experimental setup will reveal a counter-intuitive shift in the transverse intensity distribution of the electrons between two planes perpendicular to the propagation direction (see Subsection 6.3.1). If realized, this shift would constitute an observation of quantum backflow with a massive particle in its purest form, as introduced in Chapter 1. A complete analysis of the energy spread among the electrons in the beam and a relaxation of the paraxial approximation would add complexity to the problem, but the essence of the phenomenon would remain intact.

6.2 A very brief introduction to the TEM and its operation

A TEM can be broadly separated into three main components: (1) the illumination system, which includes an electron gun and a condenser system that shapes the electron beam for the sample; (2) the objective lens region, encompassing the sample and its holder; and (3) the imaging system [120]. A brief description of these components follows.

The electron beam is generated by extracting electrons from the source and accelerating them through an electric field to a specific energy level, determined by the operating voltage of the microscope. Higher acceleration voltages yield electrons with greater energy, shorter effective wavelengths, and higher mean free paths. For experimentally realizing the proposal discussed in this chapter, a FEI Titan microscope will operate at a voltage between 100-200 kV; the voltage may be chosen by taking the resolution achievable and the de Broglie wavelength suitable for observing backflow (given the properties of the double slits, see section 6.3 below) into consideration. The condenser system, comprising optical elements such as lenses, apertures, and scan coils, enables the beam to be shaped into a parallel or convergent form before it interacts with the sample.

The sample is situated between the illumination and imaging systems. It is mounted on a sample holder, which facilitates its transfer and precise positioning within the microscope via a support stage. These stages typically allow for three-dimensional positioning and tilting of the sample along one axis to optimize its orientation during imaging.

The imaging system encompasses all optical components located between the sample and the TEM's phosphorescent screen. This system generally includes intermediate and projector lenses, as well as apertures such as the objective aperture and the selected area diffraction (SAD) aperture, which can be inserted as needed. In some cases, an image aberration corrector may also be incorporated to minimize spherical aberrations, thereby enhancing imaging resolution. The imaging system operates in two primary modes: imaging mode and diffraction mode.

In the imaging mode, the lenses are configured to project the image plane of the objective lens, and an image of the sample appears on the screen. In the diffraction mode, the lenses are configured to project the back focal plane of the objective lens, and the Fourier transform of the sample appears on the screen. See Fig. (6.1) below for a schematic representation of these two modes. To realize the proposal discussed in this chapter, we plan to operate the TEM in the diffraction mode.

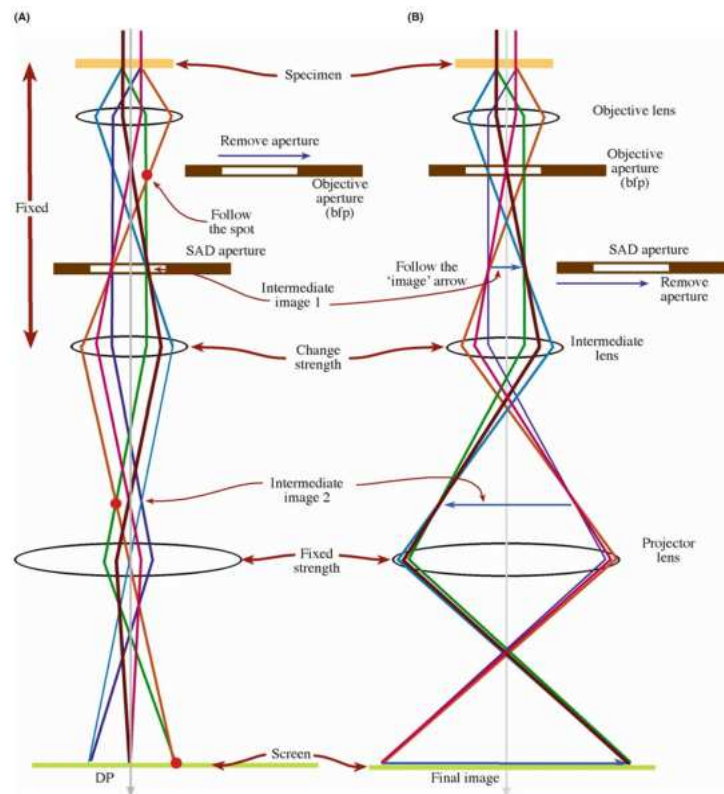


FIGURE 6.1: **The two modes of operation of the imaging system in a TEM.** The illumination system is not shown here. The two basic operations of the TEM imaging system involve (A) diffraction mode: projecting the diffraction pattern (DP) onto the viewing screen and (B) image mode: projecting the image onto the screen. In each case the intermediate lens selects either the back focal plane (BFP) (A) or the image plane (B) of the objective lens as its object. The imaging systems shown here are highly simplified. A basic principle of TEM operation is that when the DP (i.e., the BFP of the objective lens) is to be observed using parallel illumination, a selected-area-diffraction (SAD) aperture is inserted into the image plane of the objective lens to acquire the diffraction pattern of a specific area. See [120] for further information on the figure.

6.3 Backflow with electrons in a TEM

In order to avoid large electron optical aberrations in a TEM, the beam must be confined to a very narrow domain in the vicinity of the optical axis. Thus, as mentioned earlier, paraxial wave optics is assumed. Under this assumption, a sample of two slits with different widths can be used for the demonstration of a reasonable percentage of backflow (higher than that achievable with a single slit, i.e., the scenario represented in Fig (1.4)), as discussed below.

6.3.1 Theoretical description under the paraxial approximation

The phenomena of diffraction, interference and hence backflow in paraxial electron waves [118, 119], can be described using the mathematical tools introduced in section (1.2.1). Using a double slit in the front focal plane of the objective leads to a

higher percentage of backflow compared to a single slit. See Fig. (6.2) for a simplified schematic representation of the setup. The normalised amplitude transmittance

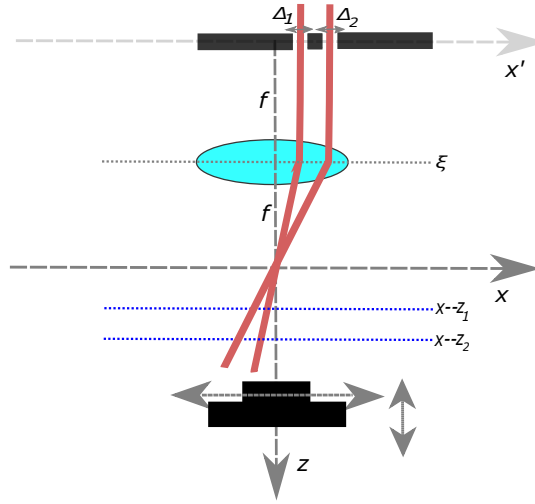


FIGURE 6.2: **A toy model of the setup to observe backflow with electrons.** A simple model of the TEM setup to observe backflow using two slits of widths Δ_1 and Δ_2 , centered around positive x_1 and x_2 respectively, in the front-focal plane of the objective lens (represented as a convex lens in blue; in reality this is a complex system of several electric and magnetic fields). $z = 0$ at the back-focal plane of the objective lens. The relative amplitude transmittance of the second slit to the first— $\tan \gamma$ —is not depicted in the figure. After the back-focal plane of the intensity of the electron beam should propagate towards the negative x . However, backflow occurs when the intensity of the superposition moves back to the positive x between planes z_1 and z_2 . To access the z_1 and z_2 planes, in the TEM, lenses used to image the back-focal plane of the objective can be de-focused (a standard procedure in a TEM) and the appropriate image magnifications can be taken into account while obtaining the probability of backflow. All angles are small such that the paraxial approximation is valid.

of the double slit is given as follows.

$$t_A(x') = \frac{\cos \gamma}{\sqrt{\Delta_1}} \text{rect} \left(\frac{x' - x_1}{\Delta_1} \right) + \frac{\sin \gamma}{\sqrt{\Delta_2}} \text{rect} \left(\frac{x' - x_2}{\Delta_2} \right) \quad (6.1)$$

Here, Δ_1 and Δ_2 are the widths and x_1 and x_2 are centres of the slits on the positive conjugate position space (x') respectively. Additionally, $\tan \gamma$ is the relative amplitude ratio between the slits. This can be incorporated by depositing thin films on the slits while preparing them (typically using electron beam lithography). As seen in Fig. (6.2), using principles of geometric optics [121, 122], the rays of electrons, after passing through the slits in the front focal plane of the objective lens (focal length f), following the deflection by the objective lens, should continue to travel along the left half of the x axis (after the back focal plane of the objective). Thus, one may naturally assume that by measuring the counts/ intensity along $x - z$ planes by scanning the camera in the x and z directions, the counts on the right half-planes gradually decrease along the direction of propagation. However, as explained in Chapter 1, owing to the wave nature of electrons, the counter-intuitive phenomenon of backflow may be observed, if a right set of physical parameters are chosen. Note that in a TEM, the detector doesn't move. Nonetheless, various planes, along the directions

of propagation can be imaged onto the detector by de-focusing or changing the field strengths of lenses in the imaging system.

One can argue that the growth in counts across any $x > L$ ($x = L$ is parallel to the z axis) between two transverse $x - z$ planes, can be considered as backflow as long as the electrons are prepared with positive momenta, i.e., the slits are placed entirely on the positive half of the $x' - z$ plane.

From the amplitude transmittance in eqn. (6.1) it can be shown using Fraunhofer and Fresnel integrals that the probability of finding the electron in $x > L$ at propagation distance z is given by

$$\begin{aligned}
P = & \frac{1}{2} - \frac{1}{2\pi} \int_{-1}^1 d\tilde{u} \left\{ \cos^2 \gamma \text{Si} [v(\alpha - \mu\beta\tilde{z} - v\tilde{z}\tilde{u})(1 - |\tilde{u}|)] + \sin^2 \gamma \text{Si} [(\alpha - \beta\tilde{z} - \tilde{z}\tilde{u})(1 - |\tilde{u}|)] \right\} \\
& - \frac{\sin 2\gamma}{4\pi\sqrt{v}} \int_{-\frac{1}{2}(1+v)}^{-\frac{1}{2}(1-v)} d\tilde{u} \left\{ \text{Si} \left[\left(v + \frac{1-\mu}{2}\beta + \tilde{u} \right) \left(\alpha - \frac{1+\mu}{2}\beta\tilde{z} - \tilde{z}\tilde{u} \right) \right] \right. \\
& + \text{Si} \left[\left(1 - \frac{1-\mu}{2}\beta + \tilde{u} \right) \left(\alpha - \frac{1+\mu}{2}\beta\tilde{z} - \tilde{z}\tilde{u} \right) \right] \left. \right\} \\
& - \frac{\sin 2\gamma}{4\pi\sqrt{v}} \int_{-\frac{1}{2}(1-v)}^{\frac{1}{2}(1-v)} d\tilde{u} \left\{ \text{Si} \left[\left(v + \frac{1-\mu}{2}\beta + \tilde{u} \right) \left(\alpha - \frac{1+\mu}{2}\beta\tilde{z} - \tilde{z}\tilde{u} \right) \right] \right. \\
& + \text{Si} \left[\left(v - \frac{1-\mu}{2}\beta - \tilde{u} \right) \left(\alpha - \frac{1+\mu}{2}\beta\tilde{z} - \tilde{z}\tilde{u} \right) \right] \left. \right\} \\
& - \frac{\sin 2\gamma}{4\pi\sqrt{v}} \int_{\frac{1}{2}(1-v)}^{\frac{1}{2}(1+v)} d\tilde{u} \left\{ \text{Si} \left[\left(1 + \frac{1-\mu}{2}\beta - \tilde{u} \right) \left(\alpha - \frac{1+\mu}{2}\beta\tilde{z} - \tilde{z}\tilde{u} \right) \right] \right. \\
& + \text{Si} \left[\left(v - \frac{1-\mu}{2}\beta - \tilde{u} \right) \left(\alpha - \frac{1+\mu}{2}\beta\tilde{z} - \tilde{z}\tilde{u} \right) \right] \left. \right\}, \tag{6.2}
\end{aligned}$$

where, the relevant dimensionless parameters are:

$$\alpha = \frac{k\Delta_2 L}{f}; \beta = \frac{2(-x_2)}{\Delta_2}; \tilde{z} = \frac{k\Delta_2^2 z}{2f^2}; v = \frac{\Delta_1}{\Delta_2}; \mu = \frac{x_1}{x_2}.$$

Here, $k = 2\pi/\lambda$ is the wavenumber and λ is the de Broglie wavelength of the electrons due to the acceleration voltage. Note that it is assumed that the slits are located entirely in positive x' and that the spacing between their centers is more than the sums of their half widths, such that the slits are distinct. Additionally, without loss of any generality, it is assumed that $\Delta_1 < \Delta_2$. The angle γ is in the first quadrant. Mathematically, these assumptions may be represented as follows.

$$0 < v < 1; \beta < 0; |\beta| > \max\left\{ \frac{1+v}{|1-\mu|}, \frac{v}{\mu}, 1 \right\}; 0 \leq \gamma \leq \frac{\pi}{2}$$

Using these assumptions, sets of parameters maximising the percentage of backflow can be found (see Fig. (6.3) for an example) by means of a random search followed by optimisation. In order to further visualise the backward motion of the normalised field intensity between two z planes after the back-focal plane of the objective lens, let us represent it in terms of the aforementioned dimensionless parameters.

$$|A(x, z)|^2 = \rho_1(x, z) + \rho_2(x, z) + \rho_{12}(x, z), \tag{6.3}$$

where

$$\begin{aligned}\rho_1(x, z) &= \frac{(\cos^2 \gamma) \alpha}{4\pi} \frac{1}{L} \int_{-1}^1 d\tilde{u} \int_{-v(1-|\tilde{u}|)}^{v(1-|\tilde{u}|)} d\tilde{v} e^{i\tilde{v}[\frac{\alpha x}{L} - \mu\beta\tilde{z} - v\tilde{z}\tilde{u}]} \\ \rho_2(x, z) &= \frac{(\sin^2 \gamma) \alpha}{4\pi} \frac{1}{L} \int_{-1}^1 d\tilde{u} \int_{-(1-|\tilde{u}|)}^{(1-|\tilde{u}|)} d\tilde{v} e^{i\tilde{v}[\frac{\alpha x}{L} - \beta\tilde{z} - \tilde{z}\tilde{u}]} \\ \rho_{12}(x, z) &= \frac{\sin 2\gamma}{2\lambda f \sqrt{\Delta_1 \Delta_2}} (r_1(x, z) + r_2(x, z) + r_3(x, z)) \\ &= r'_1(x, z) + r'_2(x, z) + r'_3(x, z),\end{aligned}\tag{6.4}$$

and

$$\begin{aligned}r'_1(x, z) &= \frac{\sin 2\gamma \alpha}{4\pi\sqrt{v}L} \int_{-\frac{1}{2}(1+v)}^{-\frac{1}{2}(1-v)} d\tilde{u} \int_{-(1-\frac{1-\mu}{2}\beta+\tilde{u})}^{(v+\frac{1-\mu}{2}\beta+\tilde{u})} d\tilde{v} \cos[\tilde{v}\{\frac{\alpha x}{L} - \frac{1+\mu}{2}\beta\tilde{z} - \tilde{z}\tilde{u}\}] \\ r'_2(x, z) &= \frac{\sin 2\gamma \alpha}{4\pi\sqrt{v}L} \int_{-\frac{1}{2}(1-v)}^{\frac{1}{2}(1-v)} d\tilde{u} \int_{-(v-\frac{1-\mu}{2}\beta-\tilde{u})}^{(v+\frac{1-\mu}{2}\beta+\tilde{u})} d\tilde{v} \cos[\tilde{v}\{\frac{\alpha x}{L} - \frac{1+\mu}{2}\beta\tilde{z} - \tilde{z}\tilde{u}\}] \\ r'_3(x, z) &= \frac{\sin 2\gamma \alpha}{4\pi\sqrt{v}L} \int_{\frac{1}{2}(1-v)}^{\frac{1}{2}(1+v)} d\tilde{u} \int_{-(v-\frac{1-\mu}{2}\beta-\tilde{u})}^{(1+\frac{1-\mu}{2}\beta-\tilde{u})} d\tilde{v} \cos[\tilde{v}\{\frac{\alpha x}{L} - \frac{1+\mu}{2}\beta\tilde{z} - \tilde{z}\tilde{u}\}]\end{aligned}\tag{6.5}$$

For the parameters in the titles of Fig. (6.3), given that $\lambda = 3$ pm; $f = 2$ mm, and

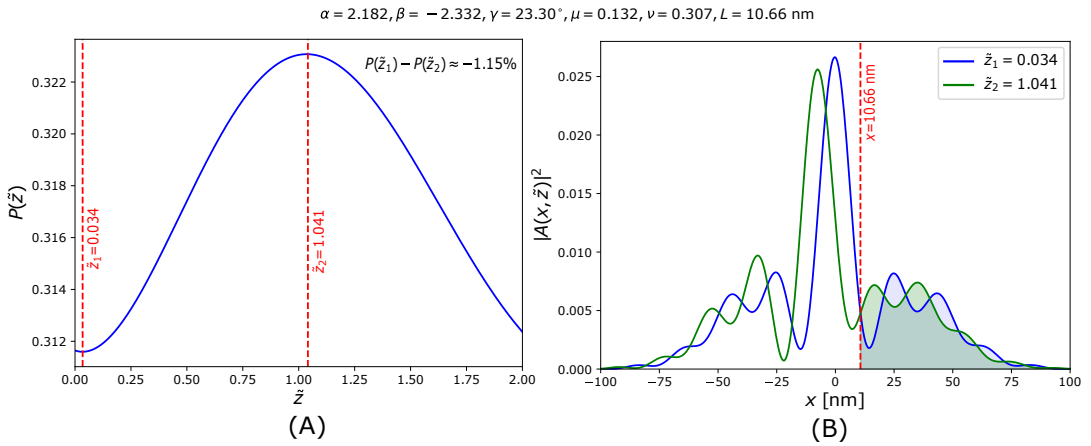


FIGURE 6.3: **A set of parameters leading to backflow.** (A) Probability of entering $x > L$ grows by 1.15 % between \tilde{z}_1 and \tilde{z}_2 . The values of the corresponding dimensionless parameters are mentioned in the title of the plot. Appropriate physical parameters are given in the main text. Amongst these, a choice of L is 10.66 nm. (B) Intensity crossing $x > L = 10.66$ nm grows by about 1.17 % between propagation planes \tilde{z}_1 and \tilde{z}_2 . x and L are in the same units [nm].

radius of aperture of the objective lens: 25 μm , we can make the following choice for the corresponding physical parameters.

1. Slit widths: $\Delta_1 = 60$ nm; $\Delta_2 = 195.44$ nm
2. slit centers: $x_1 = 30.08$ nm; $x_2 = 227.88$ nm; $|x_2 - x_1| = 197.8$ nm $\ll 25\mu\text{m}$
3. zero of the x-axis, $L = 10.66$ nm
4. $z_1 = 3.4\mu\text{m}$; $z_2 = 104.1\mu\text{m}$
5. $\tan \gamma = 0.431$

The relative amplitude ratio $\tan \gamma \neq 1$ can be challenging to implement while preparing slit samples using electron beam lithography or other methods. Additionally, even if such a sample can be prepared, the effect of charging (accumulation of excess charge from the electron beam illumination in non-conducting materials) due to the deposition thicknesses on the slits may lead to further distortions. Hence, another example of experiment-friendly physical parameters leading to backflow after setting $\tan \gamma = 1$ is shown in Fig (6.4) below. It is evident from subplots (B) in Figs.

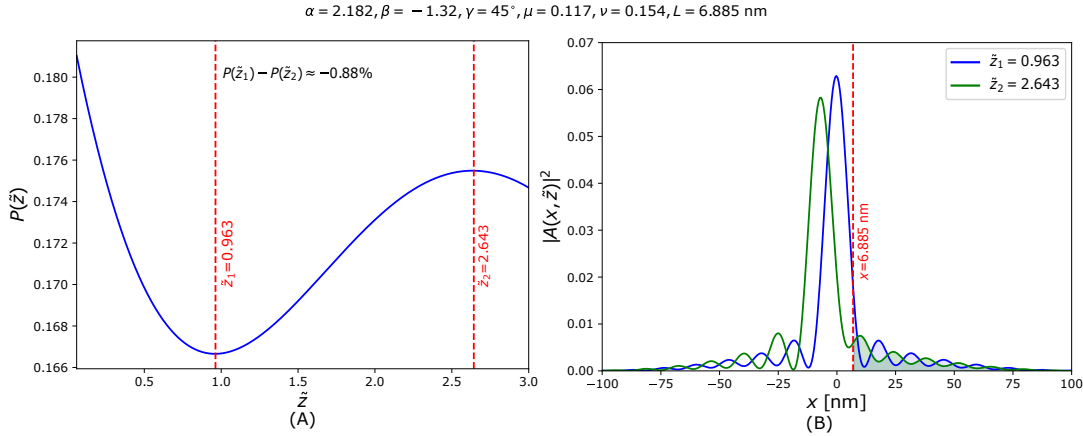


FIGURE 6.4: **A set of parameters leading to backflow assuming no relative amplitude ratio between the slits.** (A) Probability of entering $x > L$ grows by 0.88 % between \tilde{z}_1 and \tilde{z}_2 . The values of the corresponding dimensionless parameters are mentioned in the title of the plot. Once again, $\lambda = 3 \text{ pm}$ and $f = 2 \text{ mm}$. By choosing $\Delta_1 = 60 \text{ nm}$, we have $\Delta_2 = 389.34 \text{ nm}$, $x_1 = 30.002 \text{ nm}$, $x_2 = 257.003 \text{ nm}$, and $L = 6.885 \text{ nm}$. The planes z_1 and z_2 between which the aforementioned percentage of backflow occurs are $24.26 \mu\text{m}$ and $66.60 \mu\text{m}$ respectively. (B) Intensity crossing $x > L = 6.885 \text{ nm}$ grows by about 0.88 % between propagation planes \tilde{z}_1 and \tilde{z}_2 . x and L are in the same units [nm].

(6.3) and (6.4) that while the center of mass of the intensity distribution moves to the left between the planes \tilde{z}_1 and \tilde{z}_2 as expected, the area under the curve to the right of $x = L$, grows between the planes \tilde{z}_1 and \tilde{z}_2 . This notion of backflow can also be explained in terms of percentiles of the probability density, according to Dr. Arseni Goussev. Keeping in mind wave-functions that are solutions of the one dimensional Schrödinger equation, discussed in Chapter 1, let us define C -percentile $M(C, t)$ of the probability density $|\Psi(x, t)|^2$ as follows.

$$\int_{-\infty}^{M(C,t)} dx |\Psi(x, t)|^2 = C. \quad (6.6)$$

Here, $0 \leq C \leq 1$. If the particle in question has positive momentum, using the continuity equation, it can be shown that the occurrence of backflow is equivalent to the existence of C, t_1, t_2 with $t_1 < t_2$, such that the following inequality holds true.

$$M(C, t_2) < M(C, t_1) \quad (6.7)$$

This essentially means that backflow occurs when the particle, moving to the right, can be found in a comparatively leftward region with the same probability at a later time. This insight can also be translated to our problem using the paraxial approximation and the equivalence between t and \tilde{z} .

6.4 Images of a double slit from a TEM in diffraction mode



FIGURE 6.5: **Images collected in diffraction mode from a TEM using a double slit sample.** Courtesy: Prof. Thomas Juffmann. (Top left) Image of the slits (obtained in imaging mode), placed in the front focal plane of the objective along the center of the optic axis. The scale bar indicates that the slit separation is $\sim 2.5 \mu\text{m}$, the width of each slit is $\sim 0.5 \mu\text{m}$, and its length is $\sim 15 \mu\text{m}$. (Top right, bottom left and bottom right) Diffraction pattern of the slits at different z planes, obtained by offsetting the sample stage and changing the field strength of the imaging lenses. The top right panel indicates the diffraction pattern when the sample is placed at the eucentric height (see main text). The other planes are determined with respect to this plane. The rotations of the diffraction pattern between the top right panel and the other two panels are due to helical trajectories of the electrons set by the lenses. The scale-bar in all three plots indicates a distance in frequency space.

The operation of the TEM (FEI Technai F20 at 200 kV) with a double slit sample (equal widths and no amplitude ratio), placed along the center of the optical axis (hence there is no restriction of positivity on the momentum distribution), was tested by Prof. Thomas Juffmann's group at the Sternwarte in Vienna. See Fig. (6.5) for images of the preliminary results. In the top left panel, an image of the slits is shown. From the top right, bottom left, and bottom right panels, we see diffraction patterns (obtained in the diffraction mode) of the double slit, at different z planes. The top left panel shows the diffraction pattern at the *eucentric* height. When the sample holder is placed at this height, then the objective lens strength is always the same when the image on the screen is in focus [120]. All other planes in the imaging system are defined with respect to the eucentric plane. Rotations of the diffraction pattern at different z planes are due to helical trajectories of electrons set by the lenses. Furthermore, analyses (ongoing) of the preliminary results can be found in this [Google collaboration notebook](#). While the diffraction patterns are as expected

from a double slit, in order to observe backflow, a double slit sample with suitable experimental parameters must be prepared and rotations due to the imaging system should be corrected in post-processing. Instead of preparing a sample of slits with different widths, the effect of unequal widths may also be obtained by placing a movable mask in the intermediate image plane of the objective lens (marked in Fig. (6.1)) [123].

6.5 Concluding remarks

An experimental proposal to observe backflow with electrons in a TEM, is presented in this chapter. A set of experimentally realizable parameters is also presented. As argued in the introductory section of this chapter and in Chapter 1, while the previous observations of backflow were based on anomalous transverse local momenta, i.e., optical analogues of backflow in quantum mechanics, an experimental realization of the proposal discussed here would be a true demonstration of the counter-intuitive flow of probability density for a massive particle, i.e., of the phenomenon of backflow in its original sense. The effect of backflow for a sample of double slits is around 1% and cannot be much higher as the bound of 4% [15] can be achieved only by specific backflow-maximising states. A preliminary data set from operating a TEM in the diffraction mode using a double slit sample is also presented in this chapter.

In order to certify the observation of such a small effect, spherical aberrations, image shifts (due to defocusing; can be measured with sub-pixel accuracy and pixel size is $\sim 50 \mu\text{m}$), image rotations, the precision of translations (in transverse and longitudinal directions) and rotations of the sample holder, must be taken into account and the theoretical description must be modified accordingly. Although the rate of electrons from the source in a TEM ($\sim 10^7 - 10^{10}$ electrons per second) and the quantum efficiency of the detectors are typically better than those discussed for single photons in Chapter 5, shot noise or Poisson noise that occurs due to fluctuations in the detection process, should also be taken into account for a complete analysis.

Contributions: The author contributed to conceptualizing the idea, designing the setup, performing simulations, and conducting theoretical calculations. Thomas Juffmann contributed to conceptualizing the idea, designing the setup, and supervising the collection of preliminary data. Arseni Goussev and Tomasz Paterek contributed to developing the theoretical framework. Thomas Juffmann and Radek Lapkiewicz supervised the project.

Chapter 7

Conclusion and outlook

7.1 Dissertation summary

In summary, this dissertation explores the concept of anomalous "local" momentum arising in the superposition of states with well-defined momenta, a phenomenon recognized in quantum mechanics since the 1960s. Such states, which exhibit anomalous local behaviour or backflow, have more recently been linked to the concept of superoscillations in optics, as developed by Michael Berry and collaborators. By investigating the occurrence of superoscillatory local wave-vectors or backflow within the straightforward interference of two unequal beams, this work uncovers the critical role of the interference angle and amplitude ratio. This simplification not only demystifies the phenomenon, but also lays the groundwork for its broader accessibility and potential applications in future research.

Chapter 2 introduces the one-shot measurement of transverse local momentum using a Shack-Hartmann wavefront sensor (SHWFS). It examines potential errors in the algorithm employed to determine the spot centroids from the spotfield captured on the SHWFS sensor. The chapter also explores the distinction between local momentum and the Poynting vector, utilising the insensitivity of the SHWFS to polarization: the SHWFS measures the transverse components of phase changes, corresponding to transverse local momentum, rather than the spin-dependent Poynting momentum.

Chapter 3 details the experimental observation of an anomalous local transverse component of the wave-vector generated by the interference of two wide Gaussian beams with unequal amplitudes using a SHWFS. This serves as an optical analogue of the backflow phenomenon previously discussed in quantum mechanics (Chapter 1). While backflow has traditionally been regarded as exotic and challenging to observe, this work demonstrates that it is, in fact, difficult to avoid in practice. Experimental constraints, such as achieving perfectly equal beam intensities, make backflow a near-inevitable feature of such systems. Moreover, this study provides control over key parameters—amplitude ratio and interference angle—while elucidating their physical relevance, thereby offering a deeper understanding of the effect.

Chapter 4 builds on the observations from Chapter 3, extending the analysis to the superposition of two beams with helical phases and unequal amplitudes. In this case, "azimuthal backflow," or an anomalous azimuthal component of the local wave-vector scaled by the radius, is observed within the dark fringes, once again using the two-dimensional one-shot measurement offered by the SHWFS. Since the angular spectra of the constituent beams are discrete, backflow can be directly verified through measurement. This approach offers a significant advantage over previous

demonstrations, where the Fourier spectra of the constituent beams were infinite, necessitating careful validation to ensure that the observed local linear momentum was not a result of the infinite tails of the Fourier spectrum. This is because beams with well-defined orbital angular momentum (OAM) can be experimentally generated, whereas plane waves cannot.

Chapter 5 examines an experiment aimed at extending the observation of azimuthal backflow to the single-photon regime. The detection of the transverse local wave-vector is accomplished using the SHWFS technique described earlier, now combined with an intensified camera to achieve enhanced sensitivity at low photon levels. To obtain reliable results with heralded single photons, improvements are needed in the efficiency of the SPDC source, as well as the replacement of the current camera with one that provides higher temporal resolution and a shorter coincidence window. Despite these challenges, this represents the first attempt to observe counterintuitive transverse local momenta with single quantum particles, aligning with how the phenomenon was originally proposed.

Chapter 6 builds on the concept of interfering two beams with unequal amplitudes, introduced earlier in the dissertation, to propose an experiment aimed at observing the counter-intuitive propagation of single electrons in a transmission electron microscope (TEM). This represents the first-ever attempt to experimentally verify quantum backflow, with the experimental work currently underway in the group of Prof. Thomas Juffmann.

7.2 Outlook

7.2.1 On the distinction between canonical momentum and Poynting momentum

In Chapter 2, we demonstrated that the local momentum (canonical momentum) of circularly polarized Laguerre-Gauss beams, as measured by a SHWFS, exhibits distinct characteristics compared to the Poynting momentum. The SHWFS, being insensitive to polarization components, measures the local or canonical momentum density. Another approach for distinguishing between canonical and Poynting momentum densities involves examining the radially dependent rotation of truncated paraxial vortex beams along the propagation direction [67]. Additionally, the concept of "supermomentum" near a vortex core emerges due to polarization-dependent nonparaxial correction terms in the canonical momentum density, rather than from the Poynting vector [67].

This work highlights the theoretical utility of canonical momentum density in understanding the free-space evolution of monochromatic light fields. Future studies could extend this framework to encompass more complex scenarios, such as polychromatic optical fields or structured light in anisotropic media. Exploring these directions would deepen our understanding of light-matter interactions in diverse optical systems.

7.2.2 On the observations of optical backflow with classical light

Our experiments, detailed in Chapters 3 and 4, demonstrate the presence of anomalous transverse local momentum in the dark fringes of the interference of two beams and highlight that such anomalies arise due to high phase gradients over a certain spatial extent. These gradients significantly influence the interaction of electromagnetic fields with atoms and molecules, facilitating the excitation of higher-order

multipole transitions—a fundamental process in the development of ultra-precise atomic clocks [34, 35] and in the detection of photons in the dark regions of beams with complex spatial structures [104].

Our findings open avenues for designing electromagnetic fields with non-conservative forces, which can exhibit locally retrograde radiation pressure and enable "tractor-beam"-like behavior, drawing small particles toward the light source [33, 102, 124]. Another compelling application lies in light-matter interactions with chiral molecules mediated by optical fields exhibiting azimuthal backflow. While small chiral molecules usually respond to the spin (circular polarization) of light rather than the helical wavefronts associated with extrinsic orbital angular momentum, this behavior could shift in regions of tight focusing, at shorter wavelengths, or where the wavefront changes rapidly—such as in backflow regions [87]. For instance, 'superchiral' light can be produced by creating a standing wave from two counter-propagating circularly polarized beams with opposite handedness and slightly different amplitudes [91]. Similarly, our experiments demonstrate that the simple superposition of two beams with slightly different amplitudes provides an intuitive and effective method for generating rapid phase changes.

7.2.3 On the attempt to observe optical backflow with single photons

The experiment presented in Chapter 5 demonstrates the feasibility of using a Shack-Hartmann wavefront sensor (SHWFS)-based technique to detect anomalous transverse local momenta in single-photon wave-functions. Beyond this specific application, the setup—incorporating a microlens array imaged onto an intensified camera—has broader potential for investigating spatial properties of biphotons, as highlighted in prior studies [125]. However, the spatial and spatial frequency resolutions of the system remain constrained by the microlens pitch size and the aperture's point spread function, respectively.

Despite these limitations, the integration of a microlens array with an imaging camera is versatile, particularly in its ability to simultaneously capture positional and angular information. This capability aligns with its application in fast 3D imaging techniques, such as plenoptic imaging [126]. Furthermore, a fundamentally different yet complementary approach to plenoptic imaging—known as "correlation plenoptic imaging"—offers intriguing prospects. This method, suitable for chaotic light and SPDC-generated biphotons, involves spatial and directional measurements on separate sensors, with the data later combined through correlation analysis [127].

Expanding the application of the discussed setup, its capacity to measure the wavefront as a function of propagation direction and transverse position opens avenues for studying photon trajectories in exotic optical fields, such as those exhibiting azimuthal backflow [53]. On the quantum front, this setup holds promise for exploring enhanced backflow effects in photon number states, which offer increased phase sensitivity [128]. These advancements could pave the way for future explorations in both fundamental physics and applied imaging technologies.

7.2.4 On the experimental proposal to observe quantum backflow in a TEM

A significant portion of contemporary research in quantum theory centers on leveraging quantum effects for communication and computation. However, quantum systems were originally appreciated for their benefits in mechanical processes, with the tunneling effect and its applications, such as in scanning tunneling microscopy,

serving as notable examples. The tunneling effect allows a quantum particle to appear in regions that are classically inaccessible due to energy constraints. Similarly, quantum backflow, a phenomenon where a free quantum particle with positive momentum can later reappear in a region it had previously vacated, holds potential for mechanical applications.

In this context, Trillo *et al.* have theoretically demonstrated the superiority of quantum mechanical systems over classical counterparts in a practical transportation task involving a projectile, connecting the scenario to quantum backflow [129]. A projectile of a fixed mass is prepared in a bound region in space along the x -axis at time $t = 0$. The maximum quantum advantage (compared to a classical particle with the same parameters) in the probability of detecting the particle in a part of the x -axis further on the right, is found to be 4 %, i.e., the bound set by Bracken and Melloy [15]. Generally, mechanical "paradoxes" like quantum backflow emerge because position is a quantum observable, not merely a classical label. Moreover, exploring time-of-arrival scenarios [7, 8, 9] could pave the way for a deeper understanding of time in quantum theory.

Our experimental proposal to demonstrate quantum backflow using single electrons (discussed in Chapter 6) inspires questions on the use of TEMs to implement quantum-advantaged transportation tasks [129]. Discussions with Prof. Miguel Navascués, the last author of [129], suggest that applying the frameworks of quantum information science—particularly those focused on operational tasks with well-defined figures of merit—to the study of mechanical phenomena could provide further insights into the fundamental nature of space and time.

Bibliography

- [1] G Möllenstedt and H Düker. “Fresnelscher Interferenzversuch mit einem Biprisma für Elektronenwellen”. In: *Naturwissenschaften* 42.2 (Jan. 1955), pp. 41–41.
- [2] Anton Zeilinger et al. “Single- and double-slit diffraction of neutrons”. In: *Rev. Mod. Phys.* 60 (4 Oct. 1988), pp. 1067–1073. DOI: [10.1103/RevModPhys.60.1067](https://doi.org/10.1103/RevModPhys.60.1067). URL: <https://link.aps.org/doi/10.1103/RevModPhys.60.1067>.
- [3] Daniel M Greenberger, Michael A Horne, and Anton Zeilinger. “Multiparticle interferometry and the superposition principle”. en. In: *Phys. Today* 46.8 (Aug. 1993), pp. 22–29.
- [4] O. Carnal and J. Mlynek. “Young’s double-slit experiment with atoms: A simple atom interferometer”. In: *Phys. Rev. Lett.* 66 (21 May 1991), pp. 2689–2692. DOI: [10.1103/PhysRevLett.66.2689](https://doi.org/10.1103/PhysRevLett.66.2689). URL: <https://link.aps.org/doi/10.1103/PhysRevLett.66.2689>.
- [5] Thomas Juffmann et al. “Real-time single-molecule imaging of quantum interference”. en. In: *Nat Nanotechnol* 7.5 (Mar. 2012), pp. 297–300. DOI: <https://doi.org/10.1038/nnano.2012.34>. URL: <https://www.nature.com/articles/nnano.2012.34>.
- [6] M V Berry. “Quantum backflow, negative kinetic energy, and optical retro-propagation”. In: *Journal of Physics A: Mathematical and Theoretical* 43.41 (Sept. 2010), p. 415302. DOI: [10.1088/1751-8113/43/41/415302](https://doi.org/10.1088/1751-8113/43/41/415302). URL: <https://dx.doi.org/10.1088/1751-8113/43/41/415302>.
- [7] G.R. Allcock. “The time of arrival in quantum mechanics I. Formal considerations”. In: *Annals of Physics* 53.2 (1969), pp. 253–285. ISSN: 0003-4916. DOI: [https://doi.org/10.1016/0003-4916\(69\)90251-6](https://doi.org/10.1016/0003-4916(69)90251-6). URL: <https://www.sciencedirect.com/science/article/pii/0003491669902516>.
- [8] G.R. Allcock. “The time of arrival in quantum mechanics II. The individual measurement”. In: *Annals of Physics* 53.2 (1969), pp. 286–310. ISSN: 0003-4916. DOI: [https://doi.org/10.1016/0003-4916\(69\)90252-8](https://doi.org/10.1016/0003-4916(69)90252-8). URL: <https://www.sciencedirect.com/science/article/pii/0003491669902528>.
- [9] G.R. Allcock. “The time of arrival in quantum mechanics III. The measurement ensemble”. In: *Annals of Physics* 53.2 (1969), pp. 311–348. ISSN: 0003-4916. DOI: [https://doi.org/10.1016/0003-4916\(69\)90253-X](https://doi.org/10.1016/0003-4916(69)90253-X). URL: <https://www.sciencedirect.com/science/article/pii/000349166990253X>.
- [10] Nicola Vona and Detlef Dürr. “The Role of the Probability Current for Time Measurements”. In: *The Message of Quantum Science: Attempts Towards a Synthesis*. Ed. by Philippe Blanchard and Jürg Fröhlich. Berlin, Heidelberg: Springer Berlin Heidelberg, 2015, pp. 95–112. ISBN: 978-3-662-46422-9. DOI: [10.1007/978-3-662-46422-9_5](https://doi.org/10.1007/978-3-662-46422-9_5). URL: https://doi.org/10.1007/978-3-662-46422-9_5.

- [11] Simone Roncallo, Krzysztof Sacha, and Lorenzo Maccone. "When does a particle arrive?" In: *Quantum* 7 (Mar. 2023), p. 968. ISSN: 2521-327X. DOI: [10.22331/q-2023-03-30-968](https://doi.org/10.22331/q-2023-03-30-968). URL: <https://doi.org/10.22331/q-2023-03-30-968>.
- [12] J.G. Muga, J.P. Palao, and C.R. Leavens. "Arrival time distributions and perfect absorption in classical and quantum mechanics". In: *Physics Letters A* 253.1 (1999), pp. 21–27. ISSN: 0375-9601. DOI: [https://doi.org/10.1016/S0375-9601\(99\)00020-1](https://doi.org/10.1016/S0375-9601(99)00020-1). URL: <https://www.sciencedirect.com/science/article/pii/S0375960199000201>.
- [13] J.G. Muga and C.R. Leavens. "Arrival time in quantum mechanics". In: *Physics Reports* 338.4 (2000), pp. 353–438. ISSN: 0370-1573. DOI: [https://doi.org/10.1016/S0370-1573\(00\)00047-8](https://doi.org/10.1016/S0370-1573(00)00047-8). URL: <https://www.sciencedirect.com/science/article/pii/S0370157300000478>.
- [14] J. A. Damborenea et al. "Measurement-based approach to quantum arrival times". In: *Phys. Rev. A* 66 (5 Nov. 2002), p. 052104. DOI: [10.1103/PhysRevA.66.052104](https://doi.org/10.1103/PhysRevA.66.052104). URL: <https://link.aps.org/doi/10.1103/PhysRevA.66.052104>.
- [15] A J Bracken and G F Melloy. "Probability backflow and a new dimensionless quantum number". In: *Journal of Physics A: Mathematical and General* 27.6 (Mar. 1994), p. 2197. DOI: [10.1088/0305-4470/27/6/040](https://doi.org/10.1088/0305-4470/27/6/040). URL: <https://dx.doi.org/10.1088/0305-4470/27/6/040>.
- [16] Arseni Goussev. "Quantum backflow in a ring". In: *Phys. Rev. A* 103 (2 Feb. 2021), p. 022217. DOI: [10.1103/PhysRevA.103.022217](https://doi.org/10.1103/PhysRevA.103.022217). URL: <https://link.aps.org/doi/10.1103/PhysRevA.103.022217>.
- [17] P Strange. "Large quantum probability backflow and the azimuthal angle–angular momentum uncertainty relation for an electron in a constant magnetic field". In: *European Journal of Physics* 33.5 (July 2012), p. 1147. DOI: [10.1088/0143-0807/33/5/1147](https://doi.org/10.1088/0143-0807/33/5/1147). URL: <https://dx.doi.org/10.1088/0143-0807/33/5/1147>.
- [18] Valentin Daniel Paccioia, Orlando Panella, and Pinaki Roy. "Angular momentum quantum backflow in the noncommutative plane". In: *Phys. Rev. A* 102 (6 Dec. 2020), p. 062218. DOI: [10.1103/PhysRevA.102.062218](https://doi.org/10.1103/PhysRevA.102.062218). URL: <https://link.aps.org/doi/10.1103/PhysRevA.102.062218>.
- [19] Maximilien Barbier, Arseni Goussev, and Shashi C. L. Srivastava. "Unbounded quantum backflow in two dimensions". In: *Phys. Rev. A* 107 (3 Mar. 2023), p. 032204. DOI: [10.1103/PhysRevA.107.032204](https://doi.org/10.1103/PhysRevA.107.032204). URL: <https://link.aps.org/doi/10.1103/PhysRevA.107.032204>.
- [20] G F Melloy and A J Bracken. "Probability Backflow for a Dirac Particle". In: *Foundations of Physics* 28.3 (Mar. 1998), pp. 505–514. URL: <https://doi.org/10.1023/A:1018724313788>.
- [21] Iwo Bialynicki-Birula, Zofia Bialynicka-Birula, and Szymon Augustynowicz. "Backflow in relativistic wave equations". In: *Journal of Physics A: Mathematical and Theoretical* 55.25 (May 2022), p. 255702. DOI: [10.1088/1751-8121/ac65c1](https://doi.org/10.1088/1751-8121/ac65c1). URL: <https://dx.doi.org/10.1088/1751-8121/ac65c1>.
- [22] M. Palmero et al. "Detecting quantum backflow by the density of a Bose-Einstein condensate". In: *Phys. Rev. A* 87 (5 May 2013), p. 053618. DOI: [10.1103/PhysRevA.87.053618](https://doi.org/10.1103/PhysRevA.87.053618). URL: <https://link.aps.org/doi/10.1103/PhysRevA.87.053618>.

- [23] Marek Miller et al. "Experiment-friendly formulation of quantum backflow". In: *Quantum* 5 (Jan. 2021), p. 379. ISSN: 2521-327X. DOI: [10.22331/q-2021-01-11-379](https://doi.org/10.22331/q-2021-01-11-379). URL: <https://doi.org/10.22331/q-2021-01-11-379>.
- [24] M V Berry and S Popescu. "Evolution of quantum superoscillations and optical superresolution without evanescent waves". In: *Journal of Physics A: Mathematical and General* 39.22 (May 2006), p. 6965. DOI: [10.1088/0305-4470/39/22/011](https://dx.doi.org/10.1088/0305-4470/39/22/011). URL: <https://dx.doi.org/10.1088/0305-4470/39/22/011>.
- [25] Fu Min Huang et al. "Optical super-resolution through super-oscillations". In: *Journal of Optics A: Pure and Applied Optics* 9.9 (Aug. 2007), S285. DOI: [10.1088/1464-4258/9/9/S01](https://dx.doi.org/10.1088/1464-4258/9/9/S01). URL: <https://dx.doi.org/10.1088/1464-4258/9/9/S01>.
- [26] Guanghui Yuan, Edward T. F. Rogers, and Nikolay I. Zheludev. "'Plasmonics' in free space: observation of giant wavevectors, vortices, and energy backflow in superoscillatory optical fields". In: *Light: Science & Applications* 8.1 (Jan. 2019), p. 2. ISSN: 2047-7538. DOI: [10.1038/s41377-018-0112-z](https://doi.org/10.1038/s41377-018-0112-z). URL: <https://doi.org/10.1038/s41377-018-0112-z>.
- [27] Michael Berry et al. "Roadmap on superoscillations". In: *Journal of Optics* 21.5 (Apr. 2019), p. 053002. DOI: [10.1088/2040-8986/ab0191](https://dx.doi.org/10.1088/2040-8986/ab0191). URL: <https://dx.doi.org/10.1088/2040-8986/ab0191>.
- [28] Roei Remez et al. "Superoscillating electron wave functions with subdiffraction spots". In: *Phys. Rev. A* 95 (3 Mar. 2017), p. 031802. DOI: [10.1103/PhysRevA.95.031802](https://link.aps.org/doi/10.1103/PhysRevA.95.031802). URL: <https://link.aps.org/doi/10.1103/PhysRevA.95.031802>.
- [29] Brijesh K Singh et al. "Particle manipulation beyond the diffraction limit using structured super-oscillating light beams". en. In: *Light Sci. Appl.* 6.9 (Mar. 2017), e17050–e17050. URL: <https://doi.org/10.1038/lsa.2017.50>.
- [30] Yaniv Eliezer, Thomas Zacharias, and Alon Bahabad. "Observation of optical backflow". In: *Optica* 7.1 (Jan. 2020), pp. 72–76. DOI: [10.1364/OPTICA.371494](https://opg.optica.org/optica/abstract.cfm?URI=optica-7-1-72). URL: <https://opg.optica.org/optica/abstract.cfm?URI=optica-7-1-72>.
- [31] Anat Daniel et al. "Demonstrating backflow in classical two beams' interference". In: *New Journal of Physics* 24.12 (Dec. 2022), p. 123011. DOI: [10.1088/1367-2630/aca70b](https://dx.doi.org/10.1088/1367-2630/aca70b). URL: <https://dx.doi.org/10.1088/1367-2630/aca70b>.
- [32] Bohnishikha Ghosh et al. "Azimuthal backflow in light carrying orbital angular momentum". In: *Optica* 10.9 (Sept. 2023), pp. 1217–1222. DOI: [10.1364/OPTICA.495710](https://opg.optica.org/optica/abstract.cfm?URI=optica-10-9-1217). URL: <https://opg.optica.org/optica/abstract.cfm?URI=optica-10-9-1217>.
- [33] S. Sukhov and A. Dogariu. "On the concept of "tractor beams"". In: *Opt. Lett.* 35.22 (Nov. 2010), pp. 3847–3849. DOI: [10.1364/OL.35.003847](https://opg.optica.org/ol/abstract.cfm?URI=ol-35-22-3847). URL: <https://opg.optica.org/ol/abstract.cfm?URI=ol-35-22-3847>.
- [34] Christian T Schmiegelow et al. "Transfer of optical orbital angular momentum to a bound electron". en. In: *Nat. Commun.* 7.1 (Oct. 2016), p. 12998.
- [35] R. Lange et al. "Excitation of an Electric Octupole Transition by Twisted Light". In: *Phys. Rev. Lett.* 129 (25 Dec. 2022), p. 253901. DOI: [10.1103/PhysRevLett.129.253901](https://link.aps.org/doi/10.1103/PhysRevLett.129.253901). URL: <https://link.aps.org/doi/10.1103/PhysRevLett.129.253901>.

- [36] J M Yearsley and J J Halliwell. "An introduction to the quantum backflow effect". In: *Journal of Physics: Conference Series* 442.1 (June 2013), p. 012055. DOI: [10.1088/1742-6596/442/1/012055](https://doi.org/10.1088/1742-6596/442/1/012055). URL: <https://dx.doi.org/10.1088/1742-6596/442/1/012055>.
- [37] Markus Penz et al. "A new approach to quantum backflow". In: *Journal of Physics A: Mathematical and General* 39.2 (Dec. 2005), p. 423. DOI: [10.1088/0305-4470/39/2/012](https://doi.org/10.1088/0305-4470/39/2/012). URL: <https://dx.doi.org/10.1088/0305-4470/39/2/012>.
- [38] Brian Davies. "Heaviside step function". In: *Integral Transforms and their Applications*. Springer, 2002.
- [39] Ruye Wang. *Introduction to orthogonal transforms*. Cambridge, England: Cambridge University Press, Mar. 2012.
- [40] Joseph W Goodman. "Introduction to Fourier optics". In: *Introduction to Fourier optics, 3rd ed., by JW Goodman*. Englewood, CO: Roberts & Co. Publishers, 2005 1 (2005).
- [41] Y Aharonov and D Rohrlich. *Quantum Paradoxes: Quantum Theory for the Perplexed*. Weinheim: Wiley VCH, 2005.
- [42] Nikolay I Zheludev and Guanghui Yuan. "Optical superoscillation technologies beyond the diffraction limit". en. In: *Nat. Rev. Phys.* 4.1 (Oct. 2021), pp. 16–32. DOI: <https://doi.org/10.1038/s42254-021-00382-7>. URL: <https://www.nature.com/articles/s42254-021-00382-7>.
- [43] Michael Berry. "Faster than Fourier". In: *A Half-Century of Physical Asymptotics and Other Diversions*. Chap. 5.1, pp. 483–493. DOI: [10.1142/9789813221215_0036](https://doi.org/10.1142/9789813221215_0036). eprint: https://www.worldscientific.com/doi/pdf/10.1142/9789813221215_0036. URL: https://www.worldscientific.com/doi/abs/10.1142/9789813221215_0036.
- [44] M V Berry and K T McDonald. "Exact and geometrical optics energy trajectories in twisted beams". In: *Journal of Optics A: Pure and Applied Optics* 10.3 (Feb. 2008), p. 035005. DOI: [10.1088/1464-4258/10/3/035005](https://doi.org/10.1088/1464-4258/10/3/035005). URL: <https://dx.doi.org/10.1088/1464-4258/10/3/035005>.
- [45] Gang Chen, Zhong-Quan Wen, and Cheng-Wei Qiu. "Superoscillation: from physics to optical applications". en. In: *Light Sci. Appl.* 8.1 (June 2019), p. 56. DOI: <https://doi.org/10.1038/s41377-019-0163-9>. URL: <https://www.nature.com/articles/s41377-019-0163-9>.
- [46] K S Rogers and E T F Rogers. "Realising superoscillations: A review of mathematical tools and their application". In: *Journal of Physics: Photonics* 2.4 (Aug. 2020), p. 042004. DOI: [10.1088/2515-7647/aba5a7](https://doi.org/10.1088/2515-7647/aba5a7). URL: <https://dx.doi.org/10.1088/2515-7647/aba5a7>.
- [47] Fu Min Huang et al. "Focusing of light by a nanohole array". en. In: *Appl. Phys. Lett.* 90.9 (Feb. 2007), p. 091119. DOI: <https://doi.org/10.1063/1.2710775>. URL: <https://pubs.aip.org/aip/apl/article-abstract/90/9/091119/933149/Focusing-of-light-by-a-nanohole-array?redirectedFrom=fulltext>.
- [48] P J S G Ferreira and A Kempf. "Superoscillations: Faster Than the Nyquist Rate IEEE Trans". In: *IEEE Trans. Signal Process* 54 (2006), pp. 3732–3740. DOI: [10.1109/TSP.2006.877642](https://doi.org/10.1109/TSP.2006.877642). URL: <https://ieeexplore.ieee.org/document/1703843>.

- [49] Edward T F Rogers et al. "Far-field unlabeled super-resolution imaging with superoscillatory illumination". en. In: *APL Photonics* 5.6 (Apr. 2020), p. 066107. DOI: <https://doi.org/10.1063/1.5144918>. URL: <https://pubs.aip.org/aip/app/article/5/6/066107/123550/Far-field-unlabeled-super-resolution-imaging-with>.
- [50] Maximilien Barbier et al. "Comment on 'Backflow in relativistic wave equations'". In: *J. Phys. A Math. Theor.* 56.13 (Mar. 2023), p. 138003. URL: <https://iopscience.iop.org/article/10.1088/1751-8121/acba62>.
- [51] A J Bracken and G F Melloy. "Comment on 'Backflow in relativistic wave equations'". In: *Journal of Physics A: Mathematical and Theoretical* 56.13 (Mar. 2023), p. 138002. DOI: [10.1088/1751-8121/acbd70](https://doi.org/10.1088/1751-8121/acbd70). URL: <https://dx.doi.org/10.1088/1751-8121/acbd70>.
- [52] Iwo Bialynicki-Birula, Zofia Bialynicka-Birula, and Szymon Augustynowicz. "Reply to comments on 'Backflow in relativistic wave equations'". In: *Journal of Physics A: Mathematical and Theoretical* 56.13 (Mar. 2023), p. 138001. DOI: [10.1088/1751-8121/acbd72](https://doi.org/10.1088/1751-8121/acbd72). URL: <https://dx.doi.org/10.1088/1751-8121/acbd72>.
- [53] Sacha Kocsis et al. "Observing the Average Trajectories of Single Photons in a Two-Slit Interferometer". In: *Science* 332.6034 (2011), pp. 1170–1173. DOI: [10.1126/science.1202218](https://doi.org/10.1126/science.1202218). eprint: <https://www.science.org/doi/pdf/10.1126/science.1202218>. URL: <https://www.science.org/doi/abs/10.1126/science.1202218>.
- [54] Konstantin Y. Bliokh, Aleksandr Y. Bekshaev, and Franco Nori. "Extraordinary momentum and spin in evanescent waves". In: *Nature Communications* 5.1 (Mar. 2014), p. 3300. ISSN: 2041-1723. DOI: [10.1038/ncomms4300](https://doi.org/10.1038/ncomms4300). URL: <https://doi.org/10.1038/ncomms4300>.
- [55] P Ehrenfest. "Bemerkung uber die angen :a herte G ultigkeit der klassischen Mechanik innerhalb der Quantenmechanik". de. In: *Eur. Phys. J. A* 45.7-8 (July 1927), pp. 455–457.
- [56] Nikolaos K. Efremidis et al. "Airy beams and accelerating waves: an overview of recent advances". In: *Optica* 6.5 (May 2019), pp. 686–701. DOI: [10.1364/OPTICA.6.000686](https://doi.org/10.1364/OPTICA.6.000686). URL: <https://opg.optica.org/optica/abstract.cfm?URI=optica-6-5-686>.
- [57] Roland V Shack. "Production and use of a lenticular Hartmann screen". In: *Spring Meeting of Optical Society of America, 1971*. Vol. 656. 1971.
- [58] Douglas G Altman and J Martin Bland. "Standard deviations and standard errors". en. In: *BMJ* 331.7521 (Oct. 2005), p. 903.
- [59] Fanpeng Kong, Manuel Cegarra Polo, and Andrew Lambert. "Centroid estimation for a Shack–Hartmann wavefront sensor based on stream processing". In: *Appl. Opt.* 56.23 (Aug. 2017), pp. 6466–6475. DOI: [10.1364/AO.56.006466](https://doi.org/10.1364/AO.56.006466). URL: <https://opg.optica.org/ao/abstract.cfm?URI=ao-56-23-6466>.
- [60] Vyas Akondi, Samuel Steven, and Alfredo Dubra. "Centroid error due to non-uniform lenslet illumination in the Shack–Hartmann wavefront sensor". In: *Opt. Lett.* 44.17 (Sept. 2019), pp. 4167–4170. DOI: [10.1364/OL.44.004167](https://doi.org/10.1364/OL.44.004167). URL: <https://opg.optica.org/ol/abstract.cfm?URI=ol-44-17-4167>.

- [61] Ziqiang Li and Xinyang Li. “Centroid computation for Shack-Hartmann wavefront sensor in extreme situations based on artificial neural networks”. In: *Opt. Express* 26.24 (Nov. 2018), pp. 31675–31692. DOI: [10.1364/OE.26.031675](https://doi.org/10.1364/OE.26.031675). URL: <https://opg.optica.org/oe/abstract.cfm?URI=oe-26-24-31675>.
- [62] Max Born and Emil Wolf. *Principles of optics*. 7th ed. Cambridge, England: Cambridge University Press, Oct. 1999.
- [63] Konstantin Y. Bliokh and Franco Nori. “Transverse and longitudinal angular momenta of light”. In: *Physics Reports* 592 (2015). Transverse and longitudinal angular momenta of light, pp. 1–38. ISSN: 0370-1573. DOI: <https://doi.org/10.1016/j.physrep.2015.06.003>. URL: <https://www.sciencedirect.com/science/article/pii/S0370157315003336>.
- [64] M V Berry. “Optical currents”. In: *Journal of Optics A: Pure and Applied Optics* 11.9 (Aug. 2009), p. 094001. DOI: [10.1088/1464-4258/11/9/094001](https://doi.org/10.1088/1464-4258/11/9/094001). URL: <https://dx.doi.org/10.1088/1464-4258/11/9/094001>.
- [65] M Antognozzi et al. “Direct measurements of the extraordinary optical momentum and transverse spin-dependent force using a nano-cantilever”. en. In: *Nat. Phys.* 12.8 (Aug. 2016), pp. 731–735.
- [66] Aaron Yevick, David B. Ruffner, and David G. Grier. “Tractor beams in the Rayleigh limit”. In: *Phys. Rev. A* 93 (4 Apr. 2016), p. 043807. DOI: [10.1103/PhysRevA.93.043807](https://doi.org/10.1103/PhysRevA.93.043807). URL: <https://link.aps.org/doi/10.1103/PhysRevA.93.043807>.
- [67] Bohnishikha Ghosh et al. “Canonical and Poynting currents in propagation and diffraction of structured light: tutorial”. In: *J. Opt. Soc. Am. B* 41.6 (June 2024), pp. 1276–1289. DOI: [10.1364/JOSAB.522393](https://doi.org/10.1364/JOSAB.522393). URL: <https://opg.optica.org/josab/abstract.cfm?URI=josab-41-6-1276>.
- [68] Aleksandr Bekshaev, Konstantin Y Bliokh, and Marat Soskin. “Internal flows and energy circulation in light beams”. In: *Journal of Optics* 13.5 (Mar. 2011), p. 053001. DOI: [10.1088/2040-8978/13/5/053001](https://doi.org/10.1088/2040-8978/13/5/053001). URL: <https://dx.doi.org/10.1088/2040-8978/13/5/053001>.
- [69] Jonathan Leach et al. “Direct measurement of the skew angle of the Poynting vector in a helically phased beam”. In: *Opt. Express* 14.25 (Dec. 2006), pp. 11919–11924. DOI: [10.1364/OE.14.011919](https://doi.org/10.1364/OE.14.011919). URL: <https://opg.optica.org/oe/abstract.cfm?URI=oe-14-25-11919>.
- [70] Kevin Murphy et al. “Experimental detection of optical vortices with a Shack-Hartmann wavefront sensor”. In: *Opt. Express* 18.15 (July 2010), pp. 15448–15460. DOI: [10.1364/OE.18.015448](https://doi.org/10.1364/OE.18.015448). URL: <https://opg.optica.org/oe/abstract.cfm?URI=oe-18-15-15448>.
- [71] Eliot Bolduc et al. “Exact solution to simultaneous intensity and phase encryption with a single phase-only hologram”. In: *Opt. Lett.* 38.18 (Sept. 2013), pp. 3546–3549. DOI: [10.1364/OL.38.003546](https://doi.org/10.1364/OL.38.003546). URL: <https://opg.optica.org/ol/abstract.cfm?URI=ol-38-18-3546>.
- [72] Andrea Rubano et al. “Q-plate technology: a progress review [Invited]”. en. In: *J. Opt. Soc. Am. B* 36.5 (May 2019), p. D70.
- [73] Yi Zheng et al. “Detecting momentum weak value: Shack–Hartmann versus a weak measurement wavefront sensor”. In: *Opt. Lett.* 46.21 (Nov. 2021), pp. 5352–5355. DOI: [10.1364/OL.439174](https://doi.org/10.1364/OL.439174). URL: <https://opg.optica.org/ol/abstract.cfm?URI=ol-46-21-5352>.

- [74] M V Berry. "Superoscillations and leaky spectra". In: *Journal of Physics A: Mathematical and Theoretical* 52.1 (Nov. 2018), p. 015202. DOI: [10.1088/1751-8121/aeebb](https://doi.org/10.1088/1751-8121/aeebb). URL: <https://dx.doi.org/10.1088/1751-8121/aeebb>.
- [75] Salvador Bará. "Measuring eye aberrations with Hartmann–Shack wave-front sensors: Should the irradiance distribution across the eye pupil be taken into account?" In: *J. Opt. Soc. Am. A* 20.12 (Dec. 2003), pp. 2237–2245. DOI: [10.1364/JOSAA.20.002237](https://doi.org/10.1364/JOSAA.20.002237). URL: <https://opg.optica.org/josaa/abstract.cfm?URI=josaa-20-12-2237>.
- [76] Vyas Akondi and Alfredo Dubra. "Accounting for focal shift in the Shack–Hartmann wavefront sensor". In: *Opt. Lett.* 44.17 (Sept. 2019), pp. 4151–4154. DOI: [10.1364/OL.44.004151](https://doi.org/10.1364/OL.44.004151). URL: <https://opg.optica.org/ol/abstract.cfm?URI=ol-44-17-4151>.
- [77] Jürgen Klepp, Stephan Sponar, and Yuji Hasegawa. "Fundamental phenomena of quantum mechanics explored with neutron interferometers". In: *Progress of Theoretical and Experimental Physics* 2014.8 (Aug. 2014), 082A01. ISSN: 2050-3911. DOI: [10.1093/ptep/ptu085](https://doi.org/10.1093/ptep/ptu085). eprint: <https://academic.oup.com/ptep/article-pdf/2014/8/082A01/34838799/ptu085.pdf>. URL: <https://doi.org/10.1093/ptep/ptu085>.
- [78] Yaakov Y. Fein et al. "Quantum superposition of molecules beyond 25 kDa". In: *Nature Physics* 15.12 (Dec. 2019), pp. 1242–1245. ISSN: 1745-2481. DOI: [10.1038/s41567-019-0663-9](https://doi.org/10.1038/s41567-019-0663-9). URL: <https://doi.org/10.1038/s41567-019-0663-9>.
- [79] Dominik Ehberger et al. "Highly Coherent Electron Beam from a Laser-Triggered Tungsten Needle Tip". In: *Phys. Rev. Lett.* 114 (22 June 2015), p. 227601. DOI: [10.1103/PhysRevLett.114.227601](https://doi.org/10.1103/PhysRevLett.114.227601). URL: <https://link.aps.org/doi/10.1103/PhysRevLett.114.227601>.
- [80] T. Schumm et al. "Matter-wave interferometry in a double well on an atom chip". In: *Nature Physics* 1.1 (Oct. 2005), pp. 57–62. ISSN: 1745-2481. DOI: [10.1038/nphys125](https://doi.org/10.1038/nphys125). URL: <https://doi.org/10.1038/nphys125>.
- [81] I Białynicki-Birula. "On the wave function of the photon *Acta Phys.*". In: *Acta Phys. Pol. A* 86 (1994).
- [82] Guang Hui Yuan et al. "Quantum super-oscillation of a single photon". In: *Light: Science & Applications* 5.8 (Mar. 2016), e16127–e16127. ISSN: 2047-7538. DOI: [10.1038/lsa.2016.127](https://doi.org/10.1038/lsa.2016.127). URL: <https://doi.org/10.1038/lsa.2016.127>.
- [83] L. Allen et al. "Orbital angular momentum of light and the transformation of Laguerre-Gaussian laser modes". In: *Phys. Rev. A* 45 (11 June 1992), pp. 8185–8189. DOI: [10.1103/PhysRevA.45.8185](https://doi.org/10.1103/PhysRevA.45.8185). URL: <https://link.aps.org/doi/10.1103/PhysRevA.45.8185>.
- [84] M.W. Beijersbergen et al. "Astigmatic laser mode converters and transfer of orbital angular momentum". In: *Optics Communications* 96.1 (1993), pp. 123–132. ISSN: 0030-4018. DOI: [https://doi.org/10.1016/0030-4018\(93\)90535-D](https://doi.org/10.1016/0030-4018(93)90535-D). URL: <https://www.sciencedirect.com/science/article/pii/003040189390535D>.

- [85] Aaron Yevick, Daniel J Evans, and David G Grier. “Photokinetic analysis of the forces and torques exerted by optical tweezers carrying angular momentum”. en. In: *Philos. Trans. A Math. Phys. Eng. Sci.* 375.2087 (Feb. 2017), p. 20150432. DOI: <https://doi.org/10.1098/rsta.2015.0432>. URL: <https://royalsocietypublishing.org/doi/10.1098/rsta.2015.0432>.
- [86] Monika Ritsch-Martens. “Orbital angular momentum light in microscopy”. en. In: *Philos. Trans. A Math. Phys. Eng. Sci.* 375.2087 (Feb. 2017), p. 20150437. DOI: <https://doi.org/10.1098/rsta.2015.0437>. URL: <https://royalsocietypublishing.org/doi/full/10.1098/rsta.2015.0437>.
- [87] Robert P Cameron et al. “Chirality and the angular momentum of light”. en. In: *Philos. Trans. A Math. Phys. Eng. Sci.* 375.2087 (Feb. 2017), p. 20150433. DOI: <https://doi.org/10.1098/rsta.2015.0433>. URL: <https://royalsocietypublishing.org/doi/10.1098/rsta.2015.0433>.
- [88] Igor A. Litvin, Angela Dudley, and Andrew Forbes. “Poynting vector and orbital angular momentum density of superpositions of Bessel beams”. In: *Opt. Express* 19.18 (Aug. 2011), pp. 16760–16771. DOI: [10.1364/OE.19.016760](https://doi.org/10.1364/OE.19.016760). URL: <https://opg.optica.org/oe/abstract.cfm?URI=oe-19-18-16760>.
- [89] Christian Schulze et al. “Measurement of the orbital angular momentum density of light by modal decomposition”. In: *New Journal of Physics* 15.7 (July 2013), p. 073025. DOI: [10.1088/1367-2630/15/7/073025](https://doi.org/10.1088/1367-2630/15/7/073025). URL: <https://dx.doi.org/10.1088/1367-2630/15/7/073025>.
- [90] Thomas Zacharias and Alon Bahabad. “Light beams with volume superoscillations”. In: *Opt. Lett.* 45.13 (July 2020), pp. 3482–3485. DOI: [10.1364/OL.394270](https://doi.org/10.1364/OL.394270). URL: <https://opg.optica.org/ol/abstract.cfm?URI=ol-45-13-3482>.
- [91] Yiqiao Tang and Adam E. Cohen. “Enhanced Enantioselectivity in Excitation of Chiral Molecules by Superchiral Light”. In: *Science* 332.6027 (2011), pp. 333–336. DOI: [10.1126/science.1202817](https://doi.org/10.1126/science.1202817). eprint: <https://www.science.org/doi/pdf/10.1126/science.1202817>. URL: <https://www.science.org/doi/abs/10.1126/science.1202817>.
- [92] Yijie Shen et al. “Optical vortices 30 years on: OAM manipulation from topological charge to multiple singularities”. In: *Light: Science & Applications* 8.1 (Nov. 2019), p. 90. ISSN: 2047-7538. DOI: [10.1038/s41377-019-0194-2](https://doi.org/10.1038/s41377-019-0194-2). URL: <https://doi.org/10.1038/s41377-019-0194-2>.
- [93] M V Berry and Wei Liu. “No general relation between phase vortices and orbital angular momentum”. In: *Journal of Physics A: Mathematical and Theoretical* 55.37 (Aug. 2022), p. 374001. DOI: [10.1088/1751-8121/ac80de](https://doi.org/10.1088/1751-8121/ac80de). URL: <https://dx.doi.org/10.1088/1751-8121/ac80de>.
- [94] R Grella. “Fresnel propagation and diffraction and paraxial wave equation”. In: *Journal of Optics* 13.6 (Nov. 1982), p. 367. DOI: [10.1088/0150-536X/13/6/006](https://doi.org/10.1088/0150-536X/13/6/006). URL: <https://dx.doi.org/10.1088/0150-536X/13/6/006>.
- [95] Harry Bateman and Bateman Manuscript Project. *Tables of Integral Transforms*. McGraw-Hill Book Company, 1954.
- [96] Aleksandr Y. Bekshaev, Konstantin Y. Bliokh, and Franco Nori. “Transverse Spin and Momentum in Two-Wave Interference”. In: *Phys. Rev. X* 5 (1 Mar. 2015), p. 011039. DOI: [10.1103/PhysRevX.5.011039](https://doi.org/10.1103/PhysRevX.5.011039). URL: <https://link.aps.org/doi/10.1103/PhysRevX.5.011039>.

- [97] Carmelo Rosales-Guzmán, Bienvenu Ndagano, and Andrew Forbes. “A review of complex vector light fields and their applications”. In: *Journal of Optics* 20.12 (Nov. 2018), p. 123001. DOI: [10.1088/2040-8986/aaeb7d](https://doi.org/10.1088/2040-8986/aaeb7d). URL: <https://dx.doi.org/10.1088/2040-8986/aaeb7d>.
- [98] V. V. Kotlyar, S. S. Stafeev, and A. G. Nalimov. “Energy backflow in the focus of a light beam with phase or polarization singularity”. In: *Phys. Rev. A* 99 (3 Mar. 2019), p. 033840. DOI: [10.1103/PhysRevA.99.033840](https://doi.org/10.1103/PhysRevA.99.033840). URL: <https://link.aps.org/doi/10.1103/PhysRevA.99.033840>.
- [99] V. V. Kotlyar, A. G. Nalimov, and S. S. Stafeev. “Exploiting the circular polarization of light to obtain a spiral energy flow at the subwavelength focus”. In: *J. Opt. Soc. Am. B* 36.10 (Oct. 2019), pp. 2850–2855. DOI: [10.1364/JOSAB.36.002850](https://doi.org/10.1364/JOSAB.36.002850). URL: <https://opg.optica.org/josab/abstract.cfm?URI=josab-36-10-2850>.
- [100] E S Kozlova and V V Kotlyar. “The backflow of energy in a optical vortex formed by silver spiral zone plate”. In: *2019 Photonics & Electromagnetics Research Symposium - Spring (PIERS-Spring)*. Rome, Italy: IEEE, June 2019. DOI: <https://doi.org/10.1109/PIERS-Spring46901.2019.9017292>. URL: <https://ieeexplore.ieee.org/document/9017292>.
- [101] Yudong Lyu et al. “Hybrid polarization induced transverse energy flow”. In: *Optics Communications* 485 (2021), p. 126704. ISSN: 0030-4018. DOI: <https://doi.org/10.1016/j.optcom.2020.126704>. URL: <https://www.sciencedirect.com/science/article/pii/S0030401820311238>.
- [102] Andrey V. Novitsky and Denis V. Novitsky. “Negative propagation of vector Bessel beams”. In: *J. Opt. Soc. Am. A* 24.9 (Sept. 2007), pp. 2844–2849. DOI: [10.1364/JOSAA.24.002844](https://doi.org/10.1364/JOSAA.24.002844). URL: <https://opg.optica.org/josaa/abstract.cfm?URI=josaa-24-9-2844>.
- [103] S J van Enk. “Selection rules and centre-of-mass motion of ultracold atoms”. In: *Quantum Optics: Journal of the European Optical Society Part B* 6.5 (Oct. 1994), p. 445. DOI: [10.1088/0954-8998/6/5/007](https://doi.org/10.1088/0954-8998/6/5/007). URL: <https://dx.doi.org/10.1088/0954-8998/6/5/007>.
- [104] Vasily Klimov et al. “Detecting photons in the dark region of Laguerre-Gauss beams”. In: *Opt. Express* 17.12 (June 2009), pp. 9718–9723. DOI: [10.1364/OE.17.009718](https://doi.org/10.1364/OE.17.009718). URL: <https://opg.optica.org/oe/abstract.cfm?URI=oe-17-12-9718>.
- [105] Yatao Ren et al. “Plasmonic Optical Tweezers for Particle Manipulation: Principles, Methods, and Applications”. In: *ACS Nano* 15.4 (Apr. 2021), pp. 6105–6128. URL: <https://doi.org/10.1021/acsnano.1c00466>.
- [106] Paul Dirac. *The Principles of Quantum Mechanics*. Oxford: The Clarendon Press, 1958.
- [107] Jonathan P Dowling. “Quantum optical metrology – the lowdown on high-N00N states”. en. In: *Contemp. Phys.* 49.2 (Mar. 2008), pp. 125–143. DOI: <https://doi.org/10.1080/00107510802091298>. URL: <https://www.tandfonline.com/doi/full/10.1080/00107510802091298>.
- [108] Alessandro Foi et al. “Practical Poissonian-Gaussian Noise Modeling and Fitting for Single-Image Raw-Data”. In: *IEEE Transactions on Image Processing* 17.10 (2008), pp. 1737–1754. DOI: [10.1109/TIP.2008.2001399](https://doi.org/10.1109/TIP.2008.2001399). URL: <https://ieeexplore.ieee.org/document/4623175>.

- [109] Michał Jachura and Radosław Chrapkiewicz. “Shot-by-shot imaging of Hong–Ou–Mandel interference with an intensified sCMOS camera”. In: *Opt. Lett.* 40.7 (Apr. 2015), pp. 1540–1543. DOI: [10.1364/OL.40.001540](https://doi.org/10.1364/OL.40.001540). URL: <https://opg.optica.org/ol/abstract.cfm?URI=ol-40-7-1540>.
- [110] Radosław Chrapkiewicz. “Generation and characterization of spatially structured few-photon states of light”. DoctoralThesis. Feb. 2016. URL: <https://repozytorium.uw.edu.pl/handle/item/1415>.
- [111] Alessandro Fedrizzi et al. “A wavelength-tunable fiber-coupled source of narrowband entangled photons”. In: *Opt. Express* 15.23 (Nov. 2007), pp. 15377–15386. DOI: [10.1364/OE.15.015377](https://doi.org/10.1364/OE.15.015377). URL: <https://opg.optica.org/oe/abstract.cfm?URI=oe-15-23-15377>.
- [112] Andrei Nomerotski. “Imaging and time stamping of photons with nanosecond resolution in Timepix based optical cameras”. In: *Nuclear Instruments and Methods in Physics Research Section A: Accelerators, Spectrometers, Detectors and Associated Equipment* 937 (2019), pp. 26–30. ISSN: 0168-9002. DOI: <https://doi.org/10.1016/j.nima.2019.05.034>. URL: <https://www.sciencedirect.com/science/article/pii/S0168900219306667>.
- [113] Andrei Nomerotski et al. “Counting of Hong-Ou-Mandel Bunched Optical Photons Using a Fast Pixel Camera”. In: *Sensors* 20.12 (2020). ISSN: 1424-8220. DOI: [10.3390/s20123475](https://doi.org/10.3390/s20123475). URL: <https://www.mdpi.com/1424-8220/20/12/3475>.
- [114] A. Nomerotski et al. “Intensified Tpx3Cam, a fast data-driven optical camera with nanosecond timing resolution for single photon detection in quantum applications”. In: *Journal of Instrumentation* 18.01 (Jan. 2023), p. C01023. DOI: [10.1088/1748-0221/18/01/C01023](https://doi.org/10.1088/1748-0221/18/01/C01023). URL: <https://dx.doi.org/10.1088/1748-0221/18/01/C01023>.
- [115] Victor Vidyapin et al. “Characterisation of a single photon event camera for quantum imaging”. en. In: *Sci. Rep.* 13.1 (Jan. 2023), p. 1009. DOI: <https://doi.org/10.1038/s41598-023-27842-7>. URL: <https://www.nature.com/articles/s41598-023-27842-7>.
- [116] Miles Padgett. “Orbital angular momentum of single photons: revealing quantum fundamentals”. en. In: *Philos. Trans. A Math. Phys. Eng. Sci.* 382.2287 (Dec. 2024), p. 20230327. DOI: <https://doi.org/10.1098/rsta.2023.0327>. URL: <https://royalsocietypublishing.org/doi/10.1098/rsta.2023.0327>.
- [117] Zhen-Fei Zhang et al. “Observation of single-photon azimuthal backflow with weak measurement”. In: *Opt. Lett.* 50.2 (Jan. 2025), pp. 333–336. DOI: [10.1364/OL.540905](https://doi.org/10.1364/OL.540905). URL: <https://opg.optica.org/ol/abstract.cfm?URI=ol-50-2-333>.
- [118] Peter W. Hawkes and Erwin Kasper. *Principles of Electron Optics, Volume 3: Wave Optics*. https://books.google.pl/books/about/Principles_of_Electron_Optics_Volume_3.html?id=CkAyEAAAQBAJ&redir_esc=y. (Accessed on 06/19/2024).
- [119] Ludwig Reimer and Helmut Kohl. *Transmission Electron Microscopy: Physics of Image Formation*. https://books.google.pl/books/about/Transmission_Electron_Microscopy.html?id=o-0nI8hxEpMC&redir_esc=y. (Accessed on 06/19/2024).
- [120] David B Williams and C Barry Carter. *Transmission electron microscopy*. en. 2nd ed. New York, NY: Springer, Jan. 2009.

- [121] P.W. Hawkes and E. Kasper. *Principles of Electron Optics: Basic geometrical optics*. Principles of Electron Optics. Academic Press, 1989. ISBN: 9780123333513. URL: <https://books.google.co.in/books?id=MrvvAAAAMAAJ>.
- [122] P.W. Hawkes and E. Kasper. *Principles of Electron Optics, Volume 2: Applied Geometrical Optics*. Academic Press, 2017. ISBN: 9780128134054. URL: <https://books.google.co.in/books?id=LzAUDgAAQBAJ>.
- [123] Amir H Tavabi et al. "The Young-Feynman controlled double-slit electron interference experiment". en. In: *Sci. Rep.* 9.1 (July 2019), p. 10458. DOI: <https://doi.org/10.1038/s41598-019-43323-2>. URL: <https://www.nature.com/articles/s41598-019-43323-2#citeas>.
- [124] Aristide Dogariu, Sergey Sukhov, and José Sáenz. "Optically induced 'negative forces'". en. In: *Nat. Photonics* 7.1 (Jan. 2013), pp. 24–27. DOI: <https://doi.org/10.1038/nphoton.2012.315>. URL: <https://www.nature.com/articles/nphoton.2012.315>.
- [125] Xiaohang Sun, Matthew Reichert, and Jason W. Fleischer. "Measurement of Biphoton Wigner Function Using a Lenslet Array". In: *Imaging and Applied Optics 2016*. Optica Publishing Group, 2016, CW1C.2. DOI: [10.1364/COSI.2016.CW1C.2](https://doi.org/10.1364/COSI.2016.CW1C.2). URL: <https://opg.optica.org/abstract.cfm?URI=COSI-2016-CW1C.2>.
- [126] Yang Lv et al. "SU-G-IeP4-09: Method of human eye aberration measurement using plenoptic camera over large field of view". In: *Med. Phys.* 43.6Part28 (June 2016), pp. 3679–3679. DOI: <https://doi.org/10.1118/1.4957104>. URL: <https://aapm.onlinelibrary.wiley.com/doi/abs/10.1118/1.4957104>.
- [127] Francesco Di Lena et al. "Correlation Plenoptic Imaging: An overview". en. In: *Appl. Sci. (Basel)* 8.10 (Oct. 2018), p. 1958. DOI: <https://doi.org/10.3390/app8101958>. URL: <https://www.mdpi.com/2076-3417/8/10/1958>.
- [128] Markus Hiekkamäki et al. "Observation of the quantum Gouy phase". en. In: *Nat. Photonics* 16.12 (Dec. 2022), pp. 828–833. DOI: <https://doi.org/10.1038/s41566-022-01077-w>. URL: <https://www.nature.com/articles/s41566-022-01077-w>.
- [129] David Trillo, Thinh P Le, and Miguel Navascués. "Quantum advantages for transportation tasks - projectiles, rockets and quantum backflow". en. In: *Npj Quantum Inf.* 9.1 (July 2023). DOI: <https://doi.org/10.1038/s41534-023-00739-z>. URL: <https://www.nature.com/articles/s41534-023-00739-z>.